University of Strathclyde
Department of Mechanical Engineering

Extending the applicability of the Navier–Stokes equations to micro gas flows by considering molecular collisions with boundaries

Erik Johan Arlemark

A thesis presented in fulfilment of the requirements
for the degree of Doctor of Philosophy

2010

“This thesis is the result of the author’s original research. It has been composed by the author and has not been previously submitted for examination which has led to the award of a degree.”

“The copyright of this thesis belongs to the author under the terms of the United Kingdom Copyright Acts as qualified by University of Strathclyde Regulation 3.50. Due acknowledgement must always be made of the use of any material contained in, or derived from, this thesis.”

Signed: Date: 8th of April 2010

Abstract

This thesis investigates the mean travelling distance of molecules between successive collisions, which is referred to as the mean free path, and how this parameter can extend the applicability of the isothermal Navier–Stokes–Fourier equations (the Navier–Stokes equations) for micro scale gas flows. Since gas molecules in micro-scale geometries are likely to experience a significant number of wall collisions as opposed to the normally considered inter-gas molecular collisions, the geometrical dependence of the mean free path is of special concern for this thesis. A theoretical description for the geometry-dependent mean free path is derived, referred to as the effective mean free path, in the vicinity of planar and non-planar surfaces. This theoretical effective mean free path is measured and validated using the deterministic particle-based method of molecular dynamics. Comparisons of the theoretical and measured effective mean free path profiles show good agreement for the case of specular wall reflections; as opposed to diffusive reflections or reflections caused by explicit walls. The largest discrepancy between theoretical and measured mean free paths is shown to be for non-planar geometries. The effective mean free path descriptions are applied to the Navier–Stokes equations by relating the mean free path to viscosity and thereby obtaining a non-linear stress-to-strain-rate relationship. The effective mean free path is also used in the applied velocity boundary conditions of first- and second-order. The present models are solved for the planar-wall test-cases of Couette flow and Poiseuille flow. Their solutions for both of these cases are found to converge with the conventional Navier–Stokes solutions for small Knudsen numbers. For Couette flow it is found that the present model produces non-linear velocity profiles that compare well with direct simulation Monte Carlo data up to a Knudsen number of about one. For Poiseuille flow it is found that the present model does not capture the same velocity profile as the validation data from the BGK method for Knudsen numbers above 0.5. However, the present model using a second-order velocity boundary condition has roughly the same cross-sectional average velocity, which causes the mass flow rates to be similar. The mass flow rates are compared with experimental measurements and results of the BGK method. It is shown that the present model using a second-order velocity boundary condition captures the mass flow minimum at a Knudsen number of about one, and approaches a bounded value for larger Knudsen numbers consistent with the experimental validation data.

Acknowledgements

The author would particularly like to thank the supervisor of this work, Prof. Jason Reese, and also Dr Kokou Dadzie for their guidance and support of numerous aspects in the field of rarefied gas-flows. The author would like to thank Dr Chris Greenshields for his support concerning general usage of the software OpenFOAM [1]. Support is also given in the form of insight and implementation guidance of the molecular-dynamics solver, applications and utilities of OpenFOAM by Dr Graham Macpherson and Matthew Borg. The author would also like to thank Dr Simon Mizzi for helpful discussions and insight into the BGK method and Dr Timothée Ewart for providing experimental data.

This research is funded in the UK by the Engineering and Physical Sciences Research Council under grant number EP/D007488/1.

Contents

List of Figures

List of Tables

Nomenclature

Parameters in lightface indicate scalars, boldface indicate vectors and second-order tensors. In the unit indication below the following notation is used kilogram (kg), meter (m), second (s), temperature (K), joule (J), radians (rad) and dimensionless quantity (—)

Parameter	description with unit indication
A_{CS}	channel cross-sectional area, [m^2]
C	molecular velocity, [m/s]
c_p	specific heat capacity at constant pressure, [J/(kg K)]
c_v	specific heat capacity at constant volume, [J/(kg K)]
D, D'	velocity-slip coefficients, [—]
D_{tr}	molecular travelling distance, [m]
d	molecular diameter, [m]
H	channel height, [m]
$\boldsymbol{I}$	identity tensor, [—]
J	scaling function used with the effecitve mean free path, [—]
Kn	Knudsen number, [—]
k	thermal conductivity, [J/(m s K)]
L	length of a channel, [m]
l	edge length of molecular dynamics domain, [m]
m	molecular mass, [kg]
$\dot{m}$	mass flow rate, [kg/s]
N_{Av}	Avogadro's constant, [1/mol]
N_s	number of simulated molecules in domain, [—]
N_t	number of theoretical molecules in domain, [—]
$\mathbf{n}$	wall normal vector, [—]
n	magnitude of wall normal vector, [m]
n	molecular number density, [m^{-3}]
P	molecular collision probability function, [—]
Pr	Prandtl number, [—]
p	gas pressure, [kg/(m s^2)]
p_d	molecular collision probability density, [—]
$\boldsymbol{q}$	heat flux vector, [J/(m^2 s)]

R	specific gas constant, [J/(kg K)]
R_{u}	universal gas constant, [J/(mol K)]
r	molecular separation distance, [m]
r_d	radial distance, [m]
s	generalised power mean coefficient, [—]
T	gas temperature, [K]
T_{jump}	temperature-jump, [K]
t	time, [s]
$\mathbf{t}$	wall tangential vector, [—]
$\boldsymbol{v}$	mass average velocity, [m/s]
$\boldsymbol{v}_{\mathrm{slip}}$	velocity slip, [m/s]
$\widetilde{v}_t$	normalised average velocity across the channel width, [—]
$\mathbf{x}$, $\mathbf{y}$, $\mathbf{z}$	Cartasian coordinates, [m]
Z	rate of molecules crossing a plane per unit area, [1/(m^2 s)]

α	thermal diffusivity, [m^2/s]
β	constant of proportionality (used with Z), [—]
Γ	sound damping coefficient, [m^2/s]
γ	specific heat ratio, [—]
δ	inverse rarefaction parameter, [—]
δ_{sp}	average molecular spacing, [—]
η	inverse power law coefficient, [—]
θ	zenith angle of molecular travelling direction, [rad]
κ	bulk viscosity, [kg/(m s)]
κ_{IPL}	inverse power law coefficient, [—]
λ	unconfined and conventional molecular mean free path, [m]
μ	dynamic viscosity, [kg/(m s)]
υ	variable-hard-sphere constant, [—]
ρ	gas density, [kg/m^3]
$\mathbf{\Pi}$	viscous sheer stress tensor, [kg/(m s^2)]
$\sigma_{\boldsymbol{T}}$	thermal accommodation coefficient, [—]
$\sigma_{\boldsymbol{v}}$	tangential momentum accommodation coefficient, [—]
τ_{col}	molecular collsion frequency, [1/s]
$\boldsymbol{\tau}$	viscous stress vector, [—]
Ω_{μ}	collision integral for viscosity, [—]
ω	variable-hard-sphere constant, [—]

Superscripts

X^t	transpose operator

Subscripts

X_{eff}	an "effective quantity" that is geometry-dependent
X_{w}	a quantity determined at the wall or surface
X_{wall}	a quantity belonging to a wall or surface
X_i	a quantity belonging to a molecule with i-index
X_j	a quantity belonging to a molecule with j-index
X_{n}	the normal-component of a vector quantity
X_{t}	the tangential-component of a vector quantity
X_{x}	the x-component of a vector quantity
X_{y}	the y-component of a vector quantity

Molecular models

HS	hard-sphere molecular model
IPL	inverse-power-law molecular model
LJ	Lennard-Jones molecular model
MM	Maxwellian molecular model
SS	soft-sphere molecular model
VHS	variable-hard-sphere molecular model

Not everything that counts can be counted,
and not everything that can be counted counts.

Albert Einstein

Chapter 1

Modelling micro gas flows

The study of this thesis is aimed at the smaller end of a length scale conceivable to man. To bring some perspective to this length scale, some of the larger known objects will be mentioned before a few of the relevant ones. At the larger end astronomical lengths are good examples such as the width of our galaxy, the Milky Way, which is about 9×10^{20}m, the diameter of the sun being about 1.4×10^{9}m, the diameter of earth at approximately 1.3×10^{7}m. At the smaller side of this length scale are the diameter of a light hydrogen nucleus (only consisting of a proton) being about 1.6×10^{-15}m, the fixed sphere representation of a hydrogen molecule of about 2.2×10^{-10}m and the approximate length of the average travelling distance for helium molecules between successive collisions of 1.7×10^{-7}m. The length unit micrometer (μm) is 10^{-6}m and is a central length unit in this work due to the fact that most phenomena studied in this thesis are in the micro length scale ranging from 1μm to 1mm. The word micro is also used in the definition of *microscopic-parameters*, which refers to atomistic-quantities (such as the molecular velocities). The microscopic-parameters can be averaged over certain volumes or masses in order to assess *macroscopic-parameters* (such as mass-averaged velocity or temperature) which are commonly used in the solution methods of the fluid dynamics based on the continuum description.

While manufacturing techniques such as DRIE (deep reacting ion etching) are continually improved in our modern society ever smaller devices have been brought into production. The significant advance in pushing the limits of the production skills of miniaturisation has partly been due to curiosity but it may have found its drive from new doors being opened to potential markets within important fields such as industrial and medical applications. Today there are numerous kinds of micro-scaled devices operating and being in the early stages of development, which help us to measure and actuate at this characteristic length scale. Some of the small devices that have been produced so far are motors, valves, gears, cantilevers, diaphragms and tweezers of a dimension of less than 100 μm which can function by electrostatic, magnetic, electromagnetic, pneumatic and thermal actuators. Many of these devices can be used in sensors of micro-flow measurements for pressure, temperature, mass-flow, velocity, sound, chemical composition and as actuators for linear and angular motion [17] for example. Many of these devices are commonly referred to as micro-electro-mechanical-systems (MEMS), which solve quite simple tasks as well as series of operations at the micro-scale. An interesting and common micro environment where an alternative gas modelling technique is of particular concern is for hard disk drives where the reading head is situated about 65 nanometer (nm) above the disk, for which the load capacity would be erroneously predicted by using conventional macroscopic methods [29]. Other engineering based modelling areas are micro-motors where the gap between rotor and the stator is about 3μm [29], micro-channel cooling of IC chips [38] and micro-reactors for chemical synthesis [38].

With a better understanding of the surface effects experienced by gas flows in a micro scale environment, here referred to as micro gas flows, we are not only likely to improve our micro-scale manufacturing techniques but we might also be able to understand mysteries in nature such as the way mosquitoes manage to hear sounds using brush-like micro-scale antennae [26]. In the medical field, a better understanding of micro gas flows can bring forward techniques to provide more efficient delivery of inhaled medications and to understand the effects of inhaled pollutants better [19]. There are similar effects present for both micro gas flows and aerospace-flows. For the latter flows these effects occur because of the dilute gas situation even though the length-scale of aerospace-flows often are of normal dimensions. Therefore, perhaps a better understanding of the nature of micro gas flows will help to improve modelling capabilities in micro gas flows as well as gas flows related to aerospace research. It is, for instance, argued in the article by Flieseler [16] that orbital travel in the lower atmosphere could be made possible using solar sails, for which a correct understanding of the molecular surface interactions would be of major concern. Other similarities between micro-scale flows and macro-scale flows could be the description of granular flows, which avalanches could be characterised as according to Reese *et al.* [51].

Mohamed Gad-el-Hak [17] has listed the supporting funding for this field in the years 1997, 2002 and 2004 amounting to \$432 million, \$2.2 billion and \$3.5 billion respectively, showing a marked increase. This vast and increasing investment reflects the interest and desire for better understanding of these flows which will hopefully lead to cheaper production of more efficient micro-devices becoming more common in our everyday life in the future.

The constitutive and conventional thermal modelling technique for flows at the macroscopic length-scale consists of the Navier–Stokes–Fourier equations, whereas the Navier–Stokes equations constitute the conventional isothermal fluid modelling technique. With improved manufacturing capabilities of micro structures it can be shown that our conventional fluid modelling techniques for macro-scale flows applied with conventional boundary conditions fail to predict the behaviour of micro gas flows. This is because micro gas flows differ from macro gas flows due to certain rarefaction, compressibility and surface effects [38]. At small gas-flow-scales the continuum description may break down. Slip flow, thermal creep, rarefaction, viscous dissipation, compressibility, intermolecular forces, and other unconventional effects may have to be taken into account, preferably using only the first principles such as conservation of mass, Newtons second law, and conservation of energy [18]. The degree of rarefaction is essentially quantified by the Knudsen number, Kn (Kandlikar *et al.* [28]). The compressibility effects are caused by viscous forces induced by the high strain rates [17]. It is shown by experimental investigators such as Turner *et al.* [63], Jang *et al.* [27] and Yohung and Chan [70] that isothermal micro gas flows have significant compressible characteristics. This contradicts the criteria for isothermal normal scale flows which at the most has density variations of 5% below a Mach number of 0.3, but above this value the density variations become significant. It is shown by Yuhong and Chan that for a pressure-driven flow in-between a two planar-wall geometry the modelled rarefaction effects counteract the modelled compressibility effects causing the non-linear axial pressure profile tend to a more linear shape [70]. For micro gas flows the surface-effects also become important and must be taken into account as a result of the scale difference between the relatively large ratio of the confining boundary surface area to the volume of the confined gas. The surface-effects considerably influence a flow in the near-wall region, referred to as the *Knudsen layer*, which, because of the small scale of the system, represent a substantial portion of the gas volume. These effects are transmitted by the gas molecules' interactions with surfaces. The structure of the Knudsen layer in the gas and the conditions on fundamental modelling techniques have been investigated by Trilling [62].

A better understanding of micro gas flows can be obtained by inspecting the molecules and the behaviour of these molecules which averaged properties fully describes the flow. From a qualitative modelling viewpoint the interactions of the molecules should ideally be simulated using smooth potential-functions. These are dependant on the molecular separation distances being repulsive at short range and attractive at long range. The molecular collision frequency and the closely connected average travelling distance of molecules between intermolecular collisions — the mean free path, λ — are often discussed as important descriptive properties of a gas. However, they are somewhat fictional and simplified representations of the actual molecular behaviour since molecules do not experience collisions at one instant and therefore they do not have a corresponding travelling distance between these collisions. Instead they are affected by each other's presence everywhere in the gas. It is therefore necessary to determine the criteria for when a gas molecular collision has occurred. In a modelling aspect such criteria could be the switch between positive and negative potential between the molecules as they approach each other or directly the separation distance itself. The width of the Knudsen layer, within which the surface-effects considerably affect the flow, is usually appreciated using the quantity mean free path and is considered by many investigators to be one to two mean free paths wide.

To indicate the degree of rarefaction, or the state of non-equilibrium of gas flows, the key parameter, the Knudsen number,

$$Kn = \frac{\lambda}{L}, \tag{1.1}$$

is used. In Eqn (1.1) L is the typical length-scale of the flow. This length-scale is usually adequately determined by:

$$L = \frac{\Theta}{\left|\frac{\partial \Theta}{\partial \mathbf{y}}\right|}, \tag{1.2}$$

where Θ is a macroscopic flow parameter (usually density, ρ) and ($\mathbf{y}$) is a spatial coordinate. For micro channel flows confined by planar parallel walls the separation distance of the walls is often chosen as the typical length-scale for simplicity instead of L.

Some effects similar to those occurring for micro gas flows are apparent in macro-scale cases as well, if the gas is dilute enough. This can be seen from Eqn (1.1): a dilute gas has a low density and therefore a large mean free path yielding in turn a large Kn. The relatively large Kn value for micro gas flows is however due to small dimensional length-scales, which causes the rarefaction effects to become apparent. For micro gas flows, the state of non-equilibrium is mainly located in the Knudsen layer. Here non-equilibrium is introduced to the flow by gas molecules interacting with the solid wall which re-emits molecules with a Maxwellian velocity distribution [32]. The criterion for a gas to be in equilibrium is to have a Maxwellian velocity distribution. However, when the gas has a bulk movement different from the wall there will be a difference in the velocity distributions of the re-emitted molecules and the incoming molecules causing the non-equilibrium. For macro gas flows the width of the Knudsen layer is relatively thin compared to the bulk of the flow which means that the Knudsen layer has a negligible effect on the flow in general. However, for micro gas flows the width of the Knudsen layer is comparable to the length-scale of the flow which means that surface-induced rarefaction effects impacts on a considerable large part of the domain of the flow [34] and must therefore be taken into account for a proper flow description.

Experiments, such as those performed by Arkilic *et al.* [3] and Colin [10], have shown that the conventional Navier–Stokes fluid flow model (presented in section 2.4.2) cannot capture the correct mass flow rates of a pressure-driven flow in micro-channels unless certain velocity-slip boundary conditions are imposed at the walls. The conventional no-slip boundary condition commonly used in conjunction with the Navier–Stokes equations is valid only for cases where the gas is in a state of near-equilibrium or can properly be represented by a continuum description. This gas state is considered to occur for

$Kn \leq 0.001$ and is referred to as *continuum flow*, as illustrated in Figure 1.1. Micro gas flows of larger Kn require boundary conditions that allow a certain amount of velocity-slip [17]. The lower threshold value for applying the slip boundary condition is generally $Kn = 0.001$, which therefore is referred to as the lower limit of the *slip-flow regime*. For gas flows at larger Kn, further modelling modifications are needed because the linear constitutive relationships of Navier–Stokes equations becomes invalid. This threshold is at about $Kn = 0.1$, which is known as the lower limit of the *transition regime*. The name "transition regime" is appropriate in the sense that the gas-flow is not well described by either a continuum description or by the *free-molecular flow* description occurring at about $Kn \geq 10$. The transition regime, which this work mostly focuses on is generally recognised as a problematic area to describe and predict.

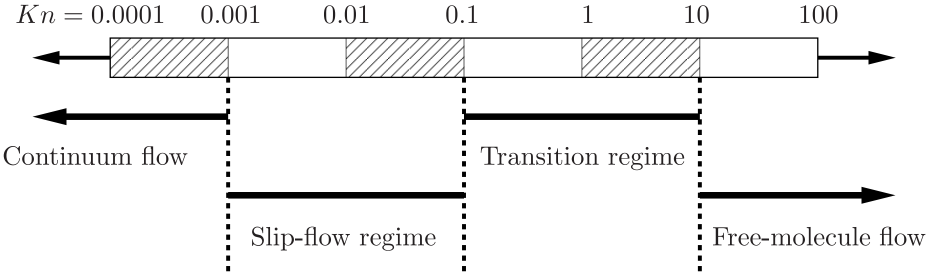

Figure 1.1: Knudsen number regime classification from Schaff [52], Gad-el-Hak [17].

.

The modelling techniques available for rarefied flows are illustrated in Figure 1.2, and their interconnections. Fluid flows can either be modelled as they really are, i.e. a collection of molecules, or as a continuum, being indefinitely divisible. Molecular models can either be deterministic, consisting of the technique of molecular dynamics (MD), or statistical, originating from the Liouville equation. The Liouville equation can be used for deriving the Boltzmann equation, being a fundamental description of kinetic theory for gases. The Liouville equation is also a fundamental building block for the conventional continuum methods and for the popular modelling method of direct simulation Monte Carlo (DSMC).

1.1 Boltzmann equation

The Boltzmann equation is derived from the Liouville equation, which is a fundamental statistical mechanics equation for gases. The Liouville equation is based on the phase-space function which consists of the combination of three coordinates describing location in physical-space and three coordinates describing velocity-space, resulting in a six-dimensional space. From the phase-space function the probability of finding a molecule with a particular position and velocity at any given time can be defined based

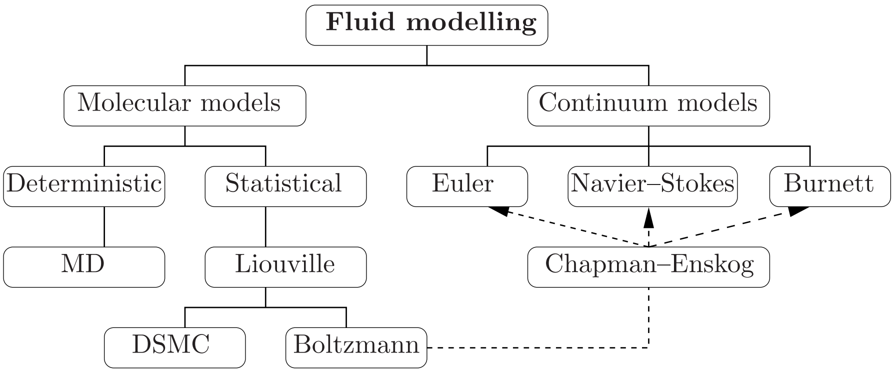

Figure 1.2: Molecular and continuum gas flow models [17].

on the conservation of the $6N$ phase-space distribution function over the N molecules in the system. The Liouville equation does not consider the changes of the phase-space distribution due to molecular collisions as opposed to the Boltzmann equation [6].

Although it would be ideal to achieve the exact dynamics of N particles, this is not possible since in practical calculations this requires a number of variables in the order of 6^N [8, 62]. This is why Boltzmann and Maxwell derived the Boltzmann equation which is only dependent on the one particle distribution function, obtained by integrating the Liouville equation and using the assumption of the studied gas being dilute and considered to be in a state of molecular chaos [6]. With molecular chaos it is assumed that the phase-space of two colliding molecules is the same as the product of the corresponding phase-spaces for both molecules. In contrast to the Liouville equation the Boltzmann equation is dependent on a non-linear collision integral that describes the net effect of populating and depopulating collisions on the distribution function [17].

The five conservation equations of mass, momentum and energy can be obtained from the Boltzmann equation by multiplying the distribution function with molecular mass, momentum and kinetic energy respectively and then integrating over all velocity space. Although the Boltzmann equation remains valid for all Kn and it produces much richer detail of the gas state than the Navier–Stokes–Fourier equations it is relatively expensive in terms of computational capacity [20]. Sharipov [55] stated that the Boltzmann equation is particularly recommended for modelling low Mach flows and flows with simple geometrical configurations. The solutions of the Boltzmann equation to arbitrary geometries are difficult to find, mostly due to the non-linearity of the collision integral. Simplified models of the collision integral have therefore been proposed in order to facilitate analytical solutions. An example of such a model is the Bhatnagar, Gross and Krook (BGK) model, which is used as a validation reference for the Couette flow velocity profiles in chapter 5.

1.2 Continuum methods

The continuum models consisting of the Euler, Navier–Stokes–Fourier and Burnett equations are non-linear partial differential equations describing the conservation of the macroscopic flow parameters mass, momentum and energy in every small sub-volume of a flow. These equations can be obtained through a Chapman–Enskog expansion of the Boltzmann equation using Kn as a smallness parameter. This expansion yields a first-, second- and third-order of accuracy with respect to Kn for the Euler, Navier–Stokes–Fourier and Burnett equations respectively. Alternatively the Euler and Navier–Stokes–Fourier equations can be derived directly, although for the Navier–Stokes–Fourier equations some empiricism is necessary to close the resulting indeterminate set of equations [17]. The Euler equation is a form of the Navier–Stokes–Fourier momentum equation, as shown in section 2.4.2, which is obtained in case the viscous forces terms are excluded. The Euler equations do not have viscous stress terms and comprises therefore a simple and appropriate solution method for equilibrium flows at $Kn \approx 0$, as noted by Xue *et al.* [69]. When solving non-equilibrium flows viscous stresses are common which makes the Euler equations inappropriate for these flows. The Navier–Stokes–Fourier equations become invalid at about $Kn = 0.1$ due to rarefaction effects, which for example is verified by a calculation of a Couette flow by Zheng *et al.* [71]. It is also stated by Zheng *et al.* that none of the continuum methods produce good results for the Couette flow case at $Kn > 0.1$. The Burnett equations have non-linear stress to strain rate and temperature to heat flux relationships, which makes these equations potentially more appropriate to model micro gas flows. As noted by Dongari [13], the Navier–Stokes equations generally perform better than the Burnett equations for $Kn < 0.01$. It is reported by Lockerby and Reese [31] that the Burnett equations are only stable up to $Kn = 1$. Since this thesis is mainly dedicated to extending the validity of the isothermal Navier–Stokes–Fourier, equations section 2.4.2 offers a more thorough presentation of this method.

The continuum methods are dependent on certain boundary conditions for the macroscopic parameters. One of the main interest of micro gas flows is what type of boundary conditions shall be applied in order to account for molecular gas/surface interactions correctly. There are generally first- and second-order sets of velocity and temperature boundary conditions, with regard to their accuracy in Kn [17]. Since it is still of great interest to find appropriate boundary conditions for micro gas flows there have also been attempts of slightly more heuristic types, such as the 1.5 order slip boundary condition by Mitsuya [43], and a hyperbolic-tangential function-based boundary condition by Xue and Fan [68]. A physical and chemical approach to describe the velocity-slip is presented by Myong *et al.* [45] where the molecules of the gas can be adsorbed for some time, by a wall having a long-range force which releases the molecules after some time lag. A temperature boundary condition has also been derived based on Langmuir's theory. This temperature boundary condition has been investigated by Myong *et al.* [44] where results showed a decreased heat transfer for increased Kn.

Modelling of surface-effects in the near-wall area of micro gas flows should ideally be performed using kinetic theory. However, an approximate extension to the Navier–Stokes–Fourier equations would be less demanding in terms of computational capacity, and the simplicity and practicality of the Navier–Stokes–Fourier equations make it desirable to solve flow cases using this model for as high Kn flows as possible. It was suggested by Stops [60] and Guo *et al.* [22] that the validity of the Navier–Stokes equations may be extended to larger Kn by a modification to the conventional expression for the molecular mean free path. This modification would incorporate gas molecular interactions with solid boundaries, in addition to the inter-molecular-gas collisions in the mean free path expression. This yields a geometry-dependent mean free path, which in this thesis is referred to as the *effective mean free path*. Using similar reasoning as Stops and Guo *et al.* this thesis presents an effective mean free path in chapter 3, which is then compared to measurements of the effective mean free path using molecular dynamics, in chapter 4. The effective mean free path expression is used for solving the Navier–Stokes equations in chapter 5 for isothermal cases for the discontinuous velocity boundary conditions of first- and second-order accuracy. Here the focus is on the predictions of Couette and Poiseuille planar wall cases, where the velocity flow profiles and the Poiseuille mass flow rate are studied.

1.3 DSMC method

The DSMC method is a statistical computational molecular approach for solving rarefied gas problems. The DSMC method treats the molecular collisions probabilistically and the molecular motions deterministically. In this method a simulated DSMC particle represents many real molecules, which causes a lower computational demand than if all molecules where to be simulated. Another computational advantage with the DSMC method is that the molecular motions are uncoupled with the intermolecular collisions over small time intervals. The DSMC method is, like the Boltzmann equation, valid for all Kn but becomes computationally expensive for $Kn < 0.1$, which fortunately is the upper limit of the Navier–Stokes equations with an applied slip boundary condition. Since the non-linear collision term of the Boltzmann equation is difficult to solve for flows in the transition regime the best approach for this regime is now the DSMC method [17]. Sharipov has listed situations for which the DSMC method is particularly recommended: high Mach flows, small (compact) region of gas-flows, complicated geometrical configurations and flows with dissociation, recombinations, ionisation etc.

The Boltzmann equation, being based on kinetic theory and derived through physical and probabilistic reasoning has assumptions that are very close to those of the DSMC method. Two of these common assumptions are that the studied gas is dilute and in a state of molecular chaos.

The DSMC method is used in this thesis to validate the extended Navier–Stokes equations in section 5.1.

1.4 Molecular dynamics

In molecular dynamics every single molecule's position and velocity is modelled and is initialised from the start of a simulation. The molecular movements are determined by using Newton's law relating the present intermolecular forces to the molecular masses and accelerations. Molecular dynamics is therefore a deterministic model having only one possible simulation outcome. To obtain macroscopic flow quantities such as density, velocity, pressure and temperature from molecular dynamics an averaging over the molecular parameters is required. This vast amount of averaging can be understood considering that all changes in a flow spread out in the gas domain through molecular collisions, which for a neon gas molecule in a gas at standard temperature and pressure occurs on average about every 2.6×10^{-10}s (as is shown in section 4.2). So, if a certain resolution of a desired macroscopic parameter is to be evaluated an averaging is needed that covers a sufficient number of molecules sampled over a sufficient amount of time. An example of the vast amount of sampling can be made by analysing the molecular dynamics method when used to sample the mean free path in chapter 4. Here the mean free path is recorded for three different noble gases, for various cases, using between 6300 and 170 000 molecules. The sampling of the molecular mean free paths is typically made over a time range of about 3ns. Since every molecule has its collision-free travelling distance recorded every time step of about 1×10^{-14}s this adds up to about 2 billion samples for the case of about 6300 molecules. If the sampling time is short compared to the averaged collision frequency time the result will be dominated by highly fluctuating values. If however the averaging is done over a time-scale which is too long compared to the time it takes for molecules to travel the average distance of the mean-free-path then the time-transient changes of the flow will be missed: Kandlikar *et al.* [28]. To give an idea of the appropriate sampling domain size it is reported by Karniadakis *et al.* [29] that a sampling volume of 10 000 molecules results in 1% statistical fluctuations of the macroscopic quantities, but this depends on whether there are transient changes in the gas domain. If the flow is at a steady state it is possible to sample fewer molecules but over a longer time period.

Molecular dynamics is commonly used to simulate liquids at the nano-scale. This is due to the amount of simulated molecules being few enough at this scale, taking into consideration that the typical simulation time is proportional to the square of the number of simulated molecules. Molecular dynamics is also appropriate for simulating liquids since liquids require a correct description of a continuous intermolecular interaction potential as opposed to gas flows which mostly experience collision-less travelling paths. However, in this thesis the method of molecular dynamics is used to simulate gas flows since a deterministic validation method is desired. This method is also used because it is difficult to use discontinuous potential forces, such as the fixed diameter hard-sphere model (presented in section 2.2.1), in direct numerical simulations where molecules are moved in discrete time-steps. This would yield infinite forces of repulsion when collisions occur at which point the molecular-diameters to cross over each other. The method of molecular dynamics is therefore of great value to this research and is used in chapter 4 to validate the theoretical effective mean free path expression derived earlier in chapter 3.

1.5 Hybrid methods

There are also undergoing investigations of hybrid methods which are designed to couple the fluid modelling techniques of the particle-based methods and the continuum methods. This approach is promising for modelling rarefied micro gas flows since it can both benefit from detailed description of the molecular behaviour in the near-wall areas by the particle-based method and benefit from the computationally less expensive continuum methods which are applied in the bulk regions of the flow. For micro gas flows, investigators such as Schwartzentruber [54] have developed hybrid methods where the Navier–Stokes equations and the DSMC method are coupled. A coupling has been made between the Euler equations and the DSMC method by Wijesinghe *et al.* [67]. A purely-particle based solver consisting of molecular dynamics and the DSMC method has successfully been developed by Nedea *et al.* [46].

Chapter 2

Micro gas flows: molecular and continuum flow models

Modelling of microfluidics, comprising both gas and liquid flows at the micro-scale, is a relatively young research field having its origins in the early 1980s. Micro gas flows has certain non-equilibrium effects which are similar to the effects of dilute aerospace gas flows, which mainly has its origin in the USSR in 1958 due to military purposes [28]. These resemblances has caused much of the gas-flow theory to have been passed on from the knowledge base of the aerospace gas flows to a knowledge base of micro gas flows.

In the next section some key parameters are presented, which are often used to describe and calculate micro gas flows.

2.1 Key molecular parameters

For rarefied micro gas flows the molecular diameter d, the mean molecular spacing δ_{sp} and the mean free path λ are of special concern. The molecular diameter is a somewhat fictional parameter which has several modelling representations that can be used when considering interactions between molecules. The inter molecular interactions are described most realistically using a molecular potential which is a function of the molecular separation distances denoted here by r, which is the magnitude of the relative position vector between the two molecules, $\boldsymbol{r}$. A common assumption for dilute gases is that molecules are sufficiently separated to only experience collisions involving two molecules. These collisions are referred to as *binary collisions*.

In the following sections various models of molecular representations will be presented. These molecular models consider that all occurring collisions conserve linear-momentum and energy between the before and after states of collision occurrences [6]. Collisions that conserve linear momentum and energy are *elastic-collisions*, which require

$$m_i\boldsymbol{C}_i + m_j\boldsymbol{C}_j = m_i^*\boldsymbol{C}_i^* + m_j^*\boldsymbol{C}_j^* = (m_i + m_j)\boldsymbol{C}_{\mathrm{cm}}, \tag{2.1}$$

for the momentum and

$$m_iC_i^2 + m_jC_j^2 = m_i^*C_i^{*2} + m_j^*C_j^{*2}, \tag{2.2}$$

for the energy conservation. In Eqns (2.1) and (2.2) m_i and m_j are the masses and $\boldsymbol{C}_i$ and $\boldsymbol{C}_j$ are the peculiar velocities of two colliding molecules with indexes i and j respectively. The star notation (*) indicates the post-collision state and $\boldsymbol{C}_{\mathrm{cm}}$ is the velocity of the centre of mass of the pair of molecules.

An illustration of how the micro gas flow parameters — the molecular diameter, the mean molecular spacing and the mean free path — can be inferred by Figure 2.1. The parameter δ_{sp} is the average separation distance of the molecules in the gas, which can be related to the distance between molecule 1 and 2 denoted by r_{12}. If a gas were in perfect equilibrium, all the molecules would be at equal distances from each other.

The average separation distance can be calculated from the molecular density, n, as $n = \delta_{\mathrm{sp}}^{-3}$. The parameter λ can be realised by using the illustration of Figure 2.1 where a representative collision cylinder is drawn, indicating the collision course of molecule i, having the peculiar velocity $\boldsymbol{C}_i$, with the collision candidate molecule j with peculiar velocity $\boldsymbol{C}_j$. These molecules are separated by r_{ij}, and a collision occurs if the centres of the molecules are separated by less than d. Similarly this can be formulated using the collision area $\pi(d/2)^2$, within which a collision occurs if the molecular centres are both inside. The collision area is illustrated together with its extrusion in the direction of the relative molecular velocity $\boldsymbol{C}_{\mathrm{rel}} = \boldsymbol{C}_i - \boldsymbol{C}_j$. Therefore during time, t, molecule i travels the distance $t\,|\boldsymbol{C}_i|$, during which time this molecule is anticipated to experience $\pi d^2\,|\boldsymbol{C}_{\mathrm{rel}}|\,tn$ collisions. The ratio of the travelling distance of molecule i, during time t, to the anticipated number of collisions in this time determines the mean free path as follows:

$$\lambda = \frac{t\,|\boldsymbol{C}_i|}{\pi d^2\,|\boldsymbol{C}_{\mathrm{rel}}|\,tn} = \frac{t\,|\boldsymbol{C}_i|}{\pi d^2\sqrt{\boldsymbol{C}_i\cdot\boldsymbol{C}_i - 2\boldsymbol{C}_i\cdot\boldsymbol{C}_j + \boldsymbol{C}_j\cdot\boldsymbol{C}_j tn}}. \tag{2.3}$$

If molecular collisions are considered to be uncorrelated, $\boldsymbol{C}_i \cdot \boldsymbol{C}_j = 0$ and that the magnitude of the peculiar velocities are randomly distributed yielding that on average $|\boldsymbol{C}_i|$ is equal to $|\boldsymbol{C}_j|$ the following mean free path definition for hard spheres is obtained:

$$\lambda = \frac{1}{\sqrt{2}\pi d^2 n}. \tag{2.4}$$

In the following sections the hard-sphere model (HS), the variable-hard-sphere model (VHS) and two smooth-potential models (SP) are presented. The SP models are repre-

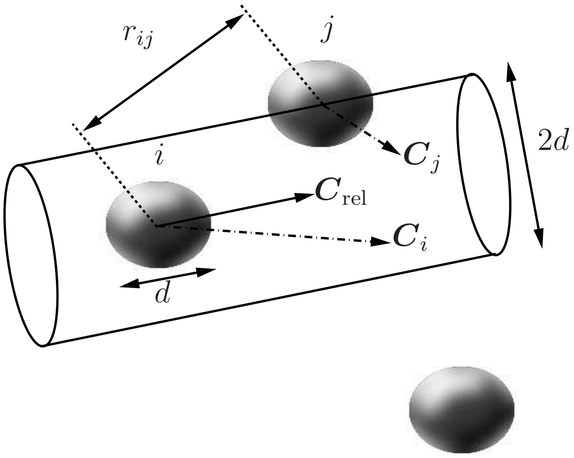

Figure 2.1: Example of a molecule i, with peculiar velocity $\boldsymbol{C}_i$, on a collision course with molecule j, with peculiar velocity $\boldsymbol{C}_j$. The separation between molecule i and j is denoted by r_{ij}. The cross-sectional collision area is $\pi(d/2)^2$, having its axial centre at the position of molecule i, which is extended in the direction $\boldsymbol{C}_{\mathrm{rel}} = \boldsymbol{C}_i - \boldsymbol{C}_j$ to illustrate collision candidates.

sented here by the inverse-power-law model and the Lennard-Jones model. The various models for describing the mean free path are dependent on the gas to be sufficiently dilute for the effects of multiple molecular collisions to be negligible. This requirement is fulfilled if:

$$\frac{d}{\delta_{\mathrm{sp}}} \ll 1, \tag{2.5}$$

as described by Kandlikar *et al.* [28]. Trilling [62] also describes the characterisation of dilute gases similar to Eqn 2.5 except for that δ_{sp} is replaced by λ.

2.2 Molecular interaction models

Here the various typical molecular representations are presented consisting of the hard-sphere molecules, the variable-hard-sphere molecules, molecules represented by the inverse-power-law model and by the Lennard-Jones model. Some of the molecular representations are particularly suitable for certain fluid modelling methods which is why an understanding of these molecular representations is particularly important.

2.2.1 The hard-sphere model

A popular and relatively simple method for describing the behaviour of molecules is the fully elastic hard-sphere model (HS), Bird [6]. For a single-species gas the hard-sphere potential (describing the intermolecular interactions) is infinite if the molecular separation between two molecules, r, is smaller than the molecular diameter, d, and zero if r is larger than d. From this representation the derivation of the molecular mean free path of Eqn 2.4 can easily be realised.

It can be shown that Eqn (2.4) can be expressed using macroscopic parameters as:

$$\lambda_{\mathrm{HS}} = \frac{16}{5\sqrt{2\pi}} \frac{\mu}{\rho\sqrt{RT}}, \tag{2.6}$$

where μ is the dynamic viscosity, ρ is the mass-density, R is the specific gas constant and T is the gas temperature [28]. By combining Eqn (2.4) and Eqn (2.6) the hard-sphere diameter can be expressed as:

$$d_{\mathrm{HS}} = \sqrt{\frac{5}{16}\frac{\rho}{n\mu}\sqrt{\frac{RT}{\pi}}}. \tag{2.7}$$

The hard-sphere model thereby represents molecules as spheres having a fixed radius at which distance they have an unyielding surface for interactions with other molecules. If molecules with this representation collide with each other they will experience an instantaneous fully elastic collision. The trajectory of a colliding hard-sphere molecule is illustrated in Figure 2.2 indicated by the linear dashed path $P \to Q^* \to R$. This is an approximation to the more realistic case where intermolecular forces are present for every molecular separation distance, which is normally represented by a smooth-potential force. This molecular model is referred to as a *soft-sphere* model (SS) which is presented in sections 2.2.3 and 2.2.4. From the soft-sphere description a fictitious diameter of the molecules can be imagined, d_{SS}. This diameter indicates an estimated distance at which point molecules on average change directions and starts to move away from each other in a manner that results in approximately the same trajectory of movement in-between collisions as for the hard-sphere representation. The trace of a colliding smooth-potential molecule is outlined by the curved solid path $P \to Q \to R$. During a collision-state the trajectories of the two different molecular representations differ. However the molecular representations yield similar post collision effects, i.e. the molecular trajectories of the models converge at points P and R where the models obtains the same molecular velocities since elastic collisions are considered. Since the smooth-potential model is more complex than the hard sphere model the choice of a molecular representation might become important depending on whether the details of the molecular collisions or the free molecular flight is of special concern.

2.2.2 The variable-hard-sphere model

The variable-hard-sphere model is a version of the hard-sphere model derived by Bird [6] to be used with the DSMC flow simulation method (described in section 1.3). The main

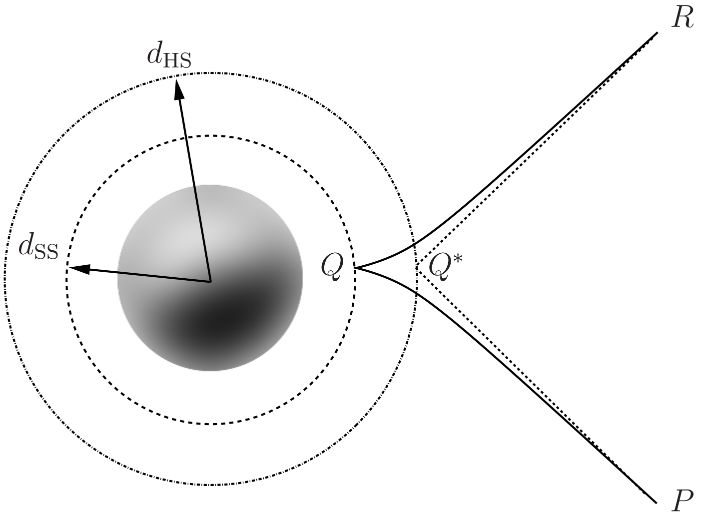

Figure 2.2: Illustration of a molecular trajectory during a molecular collision for both a hard-sphere model ($P \rightarrow Q^* \rightarrow R$) and for a smooth-potential model ($P \rightarrow Q \rightarrow R$). Here d_{HS} denotes the hard-sphere diameter and d_{SS} denotes a soft-sphere diameter.

idea of the variable-hard-sphere model is to consider that a molecule travelling with a lower velocity to be more likely to experience a collision than a molecule travelling at a higher velocity. This aspect is implemented through the variable-hard-sphere molecular diameter by allowing it to vary with molecular peculiar velocity as follows:

$$d_{\mathrm{VHS}} = d_{\mathrm{ref}}(\boldsymbol{C}_{\mathrm{ref}}/\boldsymbol{C})^{\upsilon}, \tag{2.8}$$

where a reference diameter d_{ref} and a reference molecular velocity $\boldsymbol{C}_{\mathrm{ref}}$ are used and υ is a model constant. The mean free path from the variable-hard-sphere is expressed as:

$$\lambda_{\mathrm{VHS}} = \frac{\mu}{\sqrt{2\pi RT}} \frac{2(7-2\omega)(5-2\omega)}{15}, \tag{2.9}$$

where $\omega = 1/2 + \upsilon$ is a constant that relates viscosity to temperature as $\mu \propto T^{\omega}$ and υ is a gas specific modelling parameter [6].

2.2.3 The inverse-power-law: Maxwell molecules

Another alternative to the hard-sphere molecular potential model is the inverse-power-law which belongs to the family of *soft-sphere models* (Kandlikar *et al.* [28]). The soft-sphere model has a smooth potential function of the form:

$$\Phi_{\mathrm{IPL}} = \kappa_{\mathrm{IPL}} / \left((\eta - 1)\, r_{ij}^{\eta-1} \right), \tag{2.10}$$

which acts on molecules i and j separated by a distance r_{ij} and κ_{IPL} and the exponent η are constant model parameters. From Eqn (2.10) the acting force between the molecules is calculated by:

$$F_{\mathrm{IPL}} = -\nabla \Phi_{IPL} = \frac{\kappa_{\mathrm{IPL}}}{r_{ij}^{\eta}}. \tag{2.11}$$

The function F_{IPL} is the acting force between two molecules and it is highly repulsive for short ranges and asymptotically approaches an negligible repulsive force for large r_{ij}.

An approximation to the hard-sphere model can be achieved by setting $\eta = \infty$ in Eqn 2.11 [28]. Similarly, *the Maxwell molecular model* is achieved by setting $\eta = 5$, which makes the collision probability independent of molecular velocities and thereby also the mean free path [6].

As early as 1879 Maxwell proposed the formulation for the mean free path for Maxwell molecules[1]:

$$\lambda_{\mathrm{MM}} = \frac{\mu}{\rho}\sqrt{\frac{\pi}{2RT}}, \tag{2.12}$$

which is about 2% lower than the mean free path value from the hard-sphere representation in Eqn (2.6) [28].

It can be assumed that molecules of an unbounded gas are equally likely to experience collisions whichever travelling direction they move in or if the trajectories are linear or curved. The latter is dependent on whether the molecules are affected by instantaneous or long-range potential interactions. Considering these assumptions, Eqn (2.4) can be related to Eqn (2.12), to obtain the diameter of a Maxwell molecule dependant on viscosity:

$$d_{\mathrm{MM}} = \sqrt{\frac{\rho}{\pi n \mu}\sqrt{\frac{RT}{\pi}}}. \tag{2.13}$$

2.2.4 Lennard-Jones: attractive and repulsive potential

A more realistic description of the molecular behaviour can be obtained using the short-range repulsive and long-range attractive smooth and continuous Lennard-Jones potential given by:

$$\Phi_{\mathrm{LJ}} = 4\epsilon\left[\left(\frac{\sigma}{r_{ij}}\right)^{12} - \left(\frac{\sigma}{r_{ij}}\right)^{6}\right]. \tag{2.14}$$

In Eqn (2.14), ϵ is related to the interaction strength of the molecules and σ corresponds to the distance at which point the potential between the two molecules is zero [29]. The interaction force between two Lennard-Jones molecules is

$$F_{\mathrm{LJ}} = -\nabla \Phi_{LJ} = 24\epsilon\left[2\left(\frac{\sigma^{12}}{r_{ij}^{13}}\right) - \left(\frac{\sigma^{6}}{r_{ij}^{7}}\right)\right]. \tag{2.15}$$

---

[1] The relation between λ and μ for Maxwellian molecules is derived in the section 2.4.1.

Usually the Lennard-Jones parameters σ and ϵ are set to specific values corresponding to certain molecules, which can be found in look-up tables, such as Maitland *et al.* [39]. The Lennard-Jones potential is mostly used for describing the behaviour of liquid flows meaning that alternative methods for finding these parameters might be needed for micro gas flows.

The Lennard-Jones parameters σ and ϵ can be related to the macroscopic parameters of temperature and viscosity according to Bird *et al.* [7]:

$$\sigma = \sqrt{\frac{5}{16}\frac{\rho}{n\mu\Omega_\mu}\sqrt{\frac{RT}{\pi}}}, \tag{2.16}$$

where Ω_μ is called the *collision integral for viscosity* affecting the molecular trajectories caused by binary collisions. The collision integral is a slowly varying function of the dimensionless temperature $T^* = k_B T/\epsilon$ [2] In case the molecules of a gas are described by a hard-sphere representation instead of a smooth-potential function then Ω_μ equals unity and σ equals the hard-sphere diameter, d_{HS}.

2.2.5 Comparison of molecular models

The use of various potential models influences what is considered as the molecular diameter, d and thereby also the length of the mean free path, λ. However, since the mean molecular spacing, δ_{sp}, is determined from the molecular number density this variable is not likely to be influenced by the choice of potential model.

In this section a comparison is made of the different potential models: the hard-sphere model, the inverse-power-law model and the Lennard-Jones model. The inverse-power-law is examined for both $\eta = 5$ (corresponding to Maxwell molecules) and $\eta = 100$ (which approaches the hard-sphere model). The molecular potential models are presented in Figure 2.3, where r_{ij} is normalised with σ for the Lennard-Jones model, and parameters κ_{IPL} and ϵ are set to unity.

It is seen that the hard-sphere model has a discontinuous potential shift from infinity at a separation distance of $r_{ij} < d$ to zero at a separation distance of $r_{ij} > d$. The inverse-power-law shows a smooth repulsive potential (for both $\eta = 5$ and $\eta = 100$) reaching infinity as r_{ij} approaches zero and approaches asymptotically zero at the repulsive side as r_{ij} reaches infinity. Finally, the more realistic molecular model of the Lennard-Jones potential is shown being both short-range repulsive and long-range attractive becoming infinitely repulsive as r_{ij} reaches zero, zero at $\sigma = 1$, and approaches asymptotically zero at the attractive side as r_{ij} reaches infinity.

---

[2] The function Ω_μ can be estimated by $\frac{1.16145}{T^{*0.15610}} + \frac{0.52487}{\exp(0.77320T^*)} + \frac{2.16178}{\exp(2.43787T^*)}$ [7].

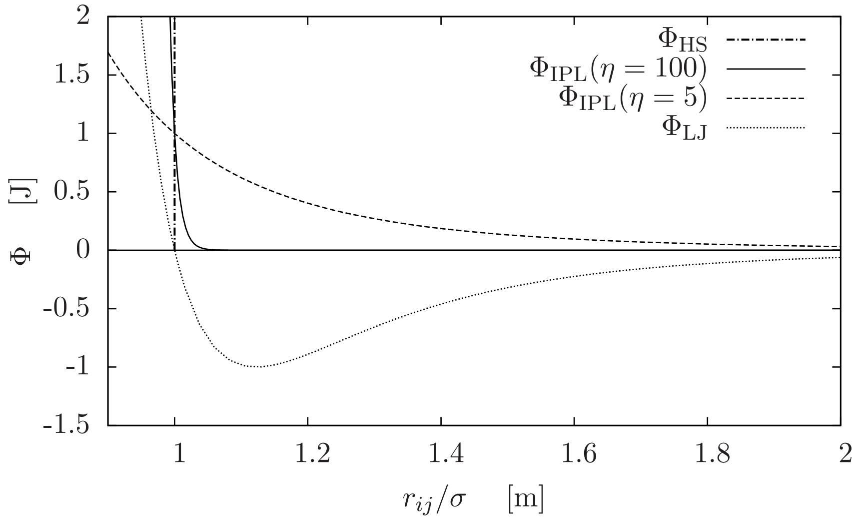

Figure 2.3: Potential energy [J] between molecules i and j for the hard-sphere model, inverse-power-law model (for both $\eta = 5$ and $\eta = 100$) and the Lennard-Jones model. Here the modelling parameters κ_{IPL} and ϵ are set to unity.

2.3 Maxwellian velocity distribution: a condition for equilibrium

A distribution function for molecular velocities in a gas at equilibrium was published in 1860 by Maxwell and has been fundamental to many of the fluid modelling techniques. The Maxwellian velocity distribution is valid for isotropic gases where there are no significant gradients of density, mass average velocity or temperature [7, 49].

From the Maxwellian velocity distribution, $f(\boldsymbol{C})$, the molecular speed distribution, $f(C)$, can be obtained by considering the magnitude of the velocities in the distributions having the form:

$$f(C) = 4\pi \left(\frac{1}{2\pi RT}\right)^{3/2} C^2 \exp\left(-C^2/2RT\right), \tag{2.17}$$

where C is the magnitude of $\boldsymbol{C}$ [65]. In Eqn (2.17) the likelihood for a molecule to have a particular speed is described from which it is possible to calculate some important quantities such as the most probable molecular speed C_{pr}, by

$$\frac{df(C)}{dC} = 0, \tag{2.18}$$

yielding

$$C_{pr} = \sqrt{2RT}. \tag{2.19}$$

The mean molecular speed, $\langle C \rangle$, is the mathematical average of the speed distribution:

$$\langle C \rangle = \int_0^\infty C f(C) dC = \sqrt{\frac{8RT}{\pi}}. \tag{2.20}$$

The root-mean-square speed, C_{rms}, is the square-root of the averaged squared speed, i.e.

$$C_{rms} = \left(\int_0^\infty C^2 f(C) dC \right)^{1/2} = \sqrt{3RT}. \tag{2.21}$$

The molecular speed distribution, $f(C)$, of Eqn (2.17) for neon gas at $273.13K$ having $R = 412.2\, [J/(kg\, K)]$ is illustrated in Figure 2.4 together with the corresponding typical speeds $C_{pr} = 474.52\, m/s$, $\langle C \rangle = 535.46\, m/s$ and $C_{rms} = 581.19\, m/s$. It is shown in section 4.5.2 that the Maxwellian velocity distribution can be used in numerical experiments to set molecular velocities in a random manner corresponding to a particular temperature.

The Maxwellian speed distribution is used in this thesis to theoretically couple the mean free path with viscosity in section 2.4.1. It is also used to analyse the experimental measurements of the mean free path in the close vicinity of a wall in section 4.5.2.

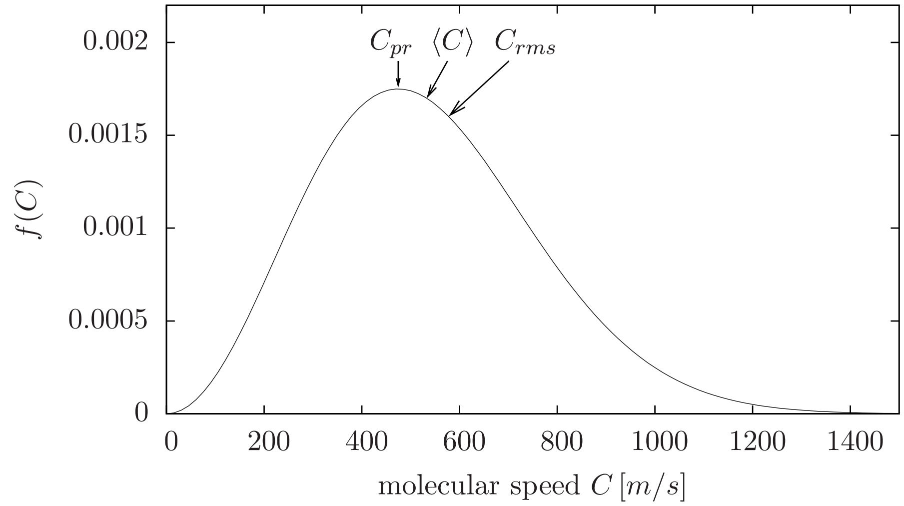

Figure 2.4: Maxwell's molecular speed distribution $f(C)$ from Eqn (2.17) together with the most probable speed, C_{pr}, the mean molecular speed, $\langle C \rangle$, and the root-mean-square speed, C_{rms}.

2.4 Navier–Stokes–Fourier models for micro gas flows

In this section the Navier–Stokes–Fourier equations are introduced. These equations are dependent on the properties viscosity and heat conductivity. Since this thesis focuses on the influence of molecular behaviour on isothermal cases the viscosity dependence on the unconfined mean free path is presented in section 2.4.1. The Navier–Stokes–Fourier equations are presented in section 2.4.2 and the used discontinuous boundary conditions are presented in section 2.4.3.

2.4.1 Viscosity: molecular transport of momentum

Before presenting the Navier–Stokes–Fourier equations the important fluid property *viscosity* needs to be clarified. Viscosity for fluids with low molecular weight can simply be conceptualised and referred to as the substrate's resistance to flow [7].

A gas in a state of non-equilibrium is considered to have a non-uniform distribution of some macroscopic properties (flow velocity, temperature, composition, etc.). Because these properties are defined by molecular properties and molecular interactions they tend to diffuse due to random thermal molecular movements. Molecules can thereby transfer macroscopic properties by travelling from a region of one state to a region of a significantly different state. In this process, molecules travel in a random manner from a region where they are on average in equilibrium, to regions where they are out of equilibrium. The result of these molecular transport processes yields the appearance, at the macroscopic level, the well-known non-equilibrium phenomena of mass diffusion, momentum exchange and heat conduction [65]. However, due to this process differences tend to even out i.e. equilibrate over time if no outer influences are present. As an example, viscosity is a macroscopic gas property affecting the rate of momentum exchange.

In Newton's law of viscosity it is stated that the shear force per unit area (here referred to as the shear stress tensor, $\mathbf{\Pi}$) is proportional to the velocity gradient of the fluid, as follows:

$$\Pi_{\mathrm{xy}} = -\mu \frac{dv_{\mathrm{x}}}{d\mathbf{y}}, \tag{2.22}$$

where v_{x} is the $\mathbf{x}$-component of the velocity of the flow, and $\mathbf{y}$ is the direction normal to the velocity. In Eqn (2.22) the viscosity, μ, is a fluid property which can be empirically determined. However, as shown in this section, viscosity can also be determined from the elementary kinetic theory of gases.

A kinetic theory analysis of viscosity is considered in Figure 2.5 which shows a velocity profile changing only in the $\mathbf{y}$-direction. In this figure a molecule is illustrated leaving a plane at $(\mathrm{y} - a)$ having the corresponding velocity to this plane and arriving at a plane at y achieving the new velocity corresponding to this plane. This occurrence would result in the following momentum exchange between the two planes at $(\mathrm{y} - a)$ and y:

$$\Pi_{\mathrm{xy}} = Zm\ v_{\mathrm{x}}\big|_{\mathrm{y}-a} - Zm\ v_{\mathrm{x}}\big|_{\mathrm{y}}, \tag{2.23}$$

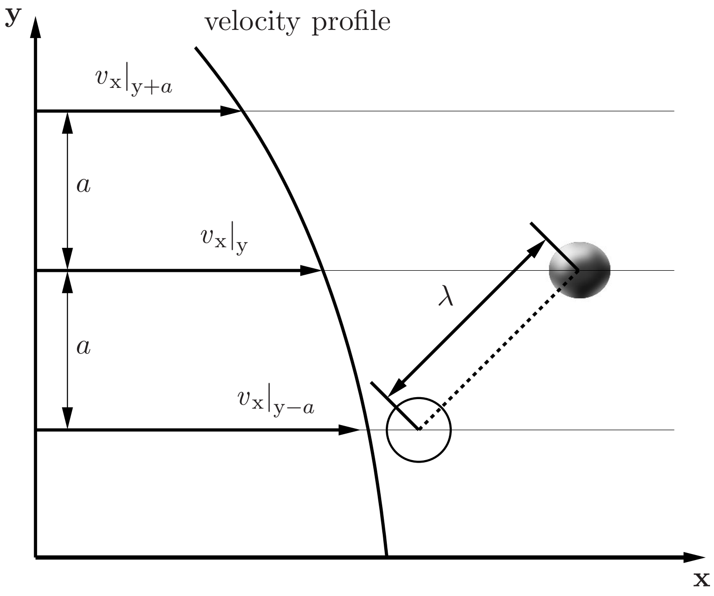

Figure 2.5: Molecular transport of momentum from the plane at $(\mathrm{y}-a)$ to the plane at y, where a is the vertical separation of the planes. Characteristic figure from [7].

where Z is a first approximation of the average number of molecules crossing the plane per unit area and per unit time from either side of this plane, represented by:

$$Z = \beta n C. \tag{2.24}$$

The coefficient β is a constant of proportionality which is set to 1/4 by Bird *et al.* [7] considering only molecules passing from in one direction of a plane and should therefore instead be 1/2 taking into account all molecules passing the plane. This coefficient is set to $0.499 \approx 1/2$ by Vincenti and Kruger [65] taking into account previous molecular collisions in addition to other second-order effects.

It is possible to use the rough approximation that the distance, a, is equal to the mean free path[3] and that the velocity profile between the two planes is linear [65]. The velocity for the plane at y can then be expressed as:

$$v_\mathrm{x}|_\mathrm{y} = v_\mathrm{x}|_{\mathrm{y}-a} + \lambda \frac{dv_\mathrm{x}}{d\mathbf{y}}. \tag{2.25}$$

By using Eqn (2.23) the following expression is achieved:

$$\Pi_\mathrm{xy} = -\beta n m C \lambda \frac{dv_\mathrm{x}}{d\mathbf{y}}. \tag{2.26}$$

---

[3] It can be realised by inspection of Figure 2.5 that a molecule has to travel strictly orthogonal to the flow direction in order for $a = \lambda$. Bird *et al.* [7] postulated that $a \approx 2/3\lambda$.

Now, if the average thermal molecular velocity

$$C = \sqrt{\frac{8RT}{\pi}}, \tag{2.27}$$

from the Maxwellian velocity distribution is inserted into Eqn (2.26) with the value $\beta = 1/2$ the relationship between the mean free path and viscosity is achieved by comparison to Eqn (2.22) i.e.:

$$\mu = \lambda\rho\sqrt{\frac{2RT}{\pi}}, \tag{2.28}$$

which can recognised from Eqn (2.12). It should be noted that this relationship requires that the gas is unbounded and far away from any solid surfaces. It is investigated in chapter 5 how a solid surface could influence Eqn (2.28) in a manner such that the molecular travelling distance a is shortened by gas–wall molecular collisions as well as gas–gas molecular collisions.

2.4.2 Navier–Stokes–Fourier equations

The continuum description of a gas is expressed by macroscopic quantities such as mass, velocity, pressure and temperature which are defined locally at every point of the gas. This section presents the traditional continuum model of the Navier–Stokes–Fourier equations, which can be obtained using the macroscopic quantities in balanced relations of continuity of mass and conservation of momentum and energy. If the gas flow is assumed to be isothermal it can be described using only the mass and momentum equations, which are then referred to as Navier-Stokes equations. The literature resource used in this section is mainly obtained from Bird *et al.* [7].

The equation of mass balance, also referred to as the *continuity equation*, can be expressed by considering the change of mass of a small stationary volume element in the following way:

$$\underbrace{\frac{\partial\rho}{\partial \mathrm{t}}}_{\boxed{\begin{array}{l}\text{rate of increase of}\\ \text{mass per unit}\\ \text{volume}\end{array}}} = \underbrace{-\left(\nabla\cdot\rho\boldsymbol{v}\right)}_{\boxed{\begin{array}{l}\text{net rate of mass}\\ \text{addition per unit}\\ \text{volume by convection}\end{array}}}, \tag{2.29}$$

where $\boldsymbol{v}$ is the mass average velocity. If the gas flow is modelled as incompressible the mass density remains a fixed quantity and Eqn (2.29) is reduced to:

$$(\nabla\cdot\boldsymbol{v}) = 0. \tag{2.30}$$

The equation of *momentum conservation* can be expressed by considering the change of momentum to a small stationary volume element due to acting processes in the following way:

$$\underbrace{\frac{\partial}{\partial \mathrm{t}}[\rho \boldsymbol{v}]}_{\boxed{\begin{array}{l}\text{rate of increase}\\ \text{of momentum per}\\ \text{unit volume}\end{array}}} = \underbrace{-[\nabla \cdot \rho \boldsymbol{v}\boldsymbol{v}]}_{\boxed{\begin{array}{l}\text{rate of momentum}\\ \text{addition by}\\ \text{convection per}\\ \text{unit volume}\end{array}}} \underbrace{-\nabla p \quad - [\nabla \cdot \boldsymbol{\Pi}]}_{\boxed{\begin{array}{l}\text{rate of momentum addition}\\ \text{by molecular transport per}\\ \text{unit volume}\end{array}}} \underbrace{+\rho \boldsymbol{g}}_{\boxed{\begin{array}{l}\text{external}\\ \text{force on}\\ \text{fluid per}\\ \text{unit volume}\end{array}}}, \tag{2.31}$$

where p is the pressure and $\boldsymbol{g}$ is the gravitational force. The viscous stress tensor is derived from Newton's viscosity law [7] and can be expressed in the vector-tensor notation as:

$$\boldsymbol{\Pi} = -\mu \left\{ \nabla \boldsymbol{v} + (\nabla \boldsymbol{v})^t \right\} + \left(\frac{2}{3}\mu - \kappa \right) (\nabla \cdot \boldsymbol{v}) \, \boldsymbol{I}, \tag{2.32}$$

where κ is the bulk viscosity[4]. Here $\boldsymbol{I}$ indicates the unit tensor with components I_{ab}, and $(\nabla \boldsymbol{v})^t$ is the transpose of the velocity gradient tensor. For incompressible cases Eqn (2.32) is reduced to:

$$\boldsymbol{\Pi} = -\mu \left(\nabla \boldsymbol{v} + (\nabla \boldsymbol{v})^t \right). \tag{2.33}$$

There are two special cases of Eqn (2.31). The first is referred to as the Stokes flow equation and is achieved if the acceleration terms are neglected, yielding:

$$0 = -\nabla p - [\nabla \cdot \boldsymbol{\Pi}] + \rho \boldsymbol{g}. \tag{2.34}$$

The second case is achieved if the viscous forces i.e. $[\nabla \cdot \boldsymbol{\Pi}] = 0$ are neglected, which results in Euler's equation of motion given by:

$$\frac{\partial}{\partial \mathrm{t}} \rho \boldsymbol{v} = -\left[\nabla \cdot \rho \boldsymbol{v} \boldsymbol{v} \right]. \tag{2.35}$$

The *energy conservation equation* can be expressed by considering the rate of change of kinetic and internal energy to a sub-volume of a gas. This is due to the result of heat change and work acting on the system. The equation of energy can be expressed as:

---

[4] For monatomic gases κ equals zero.

$$\begin{aligned}\underbrace{\frac{\partial}{\partial \mathrm{t}}\left(\frac{1}{2}\rho\boldsymbol{v}^2+\rho e\right)}_{\boxed{\begin{array}{l}\text{rate of increase of}\\ \text{energy per unit}\\ \text{volume}\end{array}}} \quad = \quad & \underbrace{-\nabla\cdot\left(\frac{1}{2}\rho\boldsymbol{v}^2+\rho e\right)\boldsymbol{v}}_{\boxed{\begin{array}{l}\text{rate of energy addition}\\ \text{per unit volume by}\\ \text{convective transport}\end{array}}} \quad \underbrace{-\left(\nabla\cdot\boldsymbol{q}\right)}_{\boxed{\begin{array}{l}\text{rate of energy addition}\\ \text{per unit volume by heat}\\ \text{conduction}\end{array}}} \\ & \underbrace{-\left(\nabla\cdot p\boldsymbol{v}\right)}_{\boxed{\begin{array}{l}\text{rate of work done}\\ \text{on fluid per unit}\\ \text{volume by pres-}\\ \text{sure forces}\end{array}}} \quad \underbrace{-\nabla\cdot\left[\boldsymbol{\Pi}\cdot\boldsymbol{v}\right]}_{\boxed{\begin{array}{l}\text{rate of work done}\\ \text{on fluid per unit}\\ \text{volume by vis-}\\ \text{cous forces}\end{array}}} \quad \underbrace{+\rho\left(\boldsymbol{v}\cdot\boldsymbol{g}\right)}_{\boxed{\begin{array}{l}\text{rate of work done on}\\ \text{fluid per unit volume}\\ \text{by external forces}\end{array}}},\end{aligned} \tag{2.36}$$

where e is the internal energy and $\boldsymbol{q}$ is the heat-flux vector.

It is possible to express Eqn (2.36) in terms of temperature by using *Fourier's law* of heat conduction:

$$\boldsymbol{q} = -k\nabla T, \tag{2.37}$$

where k is the thermal conductivity, and by using the relation between the internal energy[5] and temperature given by:

$$e = c_v T, \tag{2.38}$$

where c_v is the specific heat at constant volume. Then the energy equation, without external forces, is represented in terms of temperature as:

$$\rho c_v\left(\frac{\partial T}{\partial \mathrm{t}} + \boldsymbol{v}\cdot\nabla T\right) = -p\nabla\cdot\boldsymbol{v} + \nabla\cdot\left[k\nabla T\right] + \boldsymbol{\Pi}\cdot\nabla\boldsymbol{v}. \tag{2.39}$$

The four quantities p, ρ, $\boldsymbol{v}$ and T are thereby coupled by the three balanced equations of mass, momentum and energy of Eqns (2.29), (2.31) and (2.36) respectively. For gases a fourth relationship is fulfilled by the *perfect gas law*,

$$p = \rho R T, \tag{2.40}$$

which often is used for closure of the Navier–Stokes–Fourier equations.

---

[5] The internal energy is here assumed to be the same as the translational energy, which is the case for monatomic gases.

2.4.3 Discontinuous boundary conditions

The compressible Navier–Stokes–Fourier equations can adequately predict micro gas flows up to about $Kn = 0.001$, using boundary conditions for tangential velocity and temperature which are set equal to the corresponding values of the solid boundaries (Barber *et al.* [5]). These boundary conditions are referred to as no-velocity-slip and no-temperature-jump. However, for larger Kn the quasi equilibrium state of the gas becomes invalid yielding that modelling modifications are needed at the boundaries.

The breakdown of the quasi equilibrium description and the significance of discontinuous velocity boundary conditions are illustrated in Figure 2.6. Here the mean free path and the mass average velocity for a rarefied Couette gas flow case is described, with the average molecular behaviour. In this figure to the left: a gas of a highly equilibrium state has a linear velocity profile and the gas at the boundaries has the same velocity as the boundaries. The centre figure shows a more rarefied gas where the molecules leaving the walls have on average a tangential velocity which is the same as the walls, in agreement with gases in the near-equilibrium state. In between the walls, a change of molecular velocities can only occur due to molecular collisions which are experienced after an average molecular travelling distance of one mean free path. The colliding molecules travelling to the left and to the right exchange momentum so that they end up with a post-collisional tangential velocity equal to the average of the tangential pre-collision velocities. A molecule that approaches a wall has therefore a tangential velocity which is not equal to the corresponding velocity of the approached wall. This tangential velocity difference is dependent on how many intermolecular collisions a molecule experiences travelling between the two walls. In a rarefied gas, therefore, molecules approaching a wall have, on average, a different velocity compared to the corresponding molecules of a quasi equilibrium gas approaching a wall. In a continuum description this is perceived as a discontinuity between the gas's tangential velocity and the velocity of the wall. It should be noted that in this representation it is assumed that the molecular interactions with the walls accommodate full momentum exchange so that reflected molecules on average leave a surface with the surface's tangential velocity. It is shown in the next section that many investigators assume that the momentum exchange in a collision between a molecule and a wall is not complete, which increases the amount of velocity-slip for rarefied flows even more.

The applicability of the Navier–Stokes–Fourier equations can be extended to about $Kn = 0.1$ by allowing a certain amount of discontinuity of tangential velocity and of temperature between the gas and nearby solid surfaces. These discontinuous boundary conditions are referred to as velocity-slip, $\boldsymbol{v}_{\text{slip}}$, and temperature-jump, T_{jump} defined as

$$\boldsymbol{v}_{\text{slip}} = \boldsymbol{v}_{\text{w}} - \boldsymbol{v}_{\text{wall}} \quad \text{and} \quad T_{\text{jump}} = T_{\text{w}} - T_{\text{wall}}, \tag{2.41}$$

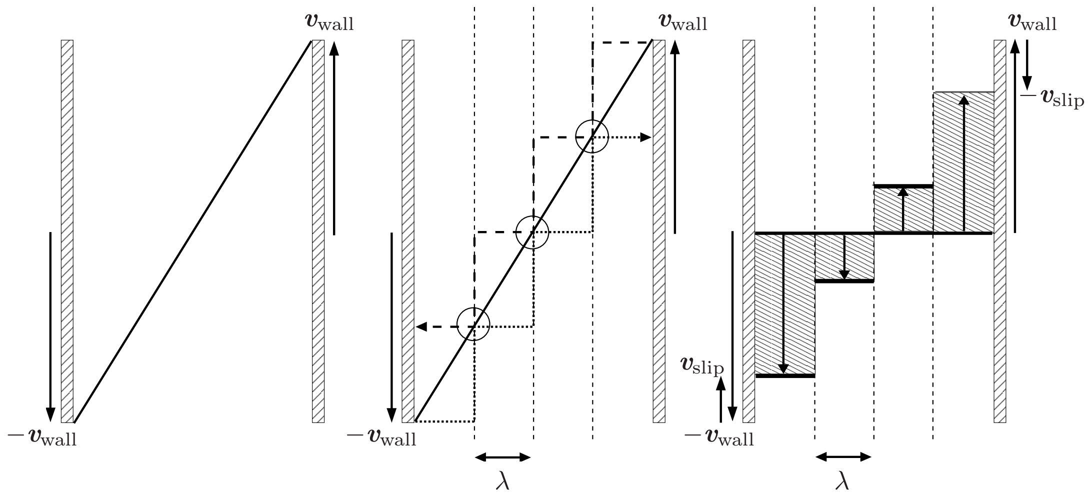

Figure 2.6: Illustration of the breakdown of the quasi equilibrium state and the slip modelling technique. The left figure illustrates a Couette flow case for a near-equilibrium gas where the gas is driven by the wall velocities, denoted by $\boldsymbol{v}_{\text{wall}}$ and $-\boldsymbol{v}_{\text{wall}}$. The centre figure shows the same case but for a rarefied gas, where the dashed arrows indicate molecules travelling from the left-hand-wall and the right-hand-wall. These velocities only change due to collisions (indicated by circles), which on average occur after a molecule travels a distance of λ. The right figure shows bins which have magnitudes equal to the average velocities of the molecules travelling to the left and to the right. The magnitude difference of the bins at the walls compared to the velocity of the walls can be interpreted as the velocity-slip, here denoted by $\boldsymbol{v}_{\text{slip}}$.

respectively. A common method for obtaining the velocity-slip and temperature-jump boundary conditions is to extrapolate the velocity or the temperature of the flow over the Knudsen layer, which for micro gas flows occupies a considerably large domain of the flow inherent of surface effects which the Navier–Stokes–Fourier equations cannot capture. With the use of these boundary conditions the bulk of the gas-flow can still be adequately predicted. The region $0.001 < Kn < 0.1$, in which the Navier-Stokes equations require discontinuous boundary conditions, is referred to as the *slip-flow regime*. This regime is represented in Figure 1.1.

In the following sections the velocity-slip boundary condition by Maxwell [42] is presented as well as the corresponding temperature-jump by von Smoluchowski [66], both having a first-order accuracy on Kn. The velocity-slip by Maxwell is shown to depend on certain coefficients which describe the molecular reflections of molecules when colliding with solid boundaries. Also, the second-order velocity-slip and temperature-jump boundary conditions are presented. The second-order velocity-slip is derived from an expansion of the first-order velocity-slip expression using λ as a smallness parameter.

First-order boundary conditions

Using kinetic theory, Maxwell showed the existence of velocity-slip [42]. The description derived by Maxwell considers molecular reflections from solid surfaces, which are either specular reflections, diffusive reflections or a mixture of the two (Figure 2.7). If the reflections of the molecules are diffusive the molecules are adsorbed by the surface (due to surface roughness of the wall, or due to a condensation–evaporation process) [28] and their tangential momentum is, on average, lost relative to the wall as they are re-emitted. For specular reflections, however, the molecular tangential momentum is retained and the momentum in the normal direction is mirrored in the normal direction of the wall. These different types of wall reflections are modelled using the *tangential momentum accommodation coefficient*, $\sigma_{\boldsymbol{v}}$, which is set to $\sigma_{\boldsymbol{v}} = 1$ for purely diffusive reflections and $\sigma_{\boldsymbol{v}} = 0$ for purely specular reflections.

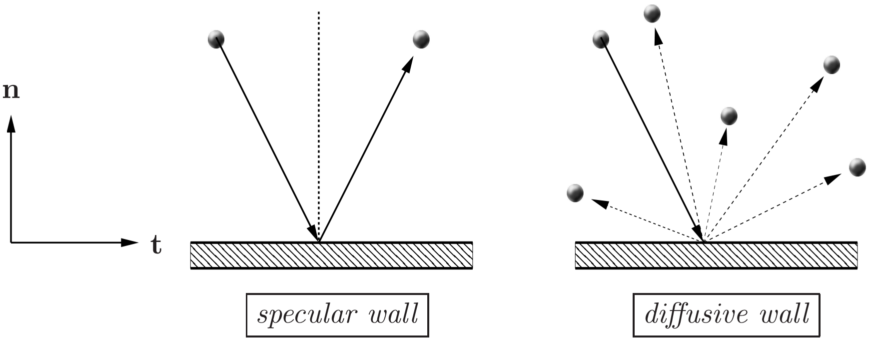

Figure 2.7: Left, specular reflections experienced by the fraction $(1-\sigma_{\boldsymbol{v}})$ of all the molecules. Right, one incoming molecule has many alternative trajectories due to diffusive reflections with the wall, which is experienced by the fraction $\sigma_{\boldsymbol{v}}$ of all reflected molecules. The axes indicate the wall normal direction, $\mathbf{n}$, and the wall tangential direction, $\mathbf{t}$.

The velocity-slip boundary condition originally proposed by Maxwell [42] has the following form:

$$\boldsymbol{v}_{\text{slip}} = -\frac{2-\sigma_{\boldsymbol{v}}}{\sigma_{\boldsymbol{v}}}\frac{\lambda}{\mu}\boldsymbol{\tau}_{\text{w}} + \frac{3}{4}\frac{Pr(\gamma-1)}{\gamma\rho RT}(-\boldsymbol{q}_{\text{w}}), \tag{2.42}$$

where $\boldsymbol{\tau}_{\text{w}}$ is the viscous stress vectors tangential to the surface and $\boldsymbol{q}_{\text{w}}$ is the heat-flux vector determined at the wall, γ is the specific heat ratio and Pr is the Prandtl number given by:

$$Pr = \frac{c_p\mu}{\rho k}, \tag{2.43}$$

where c_p is the specific heat capacity at constant pressure. The viscous stress vector, $\boldsymbol{\tau}_{\text{w}}$, relates to the viscous stress tensor, $\mathbf{\Pi}$, through the expression $\boldsymbol{\tau} = (\mathbf{n}\cdot\mathbf{\Pi})\cdot(\boldsymbol{I}-\mathbf{nn})$ [33]. The second term in Eqn (2.42) gives rise to the *thermal creep* phenomenon which causes a flow in the direction of increasing temperature gradient since $\boldsymbol{q} = -k\nabla T$. For planar wall cases it is possible to rewrite Eqn (2.42) in terms of velocity and temperature gradients in the following form:

$$\boldsymbol{v}_{\text{slip}} = \frac{2-\sigma_{\boldsymbol{v}}}{\sigma_{\boldsymbol{v}}}\lambda \left.\frac{\partial \boldsymbol{v}}{\partial \mathbf{n}}\right|_{\text{w}} + \frac{3}{4}\frac{\mu}{\rho T}\left.\frac{\partial T}{\partial \mathbf{t}}\right|_{\text{w}} . \tag{2.44}$$

For isothermal non-planar cases Eqn (2.42) can be rewritten as

$$v_{\text{slip}} = \frac{2-\sigma_{\boldsymbol{v}}}{\sigma_{\boldsymbol{v}}}\lambda\left(\frac{\partial v_{\text{n}}}{\partial \mathbf{t}} + \frac{\partial v_{\text{t}}}{\partial \mathbf{n}}\right), \tag{2.45}$$

where v_{slip} is the tangential component of the velocity slip, v_{n} and v_{t} are the normal and tangential components of the gas velocity at the surface respectively (Barber *et al.* [5] and Lockerby *et al.* [33]).

The temperature-jump boundary condition by von Smoluchowski [66] is:

$$T_{\text{jump}} = \frac{2-\sigma_T}{\sigma_T}\left[\frac{2(\gamma-1)}{(\gamma+1)}\right]\left.\frac{1}{\rho R(2RT/\pi)^{1/2}}(-q_{\text{n}})\right|_{\text{w}}, \tag{2.46}$$

where σ_T is the *thermal accommodation coefficient* and q_{n} is the normal component of the heat flux vector. Perfect energy exchange between a gas and a solid surface corresponds to $\sigma_T = 1$ and no energy exchange to $\sigma_T = 0$. For planar wall cases it is possible to rewrite Eqn (2.46) in terms of a temperature gradient as:

$$T_{\text{jump}} = \frac{2-\sigma_T}{\sigma_T}\left[\frac{2(\gamma-1)}{(\gamma+1)}\right]\frac{\lambda}{Pr}\left.\frac{\partial T}{\partial \mathbf{n}}\right|_{\text{w}} . \tag{2.47}$$

The coefficients $\sigma_{\boldsymbol{v}}$ and σ_T can be calculated as:

$$\sigma_{\boldsymbol{v}} = \frac{\tau_{\text{inc}} - \tau_{\text{ref}}}{\tau_{\text{inc}} - \tau_{\text{w}}} \quad \text{and} \quad \sigma_T = \frac{dE_{\text{inc}} - dE_{\text{ref}}}{dE_{\text{inc}} - dE_{\text{w}}}, \tag{2.48}$$

respectively, where τ is the magnitude of the viscous stress vector tangential to the wall, dE is an energy flux and the subscripts inc, ref and wall refer to incident, reflected and solid wall conditions respectively.

As reported by Steckelmacher [59], it was recognised by Knudsen that the mode of scattering of gas molecules from surfaces was fundamental to his analysis. Knudsen postulated and found empirically that, under free molecular conditions, diffuse reflections was the most reasonable model to describe the gas–surface interactions. For engineering purposes, therefore, $\sigma_{\boldsymbol{v}}$ is usually set to unity. In an experimental investigation by Arkilic [2] it was found that argon, carbon dioxide and nitrogen all have $\sigma_{\boldsymbol{v}}$ values around 0.8 under standard temperature and pressure conditions in a silicon channel, which corresponds well to the expected MEMS conditions. It is found by Ewert *et al.*

[15], from experimental studies of pressurised gas flows for Kn ranging from 0.03 to 0.3, that $\sigma_v = 0.84$.

Results of σ_v are obtained using molecular dynamics by Sun and Li [61] for planar wall configurations at $Kn \approx 0.12$, showing that σ_v decreases from about 0.6 to 0.35 with temperatures rising from 100K to 350K. These results vary significantly from the normally used values of σ_v, but Sun and Li also show results where an approximate wall roughness increasing from about 0.5nm to about 1.4nm (relevant to micro and nano devices [61]) yields σ_v values starting at about 0.80 and increasing to about 0.84. The thermal accommodation coefficient was also measured by Sun and Li: σ_T has a value of about 0.35 for gases at 300K, when confined by walls with an approximate roughness of 0.7nm. This value is found by other investigators to be between 0.31 and 0.97 for various gases and surfaces, as listed by Karniadakis *et al.* [29].

Higher-order boundary conditions

It has been found that first-order slip/jump boundary conditions are not sufficient to model mass-flow rates in pressure-driven flows beyond about $Kn = 1$. They fail to predict the mass flow minimum phenomenon (see chapter 5). In order to achieve better correspondence to mass-flow rates and in general obtain better results for high Kn flow cases, a second-order velocity-slip boundary condition has been derived through an expansion series of the first-order velocity-slip, using λ as a smallness parameter. With this method better agreements can be acquired for mass-flow rates, at about $Kn = 1$, recovering the mass flow minimum (as is shown in section 5.1.2). For higher Kn the Navier–Stokes equations using the second-order boundary condition yields the non-physical result of unbounded mass-flow values [57]. This might be due to the fact that the Navier-Stokes equations are accurate to first-order in Kn, as mentioned in section 1.2, and might therefore only be applicable together with boundary conditions accurate to the same or lesser order of Kn. Mitsuya [43] has presented a 1.5-order velocity-slip model which is capable of capturing the mass-flow minimum which shows seemingly reasonable mass-flow rate results even beyond $Kn \approx 1$ compared to experiments such as Ewart *et al.* [15].

It should be noted that many investigators of micro gas flows including Gad-el-Hak [17], Karniadakis *et al.* [29] and Ewart *et al.* [15] argue that second-order velocity-slip boundary conditions may need to be used when modelling gas flows with continuum methods in the low Kn area of the transition regime. But since, the Navier–Stokes–Fourier equations are accurate to first-order in Kn they should not be used themselves in the transition regime. Instead, higher order continuum equations such as the Burnett equations should be used, or pure molecular modelling [17].

A derivation of a higher-order velocity-slip boundary condition is done by Karniadakis *et al.* [29] by calculating the velocities of the incoming and outgoing molecules in close proximity to a solid surface yielding the following expression:

$$\boldsymbol{v}_{\mathrm{w}} - \boldsymbol{v}_{\mathrm{wall}} = \frac{2-\sigma_{\boldsymbol{v}}}{\sigma_{\boldsymbol{v}}}\left[\lambda\left(\frac{\partial \boldsymbol{v}}{\partial \mathrm{n}}\right)_{\mathrm{w}} + \frac{\lambda}{2}\left(\frac{\partial^2 \boldsymbol{v}}{\partial \mathrm{n}^2}\right)_{\mathrm{w}}\right]. \tag{2.49}$$

The general second-order velocity-slip boundary condition has the following form:

$$\boldsymbol{v}_{\mathrm{slip}} = D_1\lambda\left(\frac{\partial \boldsymbol{v}}{\partial \mathrm{n}}\right)_{\mathrm{w}} - D_2\lambda^2\left(\frac{\partial^2 \boldsymbol{v}}{\partial \mathrm{n}^2}\right)_{\mathrm{w}}. \tag{2.50}$$

By comparison of Eqn (2.49) and (2.50) it can be seen that the D_1 and D_2 slip coefficients are set to 1 and -0.5 respectively if diffusive reflections are considered. There are numerous suggestions by different investigators concerning what values the coefficients D_1 and D_2 should be set to, as shown in Table 2.1. Some values are derived purely theoretically, whereas others have been obtained through comparisons with experimental results [15]. The commonly used values for D_1, seen in Table 2.1, have about the same range as for the $\sigma_{\boldsymbol{v}}$-based ratio in the first-order slip expression, i.e. the two extreme D_1 values of 1.1466 and 1 corresponds to $\sigma_{\boldsymbol{v}}$ values of 0.93 and 1 respectively. The D_2 parameter varies in a wider range from -0.5 to $5\pi/12$. In an investigation by Hadjiconstantinou [23] based on work by Cercignani and Daneri [9] it was found that the coefficients $D_1 = 1.1466$ and $D_2 = 0.647$ yield mass-flow rates that agree with experimental investigations up to $Kn \approx 0.4$. However, since the second term of Eqn (2.50) has a quadratic dependence of λ the mass-flow rate becomes unbounded as Kn increases beyond $Kn = 0.4$ if the length scale is kept fixed. Another approach has been investigated by Shen *et al.* [57] using a 1.5-order velocity-slip definition which shows the mass flow minimum, as well as a bounded mass flow rate for $Kn > 0.4$.

Table 2.1: Some proposed coefficients for second-order velocity-slip models [29].

Author and year	D_1	D_2
Cercignani (1963) [9]	1.1466	0.9756
Hadjiconstantinou (2003) [23]	1.1466	0.647
Deissler (1964) [12]	1.0	9/8
Schamberg (1947) [53]	1.0	$5\pi/12$
Hsia and Domoto (1983) [25]	1.0	0.5
Maxwell (1979) [30]	1.0	0
Karniadakis *et al.* (2005) [29]	1.0	-0.5

A second-order temperature-jump boundary condition is derived by Karniadakis *et al.* [29] using kinetic theory of gases, yielding the following expression:

$$T_{\mathrm{jump}} = \frac{2-\sigma_T}{\sigma_T}\left[\frac{2\gamma}{(\gamma+1)}\right]\frac{1}{Pr}\left[\lambda\frac{\partial T}{\partial \mathrm{n}}\bigg|_{\mathrm{w}} + \frac{\lambda^2}{2}\frac{\partial^2 T}{\partial \mathrm{n}^2}\bigg|_{\mathrm{w}}\right]. \tag{2.51}$$

It is expected that this second-order temperature-jump boundary condition should be used at relatively high Kn when the first-order temperature-jump boundary condition becomes invalid. However, it should be noted that since the D_2 coefficient of the second-order velocity-slip boundary condition in Eqn (2.49) has a different sign compared to what most investigators use, the second-order temperature-jump of Eqn (2.51) might experience a similar inconsistency.

Chapter 3

Geometry dependent effective mean free path: a new approach

Surface effects considerably influence gas flows in the Knudsen layer which, in the case of micro-scale systems, comprise a substantial volume of the total gas flow domain. The width of the Knudsen layer is usually assumed to have a thickness of the order of the mean free path Bird [6]. The non-equilibrium effects in the Knudsen layer are introduced by gas molecules interacting with solid surfaces [32] and the gas molecules will equilibrate their momentum with the surrounding environment by gas intermolecular collisions. The state of non-equilibrium caused by a wall should therefore be spatially extended in proportion to the probability of a collision-less trace of a molecule travelling a certain distance from a wall. Therefore, by studying the shape of the effective mean free path profile a more precise indication of the Knudsen layer extent should be obtained.

From a fluid dynamic and continuum viewpoint the conventional fluid properties of viscosity and thermal conductivity are implicitly defined by the characteristic travelling time between collisions of the gas molecules, as suggested by Stops [60]. However, if the length of the mean free path of the free gas molecules is comparable to the characteristic length scale of the finite system there will be a considerable number of molecules colliding with the walls as well as with other free molecules, causing a shortening of the mean free path. This causes the mean free path to become geometry dependent, here referred to as being effective with respect to the wall distance. In chapter 5 it is therefore investigated how the effective mean free path affects the transport parameter viscosity and in turn how this effects the Navier-Stokes equations. Similar research has been performed by Guo *et al.* [22] who adopted Stops effective mean free path formulation into the solution method of the Navier-Stokes equations.

In this chapter physical reasoning is used to derive an enhanced extension for the conventional mean free path definition incorporating the effect of gas molecular collisions with solid walls as well as intermolecular gas collisions. First the theoretical effective mean free path model derived by Stops is presented in section 3.1. This model is based on similar fundamental principles as the new model in section 3.2, but it differs in the way that it is calculated when applied to a particular geometry. In chapter 4 the theoretical models for the effective mean free path are compared to simulation results using numerical experiments based on molecular dynamics.

3.1 Stops' effective mean free path model

The idea of using transport parameters that are influenced by an effective mean free path can be traced back to Stops [60]. Stops theory is based on the probability density

$$p_d(D_{tr}) = \frac{1}{\lambda} \exp\left(-\frac{D_{tr}}{\lambda}\right), \tag{3.1}$$

describing the distribution of the molecular free path dependant on the molecular travelling distance D_{tr}. The conventional (unconfined) mean free path, when no solid boundaries are present, can then be obtained by integrating $p_d(D_{tr})$ with respect to the travelling distance, D_{tr}, from zero to infinity.

The effective mean free path expression developed by Stops, $\lambda_{\text{eff}(S)}$, is achieved by using solid-angle analysis and by shortening the upper integrational limit of D_{tr} from infinity to the distance of the confining wall. The integration of $p(D_{tr})$ then yields $\lambda_{\text{eff}(S)} = \lambda J_{(S)}(\mathrm{n}, \lambda, H)$ for gas molecules confined between planar walls, where H is the wall spacing and

$$\begin{aligned} J_{(S)}(\mathrm{n}, \lambda, H) =& \frac{1}{2}\left[2 + \left(\frac{\mathrm{n}}{\lambda} - 1\right)\exp\left(-\frac{\mathrm{n}}{\lambda}\right) - \left(\frac{\mathrm{n}}{\lambda}\right)^2 Ei\left(\frac{\mathrm{n}}{\lambda}\right)\right. \\ &\left. + \left(\frac{H-\mathrm{n}}{\lambda} - 1\right)\exp\left(\frac{H-\mathrm{n}}{\lambda}\right) - \left(\frac{H-\mathrm{n}}{\lambda}\right)^2 Ei\left(\frac{H-\mathrm{n}}{\lambda}\right)\right], \end{aligned} \tag{3.2}$$

where the function Ei is the exponential integral function defined as:

$$Ei(\mathrm{z}) = \int_1^\infty t^{-1} \exp(-\mathrm{z}t)\, dt. \tag{3.3}$$

Eqn (3.2) has been used by Guo *et al.* [22] for solving some micro-gas-flow cases with good results.

In the next section a model similar to $\lambda_{\text{eff}(S)}$ is derived but without the dependence on the Ei-function, which may therefore be easier to implement and more computationally efficient for micro gas flow calculations.

3.2 A new effective mean free path model

This new effective mean free path description is based on the integrated density function $p_d(D_{tr})$ defined in Eqn (3.1) but without setting a specific integration limit for D_{tr}. The resulting probability function is expressed by:

$$P(D_{tr}) = \int p_d(D_{tr}) dD_{tr} = Q - \exp\left(-\frac{D_{tr}}{\lambda}\right). \tag{3.4}$$

This function describes the probability for a molecule to travel a distance D_{tr} without experiencing a collision. The integration constant, Q, is set to unity so that the probability ranges from zero to one.

3.2.1 Planar wall case

First, the new λ_{eff} model is derived for a single planar-wall configuration, shown in Figure 3.1, where the molecule is only allowed to travel in the negative **n**-direction and its trajectory distance to the wall is D_{tr}^-. The variable θ^- denotes the equally probable zenith angle travelling directions, which is related to D_{tr}^- using $D_{tr}^- = (\mathrm{n})/\cos(\theta^-)$. For this description, it is assumed that the molecule has just experienced an intermolecular collision at its current wall normal position nB. The corresponding effective mean free path expression depending on the molecule's distance to the left-hand wall, λ_{eff}^-, is obtained by averaging $\lambda P(D_{tr}^-)$ with respect to θ^- in the range $[0, \pi/2]$. This is done by using the following mean integral theorem,

$$\lambda_{\text{eff}}^- = \lambda \frac{2}{\pi} \int_0^{\pi/2} \left[1 - \exp\left(\frac{D_{tr}^-}{\lambda}\right)\right] d\theta^-. \tag{3.5}$$

A more realistic description accounts for the possibility of a molecule to travel in both negative and positive **n**-directions, represented in the two-planar-wall configuration in Figure 3.2. Here the notation D_{tr}^+ is used for the molecular travelling distance in the positive **n**-direction, and θ^+ for the corresponding zenith angle, which are related using $D_{tr}^+ = (H - \mathrm{n}) / \cos(\theta^+)$. Thereby it is possible to calculate λ_{eff}^+ in a corresponding manner to λ_{eff}^-.

The effective mean free path is then the average of λ_{eff}^- and λ_{eff}^+ as follows:

$$\lambda_{\text{eff}} = \frac{1}{2}\left(\lambda_{\text{eff}}^- + \lambda_{\text{eff}}^+\right). \tag{3.6}$$

In case there is only one planar wall present Eqn (3.6) should be modified so that the λ_{eff}^- or λ_{eff}^+ is replaced with unity. The averaging of Eqn (3.6) is performed here

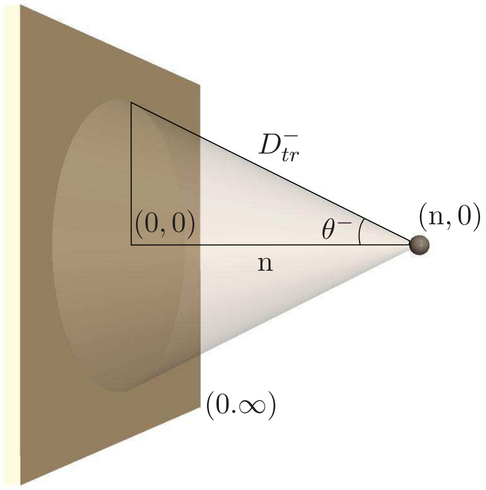

Figure 3.1: A molecule at a distance n from a planar wall. Possible trajectories for a molecule travelling in the negative **n**-direction described in cylindrical coordinates (n, n $\tan\theta^{-}$).

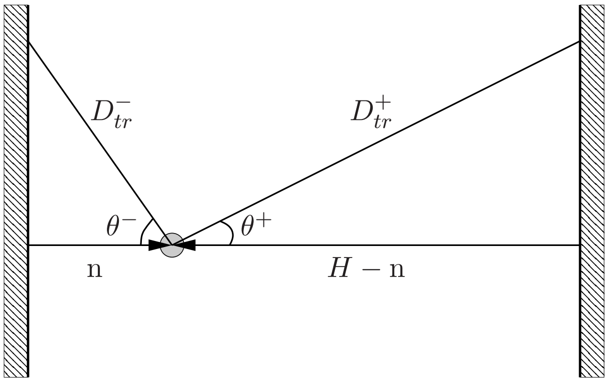

Figure 3.2: A molecule confined between two planar walls with spacing H. The minus and plus superscripts denote quantities corresponding to molecules travelling towards the left- and right-hand wall respectively. The molecule has an equal probability of travelling in any zenith angle direction θ^{-} or θ^{+}, or to travel in either the positive or the negative **n**-direction.

using Simpson's numerical integration involving 14 subintervals[1], resulting in $\lambda_{\text{eff}} =$

---

[1] The difference in mass flow results, calculated in section 5.1.2, for 14 and 16 integration intervals is 1.54% for $Kn = 1$, indicating that further increase of the number of integration intervals will only marginally affect the results.

$\lambda J(\mathrm{n}, \lambda, H)$ where,

$$\begin{aligned} J(\mathrm{n}, \lambda, H) = 1 - \frac{1}{82} \Bigg[& \exp\left(-\frac{\mathrm{n}}{\lambda}\right) + 4 \sum_{i=1}^{7} \exp\left(-\frac{\mathrm{n}}{\lambda \cos\left[\,(2\,i-1)\,\pi/28\right]}\right) \\ & + 2 \sum_{i=1}^{6} \exp\left(-\frac{\mathrm{n}}{\lambda \cos\left[\pi\, i/14\right]}\right) \\ & + \exp\left(-\frac{H-\mathrm{n}}{\lambda}\right) + 4 \sum_{i=1}^{7} \exp\left(-\frac{H-\mathrm{n}}{\lambda \cos\left[\,(2\,i-1)\,\pi/28\right]}\right) \\ & + 2 \sum_{i=1}^{6} \exp\left(-\frac{H-\mathrm{n}}{\lambda \cos\left[\,\pi\, i/14\right]}\right) \Bigg]. \end{aligned} \tag{3.7}$$

In the remainder of this thesis we will focus on the n-dependence of J, as λ and H are determined through the rarefaction parameter Kn, which will be given separately.

The J-functions from Stops model, Eqn (3.2), and from the new theory, Eqn (3.7), are compared in Figure 3.3 for four Kn: 0.04, 0.25, 1, 20 represented in a half channel. It can be seen that both models show similar results for all Kn-cases, with the largest difference at $Kn = 1$ where the new model has a slightly higher profile in most of the bulk of the channel cross-section. It should be noted that the half channel results of the $Kn = 0.04$ cases show very similar results to the case where one of the walls are modelled, due to the relatively large H compared to λ. By inspection of the $Kn = 0.04$ case, both models fulfil the physically intuitive requirements of

$$J(\mathrm{n} = H/2) \approx 1 \quad \text{and} \quad J(\mathrm{n} = H) \approx \frac{1}{2}. \tag{3.8}$$

The former requirement, for molecules far away from the walls, is based on that the effective mean free path should approach its conventional unconfined value. The latter requirement for molecules at the wall can be realised by considering the average of the equal probabilities of a molecule travelling in the direction towards the confining wall (not yielding any travelling length contribution) and the probability of it travelling into the bulk of the flow (yielding a contribution of the length λ). For $Kn = 0.25$, the channel is four unconfined mean free paths wide and since the effective mean free path almost achieves the conventional unconfined value at $\mathrm{n}/H = 0.5$ the Knudsen-layer can be estimated to be approximately two unconfined mean free paths wide. This estimation is in reasonable agreement with the estimation of Bird [6], noting that the Knudsen layer is in the order of one mean free path wide, and also in agreement with the estimation of one and a half as noted by Hadjiconstantinou [24].

For higher Kn, the entire $J(\mathrm{n})$ profile is lowered due to that the Knudsen layers of the left- and right-hand walls are overlapping, which can be explained by that molecules have a considerable likely-hood of colliding with either wall at any position of the.

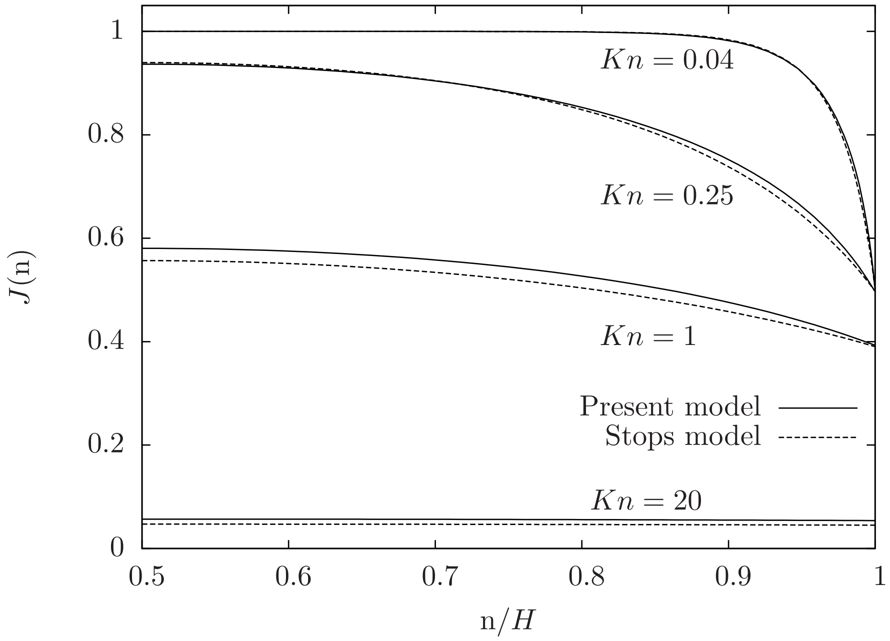

Figure 3.3: Comparison of different λ_{eff} models in a half-channel for different Knudsen numbers, where $\lambda_{\text{eff}} = \lambda J(\mathrm{n})$.

The basic physical requirement of decreasing $J(\mathrm{n})$ with increasing Kn can be seen by inspection of the considerably lower profile of the Kn_D case compared to the other cases. There is a third requirement, reported by Dongari *et al.* [14], which needs to be fulfilled by the new model: the profile should approach a value similar to the channel height H i.e.

$$\lambda_{\text{eff}}|_{Kn\to\infty} \approx H. \tag{3.9}$$

This requirement can be seen fulfilled for the Kn_D case, where $\lambda_{\text{eff}}/\lambda \approx 0.05$, by using the $\lambda = KnH$ relation as follows:

$$\frac{\lambda_{\text{eff}}}{\lambda} = 0.05 \Rightarrow \lambda_{\text{eff}} = 0.05 \times 20 \times H = H. \tag{3.10}$$

The $Kn = 0.25$ and $Kn = 1$ cases represent intermediate states between the $Kn = 0.04$ and $Kn = 20$ cases, where the profile near the wall is lower than the near-wall requirement in Eqn (3.8). This is because a molecule close to one of the walls has a significant probability of travelling directly to the other side of the channel and collide with that wall, which results in a contribution of less than one mean free path for this travelling direction.

3.2.2 Spherical obstacle case

Using the same theory as for the planar-wall case, the effective mean free path model may also be applied to the case of molecules in the close vicinity of a sphere (illustrated in Figure 3.4). In this case the molecule, at a distance r_d from the sphere centre, is as previously described equally probable to travel in any azimuthal angle, θ. There is an upper travelling distance limit, $D_{tr,u}$, associated with a critical limit for θ declared as θ_u, above which the molecule passes the sphere and travels into the bulk. This angle can be calculated by using the geometry of a formed right-angled triangle, as shown in Figure 3.4, having its right angle at the point connecting the imagined radius of the sphere and $D_{tr,u}$, which is tangential to the sphere. By inspection of this triangle the following relation is applied:

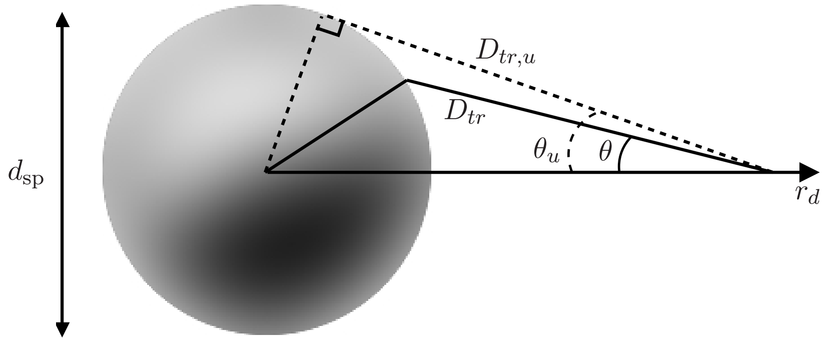

Figure 3.4: A molecule at a radial distance r_d from the centre of a spherical obstacle with diameter d_{sp}. The largest molecular travelling distance, D_{tr}, for a molecule traveling in the zenith angle θ. The largest zenith angle direction θ_u that a molecule can travel in and still intersecting the sphere, yielding the largest molecular travelling distance $D_{tr,u}$. Lines drawn are in a central cross section of the figure.

$$D_{tr,u}^2 + \left(\frac{d_{\text{sp}}}{2}\right)^2 = r_d^2. \tag{3.11}$$

By using the relation $D_{tr,u} = r_d \cos(\theta_u)$, the value of θ_u is obtained as:

$$\theta_u = \arccos\left[\frac{1}{r_d}\sqrt{r_d^2 - \left(\frac{d_{\text{sp}}}{2}\right)}\right] \tag{3.12}$$

The distance D_{tr} can be determined in terms of r_d and θ by using the cosine law:

$$\left(\frac{d_{\text{sp}}}{2}\right)^2 = D_{tr}^2 + r_d^2 - 2r_d D_{tr}\cos(\theta), \tag{3.13}$$

which yields:

$$D_{tr}(r_d,\theta) = r_d\cos(\theta) - \sqrt{r_d^2\cos^2(\theta) + \left(\frac{d_{\text{sp}}}{2}\right)^2 - r_d^2}. \tag{3.14}$$

The average distance from the molecule to the sphere's surface, with respect to the angle θ, is achieved by the following integral mean value theorem:

$$\langle D_{tr}\rangle = \frac{1}{\theta_u}\int_0^{\theta_u} D_{tr}(r_d,\theta)d\theta. \tag{3.15}$$

The mean free path for the molecules travelling in the direction of the sphere is achieved by,

$$\lambda_{\text{eff,sp}} = \frac{\lambda}{\theta_u}\int_0^{\theta_u} 1 - \exp\left(\frac{D_{tr}(r_d,\theta)}{\lambda}\right) d\theta, \tag{3.16}$$

in a similar manner to the one-wall case.

The complete effective mean free path expression is obtained by considering all possible molecular travelling directions (both towards the sphere and in directions that does not have an intersection with the sphere). This is achieved in a similar manner to the effective mean free path expression for a planar wall, in which case a probability of one half is used corresponding to the likelihood of a molecule travelling towards the planar wall instead of the bulk. Instead, here the solid angle theory is used to determine the likelihood of the molecule travelling in a direction of the sphere as opposed to travelling into the bulk expressed as $\sin^2(\theta_u/2)$ and $\left[1-\sin^2(\theta_u/2)\right]$ respectively. From this weighting the complete expression of the effective mean free path can be written as:

$$\lambda_{\text{eff}} = \lambda\left[1-\sin^2\left(\frac{\theta_u}{2}\right)\right] + \lambda_{\text{eff,sp}}\sin^2\left(\frac{\theta_u}{2}\right). \tag{3.17}$$

In Figure 3.5 three parameters involved in the calculation of λ_{eff} are plotted against r_d/λ, where $d_{\text{sp}} = 0.2\lambda$. In the top figure $\langle D_{tr}\rangle$ is plotted from Eqn (3.15), together with a dashed linear line for comparison. It can be seen that $\langle D_{tr}\rangle$ increases at a faster rate than the linear line for small r_d due to the fact that at this distance there is a large difference between $D_{tr}(r_d,\theta=\theta_u)$ and $D_{tr}(r_d,\theta=0)$. For large r_d it is seen that the $\langle D_{tr}\rangle$ profile becomes linear as $D_{tr}(r_d,\theta=\theta_u) \approx D_{tr}(r_d,\theta=0)$. In the middle figure the angle θ_u is plotted showing the fulfilment of the intuitive requirement of having a value of $\pi/2$ at the wall and approaching zero as r_d increases. In the bottom figure the resulting λ_{eff} of Eqn (3.17) is plotted. It can be seen that the λ_{eff} profile to a large extent has the same shape as an inverted shape of θ_u which suggests a dominating influence of this parameter.

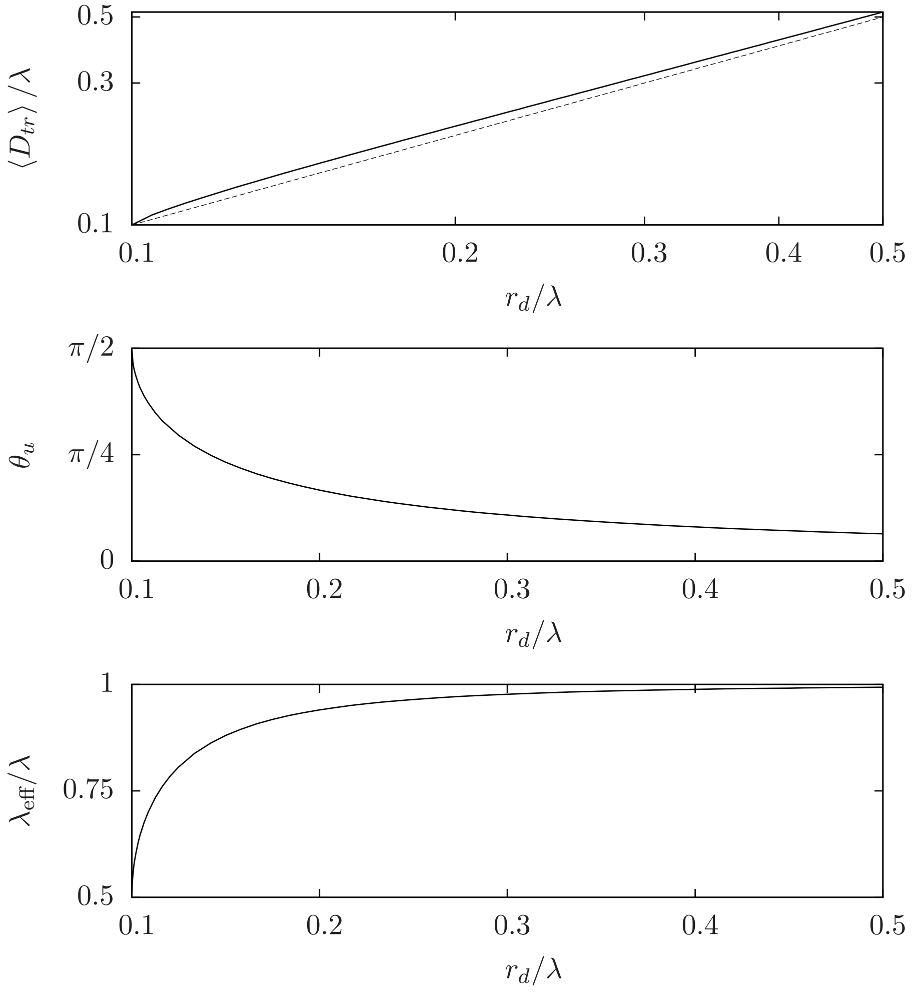

Figure 3.5: Three parameters involved in the calculation of λ_{eff} as a function of r_d/λ, where $d_{sp} = 0.2\lambda$. Top: travelling distance, D_{tr} of Eqn (3.14), when averaged over the angles zero to θ_u, together with a dashed linear line for comparison. Middle: the angle θ_u. Bottom: the resulting λ_{eff} of Eqn (3.17).

3.2.3 Spherical cavity case

Now the effective mean free path of a molecule in a spherical cavity is studied. As illustrated in Figure 3.6, (n) is the wall normal distance for a molecule inside the cavity with a diameter d_{cav}. Here, D_{tr} is the molecule's distance to the wall if the molecule at (n) has a travelling trajectory of θ. Also shown is the molecule's radial distance from the cavity's centre, C_{cav}, represented by r_d.

To calculate the effective mean free path, the wall distance of the molecule has first to be calculated using the cosine law:

$$\left(\frac{d_{\text{cav}}}{2}\right)^2 = D_{tr}^2 + r_d^2 - 2r_d D_{tr}\cos(\varphi), \tag{3.18}$$

where the angle $\varphi = \pi - \theta$ is used. The molecular travelling distance to the wall D_{tr}, dependent on r_d and φ, can then be expressed as:

$$D_{tr}(r_d,\,\varphi) = r_d\cos(\varphi) + \sqrt{r_d^2\cos^2(\varphi) + \left(\frac{d_{\text{cav}}}{2}\right)^2 - r_d^2}. \tag{3.19}$$

In terms of (n) and θ, this can be expressed as:

$$D_{tr}(\mathrm{n},\theta) = \left[\frac{d_{\text{cav}}}{2} - \mathrm{n}\right]\cos(\theta) + \sqrt{\left(\frac{d_{\text{cav}}}{2} - \mathrm{n}\right)^2\left[\cos^2(\theta) - 1\right]^2 + \left(\frac{d_{\text{cav}}}{2}\right)^2}. \tag{3.20}$$

As before, the average of this is achieved using Eqn (3.15) but here it is averaged in the range of θ from zero to π. The λ_{eff} expression is then obtained:

$$\lambda_{\text{eff}} = \frac{\lambda}{\pi}\int_0^{\pi}\left[1 - \exp\left(-\frac{D_{tr}}{\lambda}\right)\right]d\theta. \tag{3.21}$$

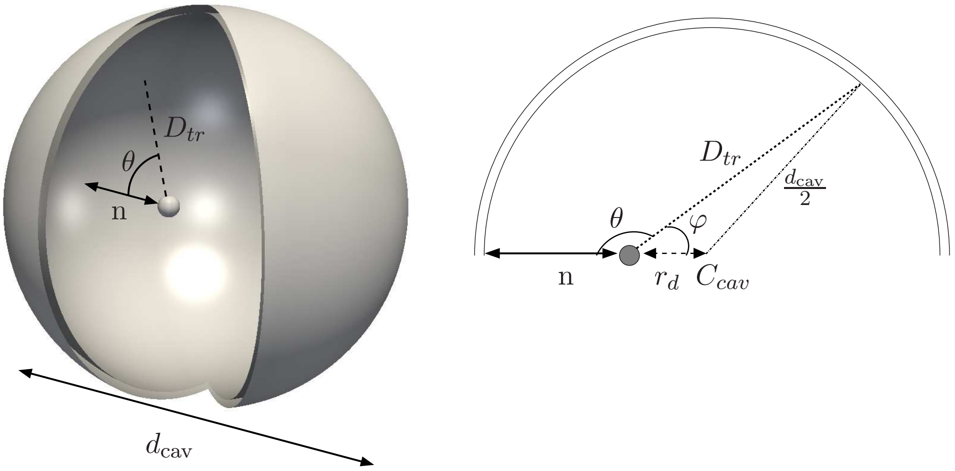

Figure 3.6: Left, a three-dimensional representation of a molecule in a spherical cavity of diameter d_{cav} at a wall normal distance of n. The molecule has the distance D_{tr} to the wall at a travelling direction of θ. Right, a two-dimensional view of the cavity illustrating the cavity's centre, C_{cav}, the molecule's radial distance, r_d, and the spherical cavity's radius $d_{\text{cav}}/2$. The angle $\varphi = \pi - \theta$ is used in the cosine law for calculating the effective mean free path.

The normalised results of the average molecular distance to the sphere's wall $\langle D_{tr}\rangle$ and the resulting effective mean free path of Eqn (3.21) are shown in Figure 3.7. The effective mean free paths are shown for the two cavity diameters of $d_{\text{cav}} = \lambda$ and $d_{\text{cav}} = 10\lambda$ corresponding to Kn of 1 and 0.1 respectively, these being based on a length scales equal to the cavity diameters.

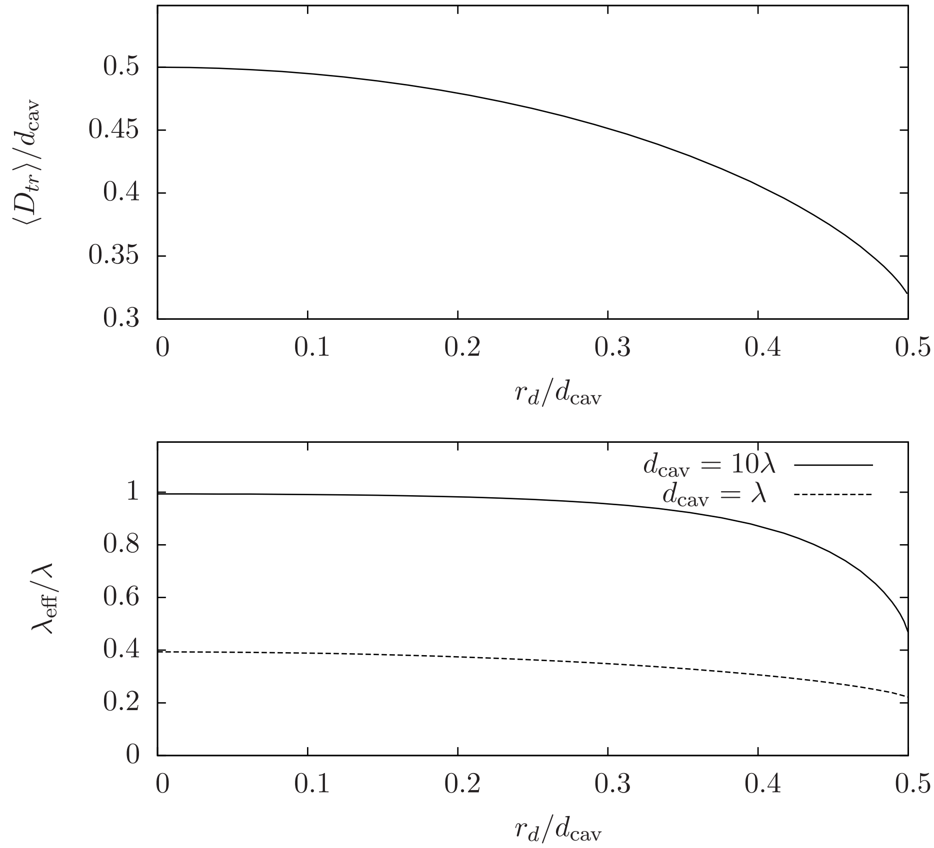

Figure 3.7: Top: the normalised average wall distance $\langle D_{tr} \rangle$. Bottom: the normalised effective mean free path for $d_{\mathrm{cav}} = 10\lambda$ and $d_{\mathrm{cav}} = \lambda$.

It should be noted that the average molecular distance to the sphere's wall shown in the top of Figure 3.7 is the same for all d_{cav}. The average wall distance show reasonable results, achieving a value of half the diameter in the centre of the cavity and a lower value of about 0.32 at the wall. The results of the effective mean free path are shown in the bottom sub-figure. Here the characteristic result for the case $d_{\mathrm{cav}} = 10\lambda$ is seemingly similar to the results of the two-planar-wall results, showing clearly that the near-wall value is close to half of the unconfined mean free path value and that the unconfined value is almost achieved in the centre of the cavity. For the $d_{\mathrm{cav}} = \lambda$ case the expected result of a lower flatter profile are observed. For this case the resulting low profile has a similar shape to $\langle D_{tr} \rangle$, because intermolecular collisions are relatively few causing the mean free path to be the same as the average wall distance.

3.3 Discussion

In this chapter a new theoretical expression for a geometry-dependent and effective mean free path is derived. This effective mean free path is dependant on the free path probability distribution of a molecule travelling a certain distance without experiencing a collision. By integrating this probability distribution, with respect to an unconfined space, from zero to infinity, the conventional unconfined value is obtained. Since this thesis is focused on micro gas flows in close vicinities to walls this method has been enhanced by integrating this probability function from zero to the distance of a confining wall instead. This upper limit is interpreted such that a molecule will experience a collision by hitting the wall which terminates its free path. By averaging this function for all possible travelling directions the effective mean free path is obtained. This new method has been applied to both planar- and non-planar-wall cases.

The developed effective mean free path for planar cases consists of both one- and two-wall confining geometries. For the one-planar-wall case at large wall distances the method fulfils the basic requirement of asymptotically approaching the unconfined mean free path value. In the near-wall region the requirement that the effective mean free path should reach half the value of the unconfined mean free path is obtained. The effective mean free path for the two-planar-wall case fulfils an other requirement showing similar results as for the one-wall case where the two walls are far apart. When the two walls are at a distance of about four unconfined mean free paths from each other it is observed that there is a significant overlapping effect from the two walls causing the effective mean free path in the middle of the channel not to tend to the unconfined value. Where the walls are at a distance of one twentieth of the unconfined mean free path from each other the effective mean free path obtains a flat profile having roughly the value of the channel separation distance, which fulfils a third requirement noted by Dongari *et al.* [14].

For the non-planar-wall cases both a spherical obstacle case and a spherical cavity case are considered. The new effective mean free path results for the spherical obstacle case is studied for a sphere with a diameter of 0.2λ. The results show that the effective mean free path, for this case, has a profile which is largely dependent on the upper travelling trajectory angle, which a molecule can travel in, in order to tangentially collide with the sphere. The effective mean free path profile, for this case, is shown to have a sharper increase in the near-wall region compared to the one-planar-wall case because compared to the one wall case the sphere does not “block” travelling directions for a molecule travelling in an opposite direction to the wall normal. The effective mean free path results of the spherical cavity case fulfils the requirement of nearly achieving the unconfined mean free path value in the centre of the cavity, if the diameter of the sphere is large enough. When the sphere diameter is small in comparison to the mean free path it is observed that the effective mean free path reaches a profile similar to the mean distance to the walls, which is reasonable since intermolecular gas collisions are less likely.

In the next chapter the new and Stops' λ_{eff} models are compared to some numerical experiments performed using the method of molecular dynamics.

Chapter 4

Validation using molecular dynamics

To simulate the mean free paths of noble gases, the open source software OpenFOAM (Open Field Operation and Manipulation) [1] is used with the molecular dynamics routines implemented by Macpherson *et al.* [37, 35]. The molecular dynamics method is often used to simulate liquids at the nano-scale because liquid molecules are believed to experience constant molecular interactions, which are considered to be correctly taken into account using this method. The argument for simulating domains at the nano-scale is simply that at such a small scale the liquid is comprised of a manageable number of molecules. The molecular dynamics method is chosen here for simulating gases at standard temperature and pressure (STP). This model is attractive for the purpose of estimating the mean free path because it is the only deterministic approach available and it allows for realistic molecular behaviour, i.e. molecular attractions, repulsions, movements and scatterings. It is, however, possible to simulate larger domains for gases than for liquids. This is due to the fact that the density of gases is much lower than the density of liquids and due to that the density of a gas is linearly proportional to the number density of molecules in that gas yielding considerably larger separation distances between gas molecules than for liquid molecules. Thereby fewer gas molecules than liquid molecules are modelled in the same volume domain.

There is however a difficulty in simulating the boundary walls explicitly, consisting of molecules in an arranged structure. This is because walls are about as dense as liquids and therefore require a large number of molecules to be represented. Explicit walls therefore need to be very thin (just a few molecular layers) in order for the simulation not to be too computationally expensive. Due to the expensive simulations of explicit walls it is quite common to simulate walls implicitly, in which cases they are replaced by a surface which reflects molecules specularly, diffusively or in a combination of the both. In this chapter the default molecular dynamics solver is enhanced by implementing features allowing it to measure the unconfined mean free path and the effective mean free path affected by both implicit and explicit walls.

To begin with, the theoretical unconfined mean free path values are evaluated for a hard-sphere gas and Maxwellian gas using Eqn (2.6) and (2.12) respectively. The mean free path for Maxwellian molecules is used for normalisation purposes in this thesis. In such cases, where the subscript of the mean free path is omitted it should be interpreted as being for a Maxwellian gas. The theoretical mean free path values of the two representations are calculated for helium, neon and argon gas at STP. Noble gases are considered because they are composed of monatomic molecules which only have translational motion, and therefore no molecular vibrational or rotational energies are present. This makes the noble gases easier to interpret theoretically and to model using molecular dynamics. Table 4.1 lists the gas parameters used for calculating the theoretical mean free paths. Here the specific gas constant has been calculated using $R = R_\mathrm{u}/M$, where R_u is the universal gas constant of 8.3145 [J/(mol K)]. It should be noted that the mean free path of the hard-sphere model is greater by a factor of $16/5\pi \approx 1.02$ then that of Maxwellian molecules [28]. The molecular masses of the gases helium, neon and argon can be calculated by M/N_Av, where N_Av is Avogadro's constant equal to 6.0221367×10^{23} molecules per mol.

Table 4.1: Gas data of standard temperature and pressure [47].

Gas:	He	Ne	Ar
$\mu \times 10^6$ [kg/(m s)]	18.2	29.7	20.8
ρ [kg/m^3]	0.178	0.900	1.784
M [kg/kmol]	4.00	20.18	39.95
R [J/(kg K)]	2077.3	412.2	208.1
$\lambda_\mathrm{MM} \times 10^7$ [m]	1.696	1.233	0.613
$\lambda_\mathrm{HS} \times 10^7$ [m]	1.728	1.256	0.624

4.1 Intermolecular potentials in the molecular dynamics simulation and the determination of a collision

In the molecular dynamics simulation the Lennard-Jones molecular interaction potential, Φ_LJ, presented in Eqn (2.14), is used. It is here chosen to set σ equal to the hard-sphere diameter of a monatomic gas in order to relate the molecular dynamics measurement of the mean free path to the theoretically derived mean free path. The σ parameter is determined using the relationship to viscosity, in Eqn (2.16) by setting the collision integral for viscosity $\Omega_\mu = 1$. With σ it is possible to calculate the theoretical hard-sphere value of the mean free path, using microscopic parameters, by Eqn

(2.6). This gives the same values as in Table 4.1, i.e. 1.728×10^{-7}m, 1.256×10^{-7}m and 0.624×10^{-7}m for helium, neon and argon respectively.

An experiment has been performed by Well *et al.* [64] where the sound damping is related to the Lennard-Jones parameters using an experiment of neutron scattering of liquid neon. In this thesis the parameter ϵ is chosen so that the ratio of the reduced sound damping factor, Γ^*, to the sound damping factor,

$$\frac{\Gamma^*}{\Gamma} = \frac{1}{\sigma}\sqrt{M/\epsilon}, \tag{4.1}$$

presented by Well *et al.* [64], retains the same values as for the commonly applied Lennard-Jones parameters for liquids (denoted by a prime symbol). The sound damping coefficient is defined as

$$\Gamma = \left[\mu/\rho + (\gamma - 1)\alpha\right]/2, \tag{4.2}$$

where γ is the specific heat ratio and $\alpha = k(\rho c_p)^{-1}$ is the thermal diffusivity.

Since the molecular mass is independent of the choice of Lennard-Jones parameters ϵ is obtained from the relation $\epsilon = \sigma'^2\epsilon'/\sigma^2$, under the assumption that this law is appropriate to scale liquid to gas properties in the same way as between liquid properties. The relation of Eqn 4.1 is adopted in research by Guarini *et al.* [21] investigating molecular scattering angles.

The σ and ϵ values are presented in Table 4.2 for the monatomic gases helium, neon and argon. The commonly used Lennard-Jones parameters for liquids, used for scaling, are denoted by a prime symbol.[1]

Table 4.2: Lennard-Jones parameter data. Prime notation indicates commonly used data, where data for helium is from [6] and data for neon and argon is from [7]. The prime notated parameters are used here for scaling ϵ.

Gas:	He	Ne	Ar
$\sigma' \times 10^{10}$ [m]	2.576	2.720	3.405
$\epsilon' \times 10^{22}$ [J]	1.4083	6.4891	17.2857
$\sigma \times 10^{10}$ [m]	2.2024	2.5836	3.6614
$\epsilon \times 10^{22}$ [J]	1.9266	7.1924	14.9496

The potential, Φ, of the Lennard-Jones model is shown in Figure 4.1 for helium, neon and argon together with their corresponding forces. Here it is possible to distinguish

---

[1] The sensitivity of ϵ on the mean free path is tested in this thesis for neon gas, where it is found that by reducing ϵ by one half resulted in an ϵ value of 3.5979×10^{22}J decreases the mean free path by about 0.16%, so the solution is considered to be relatively insensitive to this parameter.

the effect of the first and second terms in the Lennard-Jones potential. The former is repulsive short-ranged, dominating to the left in the figures, and the latter is attractive and long-ranged, dominant to the right. It is seen that argon gas has the highest ϵ value with the deepest potential well, and it therefore also has the strongest interaction force. It is seen that σ corresponds to the molecular separation distance where the molecular potential switches between positive and negative.

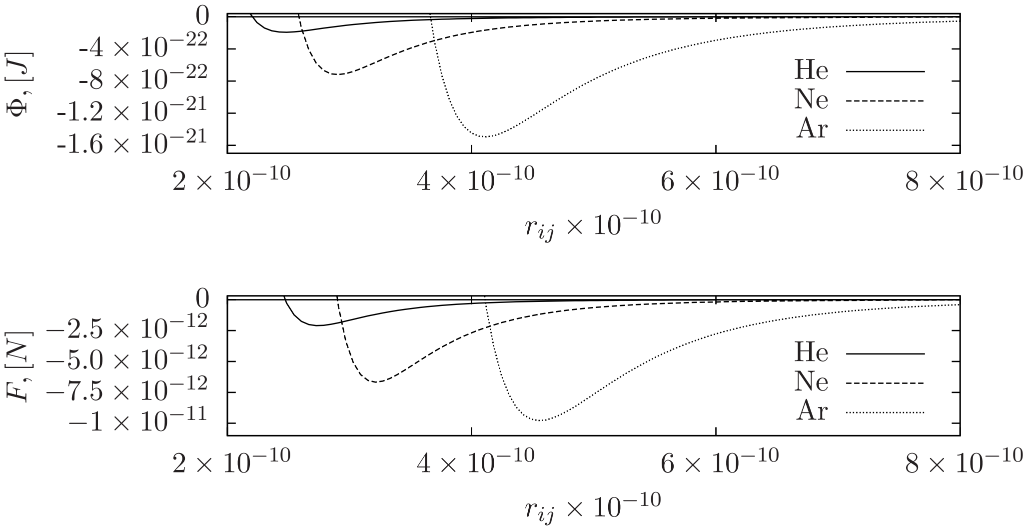

Figure 4.1: Top: the potential energy [J]. Bottom: potential force [N]. Potential energy and potential force between molecules i and j for helium, neon and argon.

In order to be able to compare the conventional definitions of the mean free path given by Eqns (2.6) and (2.12) with molecular dynamics the definition of a collision needs to be defined. Since molecular dynamics already uses a “closeness parameter” given by σ, which is described as being similar to the molecular diameter by authors such as Karniadakis *et al.* [29], a collision is here considered to occur if two molecules are closer to each other than this distance.

In the implementation of the mean free path recording in molecular dynamics the travelled distance of a molecule since it last experienced a collision, i.e. the free path, is continuously assigned to the current position of the molecule. The mean free path value is expected to be recovered when this distance is averaged over all molecules, in the space of the cell of the geometry, and over a certain time interval. This simulation method is different from the intuitive method of directly measuring a molecule’s travelled distance between two successive collisions, which can only be recorded when a collision occurs. For this approach the measurement of the mean free path the free path needs to be assigned to a specific point, which is difficult to determine because

Table 4.3: Theoretically based molecular data for helium, neon and argon: the most probable molecular speed (Eqn 4.3) , C_{pr}, the average time period between collisions (Eqn 4.4) , τ_{col}, and the corresponding average number of collisions per molecule during the simulated time of 3 nano seconds, N_{col}.

Gas:	He	Ne	Ar
C_{pr} [m/s]	1065.28	474.52	337.19
$\tau_{\text{col}} \times 10^{10}$ [s]	2.22	2.60	1.82
N_{col}	13.5	16.5	11.6

it is unclear where, between the two successive collisions, the free path should be assigned. An advantage of the former method, used in this thesis, is that data recording of the collision-less molecular travelling distance can be programmed to be a molecular attribute, together with the usual attributes such as the molecular position and the molecular velocity, and is thereby easy to implement and handle.

For the recording of the mean free path the length of the simulation time period has to be determined. In this thesis this simulation time is chosen based on the time it takes for the mean free path recording, starting at zero, to stagnate at a constant value. The stagnation is shown to occur for all tested cases after roughly 1.5 nano seconds. The simulation time for the recording of the mean free path has therefore to be longer than this time and is most often chosen to be twice as long, i.e. 3 nanoseconds, as is shown in subsection 4.5.1.

It is also interesting to determine how many collisions on average a molecule experiences during these simulations. Using the theoretical mean free path value, λ, this can be estimated by calculating the average collision time period given by:

$$\tau_{\text{col}} = \frac{\lambda}{C_{pr}}, \tag{4.3}$$

where

$$C_{pr} = \sqrt{2RT}, \tag{4.4}$$

is the most probable molecular speed in the Maxwellian velocity distribution. For the given gas conditions the speeds listed in Table 4.3 are obtained.

4.2 Geometry and periodic boundaries

The first aim is to validate the measurement of the mean free path by recovering the conventional value of the unconfined mean free path of helium, neon and argon gas (unaffected by any solid boundaries). In this attempt it is chosen to simulate a cube-shaped geometry with periodic boundaries. Periodic boundaries transfer any molecule that passes into them to a perpendicular position on the opposite boundary of the cube, keeping all of the molecule's attributes, except its position.

An important issue in this validation is choosing an appropriate edge length of the simulated cube geometry. Ideally a large cube should be modelled but since the computational cost of molecular dynamics is severe for a gas at STP conditions at the micro-scale[2] it is important to find the smallest volume of a cube that still presents reasonable results. In order to study whether the volume of the studied gas has an effect on the mean free path, it is chosen here to simulate three cases of various size of the cube domain for neon gas. These cases are labelled after their side lengths defined by their relation to the theoretical unconfined mean free path value of neon, λ_{Ne}. The three cases are:

$$l_A = 0.5\lambda_{\mathrm{Ne}}, \qquad l_B = \lambda_{\mathrm{Ne}} \quad \text{and} \quad l_C = 1.5\lambda_{\mathrm{Ne}}. \tag{4.5}$$

The helium and argon gases are simulated using the side length of $l_B = 1.0\lambda_{\mathrm{Ne}} = 1.23310^{-7}$ m. This case corresponds to side- lengths of $0.73\lambda_{\mathrm{He}}$ and $2.01\lambda_{\mathrm{Ar}}$ for helium and argon respectively, where λ_{He} and λ_{Ar} are the theoretical unconfined mean free paths of helium and argon.

A mesh is applied to the l_A, l_B and l_C cases consisting of 6^3, 12^3 and 16^3 cells respectively. The numbers of cells are chosen so that there are more than 10 simulated molecules on average per cell, and so that the cells are relatively small as this will decrease the computational time cost [35]. It should also be noted that no dependence of the grid has been observed to influence the results of the recorded mean free path, although this has not been investigated separately. The geometry domain is illustrated in Figure 4.2.

4.3 Implemented attributes for recording the free path

In this section the proceedure of implementing the required feature of recording the mean free path in the default molecular dynamics solver is presented.

Due to the periodic boundary conditions it is not convenient to directly record the travelled distance of the molecule as a difference between the current position of the molecule and the position of its last collision, as illustrated in Figure 4.2, i.e. the distances $P_1 \rightarrow P_2$ is not the same as $P_1 \rightarrow P_3 \rightarrow P_4 \rightarrow P_5 \rightarrow P_6 \rightarrow P_2$. Instead the

---

[2] The typical computational cost of molecular dynamics scales as the square of the number of simulated molecules, but this molecular dynamics simulation has a computational cost with a linear dependency on the number of simulated molecules [37, 35].

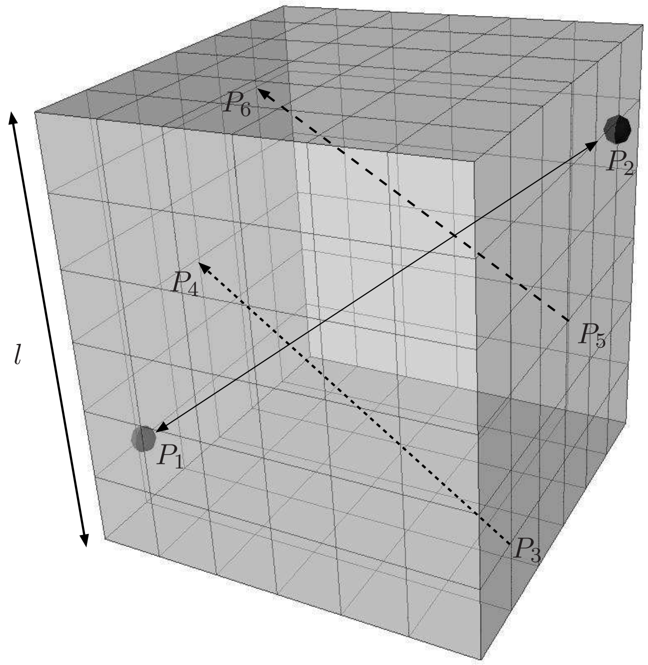

Figure 4.2: An example of the simulated cube geometry with periodic boundary conditions on all faces. The cube consists of either 6^3, 12^3 or 16^3 cells for the l_A, l_B and l_C cases, respectively. The edge length of the cube, l, is illustrated. An example is shown of how a molecule travels from point P_1 to P_2 through the periodic boundaries (by dashed arrows), in the order $P_1 \rightarrow P_3 \rightarrow P_4 \rightarrow P_5 \rightarrow P_6 \rightarrow P_2$. This travelled distance is different from the spatial difference illustrated by the solid double-headed arrow between P_1 and P_2.

molecular travelling distance is obtained by:

$$D_{tr} = Sp_C(t_C - t_{LC}), \tag{4.6}$$

where the quantities to the right in Eqn. (4.6) are molecular attributes implemented to the default molecular dynamics solver. The attribute t_{LC} is the time of the last occurring collision, t_C is the current simulated time and Sp_C is the current speed of the molecule. The attributes Sp_C and t_C are easily accessible to the default solver but in order to make the free path measurement the additional molecular attributes t_{LC} and Col are required in the code. The attribute t_{LC} is statically set to the current simulation time when a collision occurs. The attribute Col is implemented to keep track of whether a molecule is currently undergoing a collision in which case it is activated (set to one), which happens if the molecule is closer to any other molecule than the distance of σ. The attribute Col is deactivated (set to zero) if the molecule is at a distance greater than σ to any other molecule and if it is currently activated.

It should be noted that the present recording of the mean free path does not affect the original way the molecular dynamics solver predicts the dynamics of the gas.

4.4 Set-up of the molecular dynamics simulation

The gas molecules are initially spatially distributed in the domain in a single cubic crystal arrangement and given a random velocity from the Maxwellian velocity distribution [35]:

$$\sqrt{\frac{M}{2\pi RT}}\exp\left(-C^2M/2RT\right), \tag{4.7}$$

in the velocity directions C_x, C_y and C_z of $\boldsymbol{C}$ corresponding to the set gas temperature of 273.15 K and M.

The newly defined molecular dynamics attributes (t_C and Col) used for recording the collision-less travelling distance are set to zero, which is why the results of the mean free path are zero at the start of the simulation as is shown in section 4.5.1.

Filling a cube of edge length l should theoretically require a number of molecules, at STP, given by:

$$N_t = \frac{\rho l^3 N_{Av}}{M}. \tag{4.8}$$

The value for M and ρ are listed in Table 4.1. The number of molecules N_t in the volume l^3 is displayed in Table 4.4, together with the actual number of simulated molecules. It should be noted that the number of molecules in a gas is roughly independent of the type of gas.

Table 4.4: The number of simulated molecules N_s and the theoretically calculated number of molecules, N_t from Eqn (4.8), required to fill the cubes of edge lengths l_A, l_B and l_C, given by Eqn (4.5). Also displayed is the ratio N_t/N_s of molecules. The number of computer processors used for the various simulations and the corresponding real time in hours is shown for the simulation to finish at 3 nanoseconds.

Gas:	Ne			He	Ar
case:	l_A	l_B	l_C	l_B	l_B
size: (l/λ_{Ne}):	0.5	1.0	1.5	1.0	1.0
N_t, theoretical	6293	50345	169914	50197	50412
N_s, simulated	6292	50364	169922	50249	50439
N_t/N_s	1.0002	0.9996	1.0000	0.9990	0.9995
No. processors	1	4	8	4	4
prob. time (hours)[a]	14	19	27	≈ 19	≈ 19

---

[a] The machines used for these simulation were Dual Core AMD Opteron(tm) Processor 270, 2 GHz, 4GB RAM.

The theoretical number of molecules from Eqn (4.8) is better obtained by the larger simulated case size of l_C than the two smaller cases. This is expected because in smaller cube volumes, the number of molecules in the initial crystal lattice is sensitive to the location of where the sides of the lattice lies, which causes the cube volumes to be more difficult to fill to a more precise and accurate amount. For larger cube sizes there is a sufficient number of molecules in the bulk of the lattice to cause a smaller effect of the number of molecules affected at the borders. It should be noted that the theoretical predictions of the mean free paths of Eqn (2.6) and (2.12) for λ is inversely proportional to ρ and therefore also to $n = N_t/l^3$. This means that the divergence from unity of N_t/N_s in Table 4.4 can be directly related to an expected deviation of the simulated mean free path from the theoretical value.

The default time step value of the molecular dynamics simulation is 10^{-14}s, but in this thesis a time step value of 0.5×10^{-14}s is used instead to obtain more precise molecular movements and interactions. An additional reason for not using the default time step value is that this value causes the molecules of the simulation to come closer to each other than what the default molecular minimum closeness parameter allows [3], which causes the simulation to terminate. Using half of the default time step value means that the molecules do not come closer to each other than what the minimum closeness parameter allows.

4.5 Simulation results

In Figure 4.3 the various mean free path measurements using molecular dynamics are schematically illustrated. The unconfined distribution function of the free path is measured for the helium, neon and argon gases. Next the mean free path is measured for neon gas the measurement uses three different volumes of gas packages, under the same STP gas conditions. The three gas volumes are investigated in order to evaluate whether the size of the volume affects the averaged values of the mean free paths. Two sets of measurements of the unconfined mean free paths are made for helium neon and argon. One of the simulation sets is performed considering the affect of all collisions, i.e. whatever number of molecules taking part in a collision, referred to as multiple-part collisions. The other set of measurements concerns the mean free paths recorded only between binary collisions. This corresponds to the theory on which the conventional definitions of the mean free paths in Eqn (2.6) and (2.12) are based. This yields a validation of the dilute gas assumption stated in Eqn (2.5). The effective mean free path is there after measured as a wall is introduced at one side of the cube. The wall is simulated as specular or diffusive or a combination of both in section

---

[3] The default molecular minimum closeness parameter is 1×10^{-10}m for neon and 1.5×10^{-10}m for argon. For helium the minimum molecular closeness parameter was not defined which is why this value was set to be the same as for neon.

4.5.2, and in addition a more realistic explicit wall is investigated consisting of tethered molecules. Also, the mean free path between two planar walls is measured, where the walls are simulated as either specular or diffusive. Finally, the effective mean free path is measured in the near-wall vicinities of non-planar geometries consisting of a spherical obstacle case and a spherical cavity case, which have either a specular or a diffusive surface.

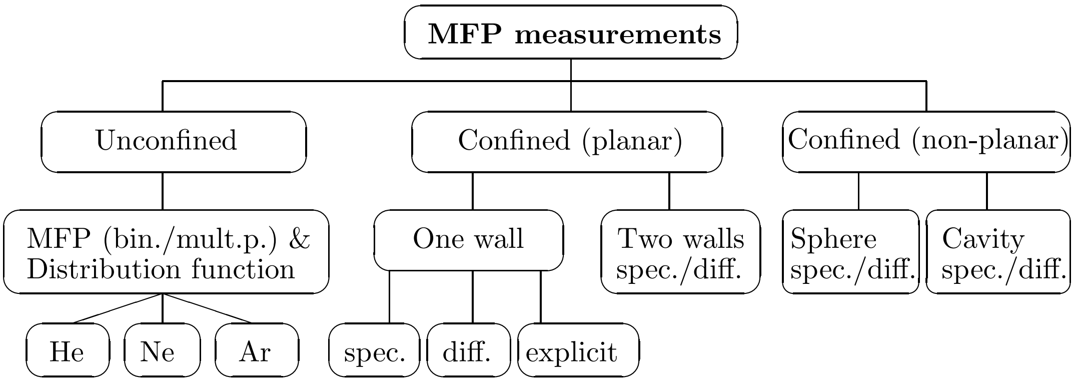

Figure 4.3: Schematic representation of the mean free path measurements using molecular dynamics. The following abbreviations are used, bin. = binary collisions, mult.p. = multiple part collisions, spec. = specular reflections and diff. = diffusive reflections.

4.5.1 Unconfined mean free path

Before the mean free path of the unbounded helium, neon and argon gases are measured, the theoretical free path distribution function of Eqn (3.1) is compared with measurement of the free paths in molecular dynamics. In Figure 4.4 the theoretical free path distribution by Stops [60] and the measured free path distribution are compared. For helium, neon and argon, the longest free paths recorded are 2.4458×10^{-6}m, 1.5804×10^{-6}m and 6.8072×10^{-7}m respectively, out of a sampling of approximately 5 million free paths. The average of these free paths, i.e. the corresponding mean free paths, are 1.6692×10^{-7}m, 1.215×10^{-7}m and 6.0990×10^{-8}m respectively, being 1.58% 1.46% and 0.51% less than the theoretical values of the mean free path for Maxwellian molecules. It is seen that the simulated free path distribution profiles are in close agreement to the theoretical distribution profiles and differ mostly for short free paths where the largest error is for argon being approximately 11% higher for the simulation than for the theoretical free path distribution. The reason for the larger number of simulated short-range free paths might be because the simulation only accounts for collisions to occur point-wise. This is justifiable in the sense that a molecule will always have a non-zero free path except for in the instant it is experiencing the collision. An alternative modelling approach would be to keep the free path of the colliding molecules zero throughout the duration of the collision and re-initiate the free path recording once the molecules are separated by a distance of σ. Although this is expected to have only a small effect on the measured mean free path results because the ratios of σ/λ are 1.2986×10^{-3}, 2.0953×10^{-3} and 5.9729×10^{-3} for helium, neon and argon respectively. The fact that argon has such a large σ/λ ratio would explain why the deviation of the short ranged free paths is largest for this molecule type case.

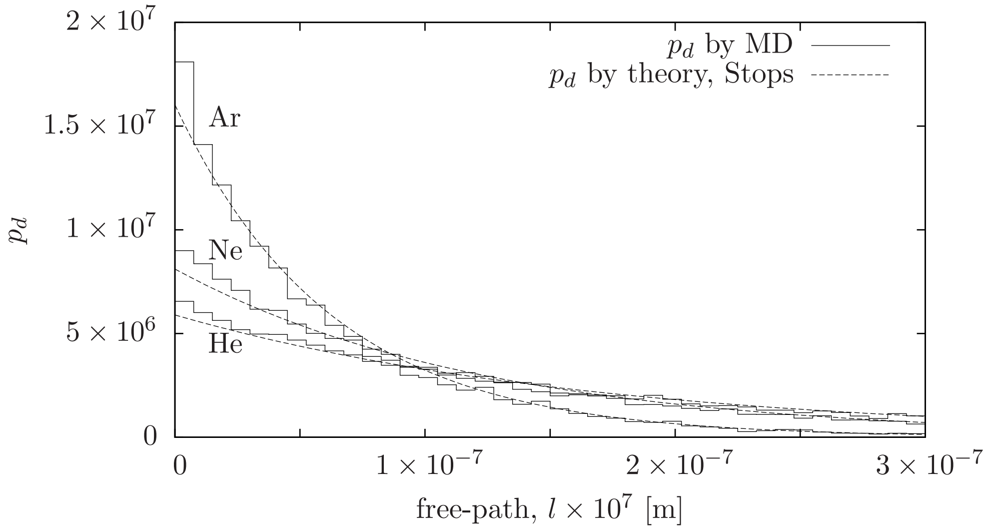

Figure 4.4: MD and theoretical comparison of free path distribution in unconfined helium, neon and argon gases. In the MD simulation the l_B domain size is used, recording about 5 million free paths after a settling problem time of 3 nanoseconds.

As the free path distribution acquired by molecular dynamics is reasonably close to the theoretical free path distribution, it is now of interest to investigate the convergence of the mean free path with respect to the problem time. First, an investigation is performed allowing for multiple molecules taking part in collisions. This is assumed to correspond to the behaviour of a real gas, as opposed to the condition of binary collisions on which the theoretical mean free path formulations are based.

Figure 4.5 shows the recorded mean free paths for the l_A, l_B and l_C cases for neon. By comparing these cases it can be seen that the cases with more molecules have smoother lines of convergence to steady-state. This is because a case with a larger number of molecules will cause the cell averaging to be done over a larger number of free paths in the same unit of time.

Since the convergence values of the mean free path results are seen to be independent of the geometry size in Figure 4.5, measurements are only made with respect to the common geometry domain size of l_B. The results of the $l_B = \lambda_{\mathrm{Ne}}$ case for neon gas, the $l_B = 0.73\lambda_{\mathrm{He}}$ case for helium and the $l_B = 2.01\lambda_{\mathrm{Ar}}$ case for argon are shown in

Figure 4.6. The cases are considered to have stabilised at a constant level after about 1.5 nanoseconds. An average of the l_B results is therefore calculated in the time interwall between 1.5 and 3 nanoseconds. The results of the mean free paths for helium, neon and argon are 1.6720×10^{-7}m, 1.2110×10^{-7}m and 6.1700×10^{-7}m respectively. The error percentages are 1.42% 1.79% 0.65% lower than the corresponding theoretical values for Maxwellian molecules for helium, neon and argon respectively. The reason for the differences in the error percentages between the free path investigation and the mean free path investigation is not known. However, the sampling of approximately 5 million free paths took less than the 1.5 nanoseconds used for the sampling of the mean free path investigation. This shorter sampling time could have caused the average of the free paths to be biased. In order to achieve a better sampling it might therefore be beneficial if the sampling of the 5 million free paths is distributed more sparsely over the longer time range of 1.5 nanoseconds.

It is considered that the l_B case of argon shows best agreement with the theoretical mean free path. This may be because this gas has the shortest mean free path of the gases, and the bounding box is therefore relatively large compared to the other cases. Correspondingly the simulation of helium, having the longest mean free path of the studied gases is the simulation that deviates the most from its theoretically estimated value. Alternatively the difference could depend on the scaling $\epsilon\sigma^2 = \sigma'^2\epsilon'$ which was used to obtain the ϵ values shown in Table 4.2. As the applied σ values seem to yield a correct magnitude of the mean free path value for all the gases the down-scaling of the ϵ values for helium and neon cause a stronger attractive force between the molecules and therefore a shorter mean free path. The ϵ value for the argon gas is slightly scaled down causing the molecules to be less attracted to each other and thereby might cause a relatively longer mean free path. Since the simulated results shown in Figure 4.6 are slightly lower compared to the theoretically derived mean free path values an investigation is made of the mean free path based on binary collisions, which would be expected to predict a longer mean free path due to fewer occurring collisions.

The unbounded mean free path only taking binary-collisions into account is recorded by neglecting a molecule's collision in cases where more than two molecules are taking part. In the simulation this is performed by not recording a collision if a molecule is within the collision distance of another molecule with the Col parameter set to one. In this investigation only the l_B cases for helium, neon and argon are simulated. The results are again compared with the theoretical mean free path values. This yields average values of 1.6684×10^{-7}m, 1.2139×10^{-7}m and 6.1875×10^{-8}m for helium, neon and argon respectively, from the sampling time range in between 1.5 and 3 nanoseconds. It should be noted that in the comparison of the mean free paths between the simulations using multiple part collisions and the simulations using binary collisions that it is for

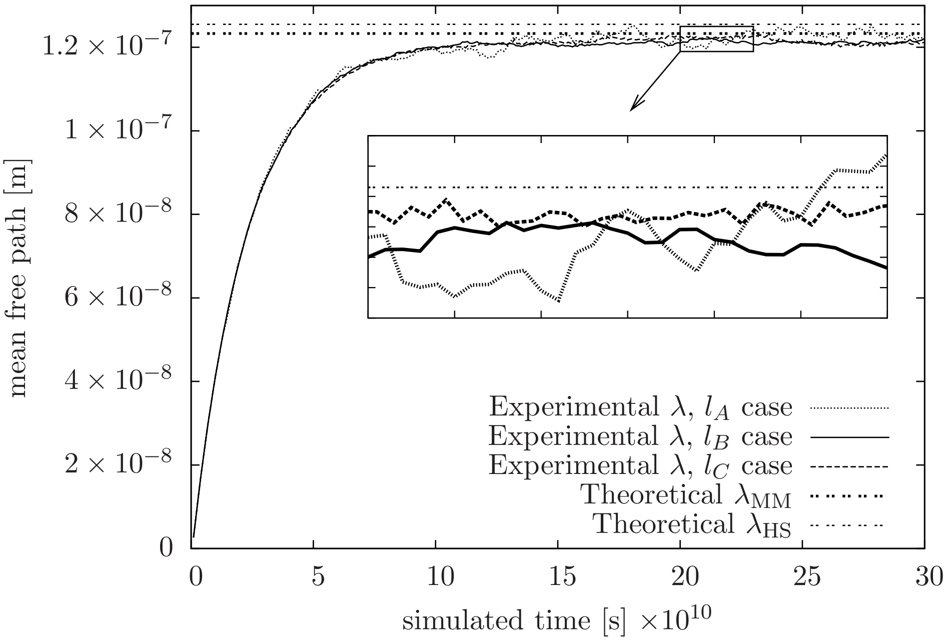

Figure 4.5: Convergence to steady value of the $l_A = 0.5\lambda_{\mathrm{Ne}}$, $l_B = \lambda_{\mathrm{Ne}}$ and $l_C = 1.5\lambda_{\mathrm{Ne}}$ cases for neon gas, when multiple part collisions are taken into account, plotted against problem time. The conventional values of the mean free paths assuming Maxwell molecules and hard-spheres are illustrated by the constant dashed lines at the values listed in Table 4.1.

argon gas simulations that the mean free path is proportionally the largest for the simulation involving binary collisions compared to the simulation involving multiple part collisions. This is reasonable since multiple part collisions are also occuring more often for argon due to the molecules larger diameter, which shortens the mean free path more severely.

The mean free path results of the simulation involving binary collisions are considered to be close enough to the corresponding results involving multiple part collisions, making it reasonable to conclude that the dilute gas approximation of Eqn (2.5) is seemingly fulfilled. However, this conclusion might not be valid for investigations of other parameters than the mean free path. The number of multiple-part molecular collisions and binary collisions in the simulations of helium, neon and argon are listed in Table 4.5 together with the ratio of the two. The number of multiple-part collisions is considerable in comparison to the binary collisions for all the studied gases. The reason for the mean free paths for helium, neon and argon not being very different for the cases where binary collisions are considered compared to the results where multiple part collisions are considered is not certain. However, it could be argued that the modelling of molecules experiencing binary collisions often causes a termination of the free path of an extra "external" incoming molecule anyway. This is assumed to frequently

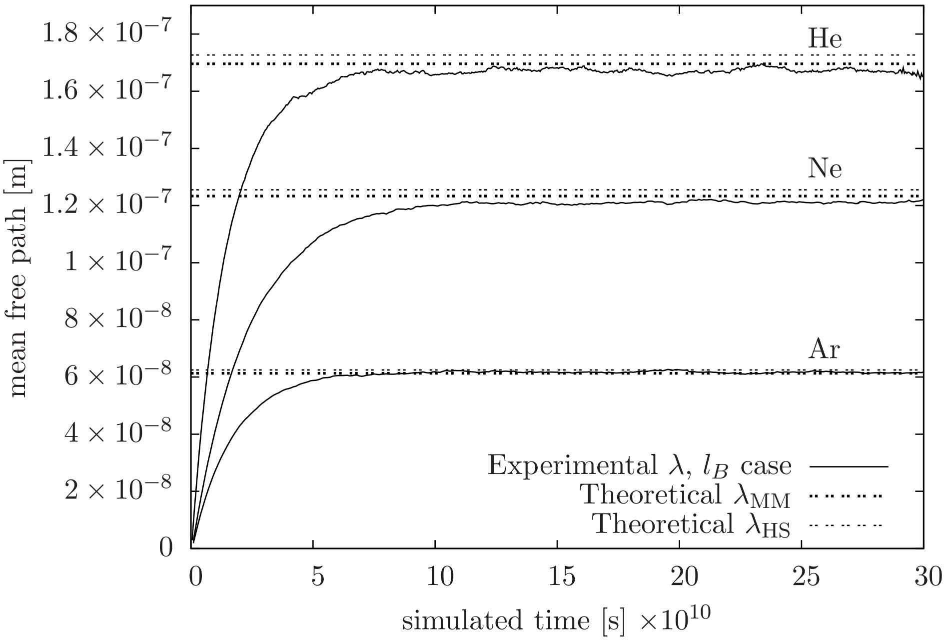

Figure 4.6: Convergence to steady value of the $l_B = \lambda_{\text{Ne}}$ case for neon gas, the $l_B = 0.73\lambda_{\text{He}}$ case for helium and the $l_B = 2.01\lambda_{\text{Ar}}$ case for argon when multiple part collisions are taken into account, plotted against problem time. The conventional values of the mean free paths assuming Maxwell molecules and hard-spheres are illustrated by the constant dashed lines at the values listed in Table 4.1.

Table 4.5: The number of binary collisions and multiple-part collisions and the ratio of the multiple-part collisions for the gases helium, neon and argon. The sampling time range is between 1.5 and 3 nanoseconds of the problem time.

Gas:	He	Ne	Ar
multiple-part collisions	47022	29897	71030
binary collisions	251836	203410	212773
ratio	0.8427	0.8719	0.7497

occur as the external molecule experiences a collision with one of the initially colliding molecules as soon as the latter two are separated by a distance greater than σ.

The reason for the difference between the measured mean free path values and the theoretical values could be due to the assertion of the selected Lennard-Jones parameters. Also it would be of particular interest to investigate the influence of applying non-unity values to the collision integral for viscosity used in determining σ.

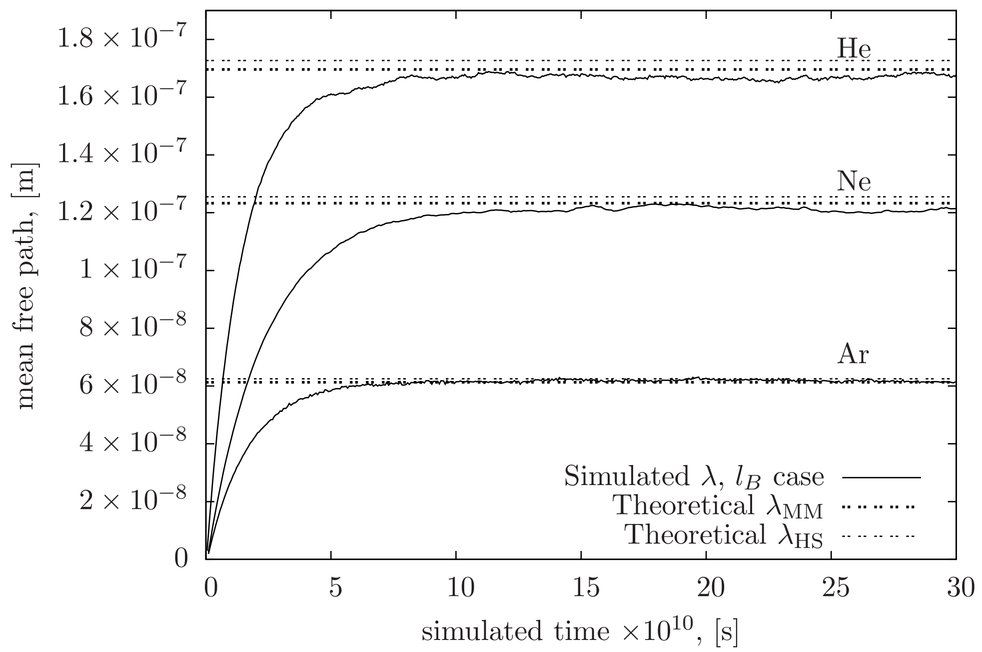

Figure 4.7: Convergence to steady value of the l_B cases for helium, neon and argon gases when only binary molecular collisions are taken into account, plotted against problem time. The conventional values of the mean free paths assuming Maxwell molecules and hard-spheres are illustrated by the constant dashed lines at the fixed values listed in Table 4.1.

4.5.2 Confined mean free path

Here the surface effects on the mean free path of neon are investigated in order to show whether gas molecular collisions with solid walls yield similar shortenings of the mean free path as predicted by the new theoretical model in chapter 3. These simulations are performed in a box shaped domain. The simulated geometry has side lengths of $0.75\lambda_{\mathrm{Ne}}$ in the x- and z-directions and $2\lambda_{\mathrm{Ne}}$ in the n-direction. The domain uses two pairs of periodic boundaries, in the **x**- and **z**-directions (Figure 4.8) and, with reference to the wall normal coordinate, **n**, two parallel planar reflective surfaces are placed at $\mathrm{n} = 0$ and $\mathrm{n} = H$. The reflective surfaces are first chosen to be specular, i.e. the molecular tangential velocity is maintained and the molecular normal velocity just changes sign when a molecule is reflected. By using reflective surfaces an investigation of the mean free path profile affected by both a single planar wall and two planar walls is performed.

The length of the molecular free paths since the molecules last experienced collision is again determined using Eqn (4.6). The reflective surfaces are used in two different ways. Firstly, and more intuitively, one of them is used to act as an actual wall by setting $t_{LC} = t_C$, similar to how inter-gas molecular collisions are calculated. Secondly a reflective surface is used to simulate the effects of the bulk flow. This is done by

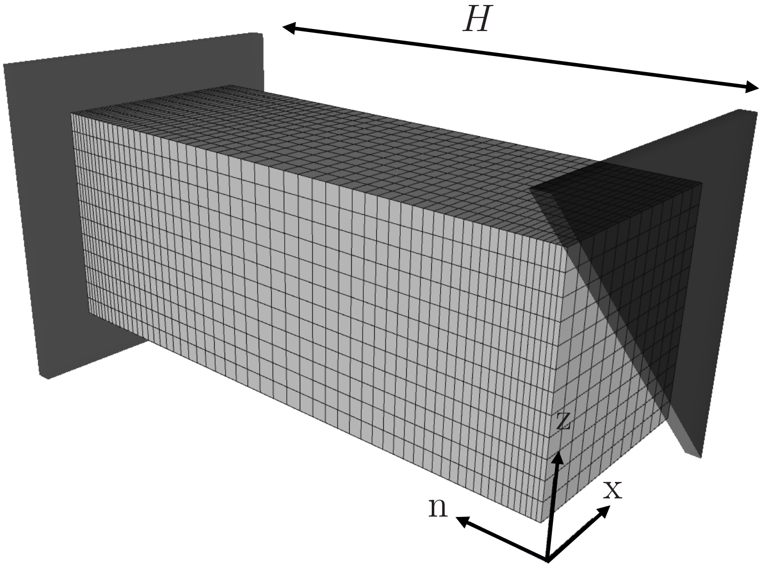

Figure 4.8: An example of the simulated molecular dynamics geometry, extending between two reflective surfaces at n $= 0$ and n $= H$. The width and breadth of the geometry is $0.75\lambda_{\mathrm{Ne}}$. Periodic boundary conditions are applied in the x- and z-directions. The mesh shown consists of $12 \times 12 \times 60$ cells in the x-, z- and n-directions respectively. For the two-planar-wall case, shown here, the cells are graded in the n -direction so that the cell widths at n $= 0$ and at n $= H$ are one quarter of the cell widths at n $= H/2$.

setting all reflected molecules to have experienced a collision-less travel of one mean free path which is done by setting $t_{LC} = \lambda_{\mathrm{Ne}}/Sp_C - t_C$, where λ_{Ne} is the conventional mean free path for neon gas unaffected by solid boundaries.

There after an investigation is performed where one of the walls is chosen to be diffusive, emitting reflected molecules with a Maxwellian velocity distribution. Finally a molecular dynamics simulation is performed where the wall is modelled explicitly and made up of actual neon molecules that are tethered to a fixed lattice, with a density of 1000kg/m^3. For simplicity, the wall molecules are simulated as molecules without any intermolecular interaction between themselves. They are tethered with a very stiff spring constant to prevent movement into the sampling region of interest. A sampling of reflected molecular speeds from the diffusive and explicit walls is presented in Figure 4.9, alongside the Maxwellian speed distribution. The molecular dynamics results of diffusely reflected speeds consists of 141 522 samples presented as a histogram with a bin-width of 10m/s. The sampling of the molecular speeds using explicit walls is made using two different thickness's of the walls. The thinner explicit wall case is not labelled with a subscript and uses 135 776 molecules in total out of which 79 288 are wall molecules in a wall of width 0.0025λ. The thicker explicit wall case is labelled thick as a subscript and uses 150 016 molecules in total out of which 94 328 are wall molecules in a wall of width 0.003λ. The speed of the molecules are recorded at a distance of 5×10^{-10}m away in the normal direction from the wall consisting of tethered molecules so the wall's potential influence on the gas molecules should be reduced compared to the wall potential affect on the molecules at the wall. This sampling consists of 54 565 and 88 898 reflected molecules for the thinner and for the thicker explicit wall cases respectively and is presented in Figure 4.9. The distribution of the reflected molecular speeds is presented using bin-widths of 10m/s for the diffusive wall and 20m/s for the explicit walls.

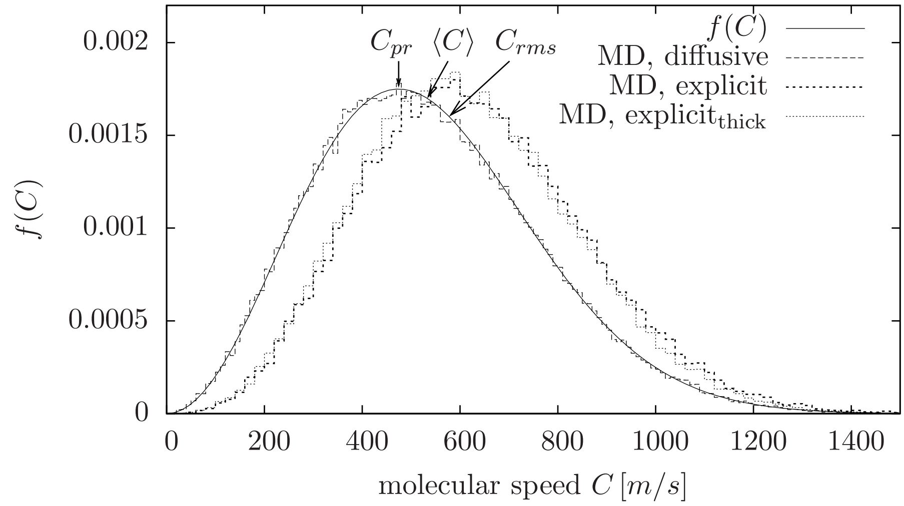

Figure 4.9: Maxwell's molecular speed distribution $f(C)$ from Eqn (2.17) together with the most probable speed, C_{pr}, the mean molecular speed, $\langle C \rangle$, and the root-mean-square speed, C_{rms}.

It is seen in Figure 4.9 that the simulation manages to reflect molecules diffusely with the Maxwellian speed distribution well. However, the molecular speed distribution obtained from molecules that are reflected off explicit walls is shifted to a higher speed compared to the case of diffusely reflected molecules. The molecular speeds where recorded at a wall distance of 5×10^{-10}m for which the wall potential was assumed to be negligible, which seem reasonable by inspection of Figure 4.1. However, the superimposed potential from all the wall molecules probably causes the gas molecule to be in a region of considerable influence of the wall potential. The recorded speeds of these reflected molecules should therefore probably be made at an even larger wall distance. The deviation of the effective mean free path profile is not assumed to depend on the molecular speeds of the reflected molecules since the measured speed distribution has the same shape as the Maxwellian. It is assumed that the speed distribution for explicit walls should be shifted to the same location as the Maxwellian in case the molecular speeds are recorded at an appropriate distance from the wall. It is also seen in Figure 4.9 that there is no visual difference between the molecular speed distributions between the thinner and thicker explicit wall cases.

Results of mean free path affected by one wall

The results of the mean free path affected by one planar wall are here presented for neon gas. The geometry is similar to the geometry illustrated in Figure 4.8 having the same side lengths of $0.75\lambda_{\mathrm{Ne}}$ in the x- and z-directions and $2\lambda_{\mathrm{Ne}}$ in the n-direction. The grading of the mesh is configured so that the near-wall cell widths at $\mathrm{n} = 0$ are one quarter of the width of the largest cells located at $\mathrm{n} = H$. This configuration uses 12 cells in the x- and z- directions and 40 cells in the n-direction. Since slightly different grids have been tested and there has not been any observed dependence of using different grid structures, the grid is purely chosen in order to yield good detail in near-wall regions where the mean free path tends to change more than in the bulk-ward cells. The gas is simulated by 56 672 molecules for implicit walls and by 56 488 and 55 688 gas molecules for explicit walls of the thinner and thicker walls respectively. The number of simulated molecules should be compared to the theoretical estimate of the number of molecules in this volume of gas:

$$N_t = \frac{\rho\,(0.75 \times \lambda_{\mathrm{Ne}})^2\,(2 \times \lambda_{\mathrm{Ne}})\,N_{Av}}{M}, \tag{4.9}$$

which yields a value of 56 638. This value is assumed to be sufficiently close to the simulated number of molecules in order for the results not to biased. The sampling of the effective mean free path profile, in terms of the problem time, is made over 2 nanoseconds taken after 4 nano seconds settlement.

The simulation result of the mean free path profiles are compared to the new theoretical model of $\lambda_{\mathrm{eff}} = \lambda J$, where J is given by the one wall case of Eqn (3.7), i.e.

$$\begin{aligned}\frac{\lambda_{\mathrm{eff}}}{\lambda_{\mathrm{Ne}}} =& 1 - \frac{1}{82}\left[\exp\left(-\frac{\mathrm{n}}{\lambda_{\mathrm{Ne}}}\right) + 4\sum_{i=1}^{7}\exp\left(-\frac{\mathrm{n}}{\cos\left(\,(2\,i-1)\,\pi/28\right)\lambda_{\mathrm{Ne}}}\right)\right.\\ &\left. +2\sum_{i=1}^{6}\exp\left(-\frac{\mathrm{n}}{\cos\left(\pi/14\,\right)\lambda_{\mathrm{Ne}}}\right)\right],\end{aligned} \tag{4.10}$$

where n is the wall-normal distance in accordance to Figure 4.8. The results are also compared with the corresponding model by Stops [60] expressed in Eqn (3.2) i.e.

$$\frac{\lambda_{\mathrm{eff}(S)}}{\lambda_{\mathrm{Ne}}} = \frac{1}{2}\left[2 + \left(\frac{\mathrm{n}}{\lambda_{\mathrm{Ne}}} - 1\right)\exp\left(-\frac{\mathrm{n}}{\lambda_{\mathrm{Ne}}}\right) - \left(\frac{\mathrm{n}}{\lambda_{\mathrm{Ne}}}\right)^2 Ei\left(\frac{\mathrm{n}}{\lambda_{\mathrm{Ne}}}\right)\right], \tag{4.11}$$

for a one-wall case. A two-term exponential Gauss–Newton curve-fit is applied to the molecular dynamics results (except for the thicker explicit wall case) for which the general form is:

$$\frac{\lambda_{\text{eff}(CF)}}{\lambda_{\text{Ne}}} = 1 - \frac{1}{2}\left[A_1 \exp\left(\frac{-A_2\text{n}}{\lambda_{\text{Ne}}}\right) + A_3 \exp\left(\frac{-A_4\text{n}}{\lambda_{\text{Ne}}}\right)\right], \tag{4.12}$$

which has the parameters listed in Table 4.6.

Table 4.6: Curve-fit data parameters. The explicit wall data is for the thinner wall case.

reflection	A_1	A_2	A_3	A_4
specular	0.466763	5.38570	0.53324	0.96319
diffusive	0.45487	23.48058	0.99366	2.22688
$\sigma_{\boldsymbol{v}} = 0.8$	0.45735	20.69306	0.93510	2.03169
explicit wall	1.43102	0.71099	0.00540	20.9878

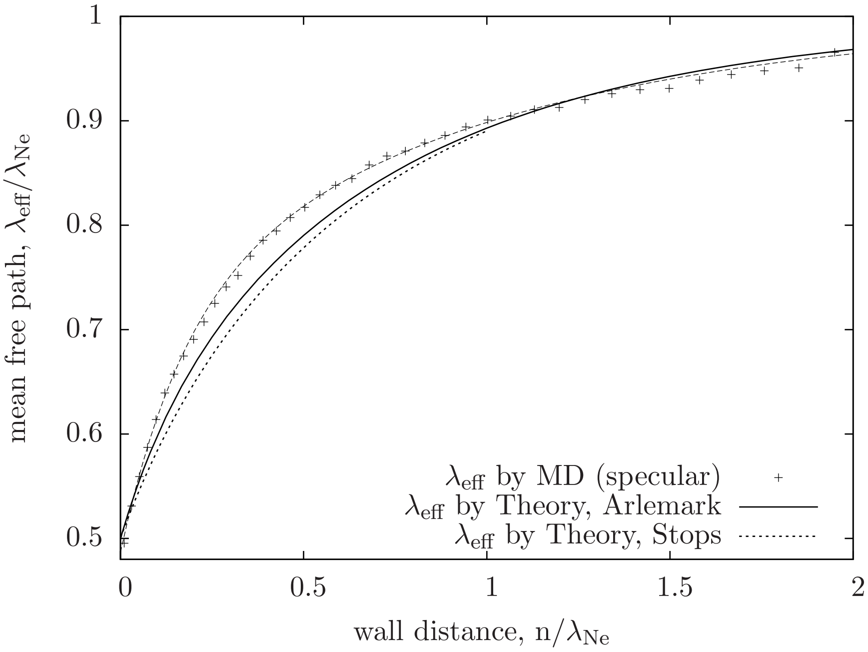

Figure 4.10: Comparison between effective mean free path profiles by molecular dynamics using a specular wall and by theoretical models from physical reasoning.

It can be seen in Figure 4.10 that the theoretical λ_{eff} models achieve the same near-wall values and bulk values as the molecular dynamics simulation for the specular wall case. However, the λ_{eff} results from the simulation is slightly higher than the theoretical results at approximately $\text{n} = 0.5/\lambda_{\text{Ne}}$. It can be seen in Figure 4.11 that the λ_{eff} profile for a diffusive wall achieves a near-wall value of about 0.3λ, which is lower than for

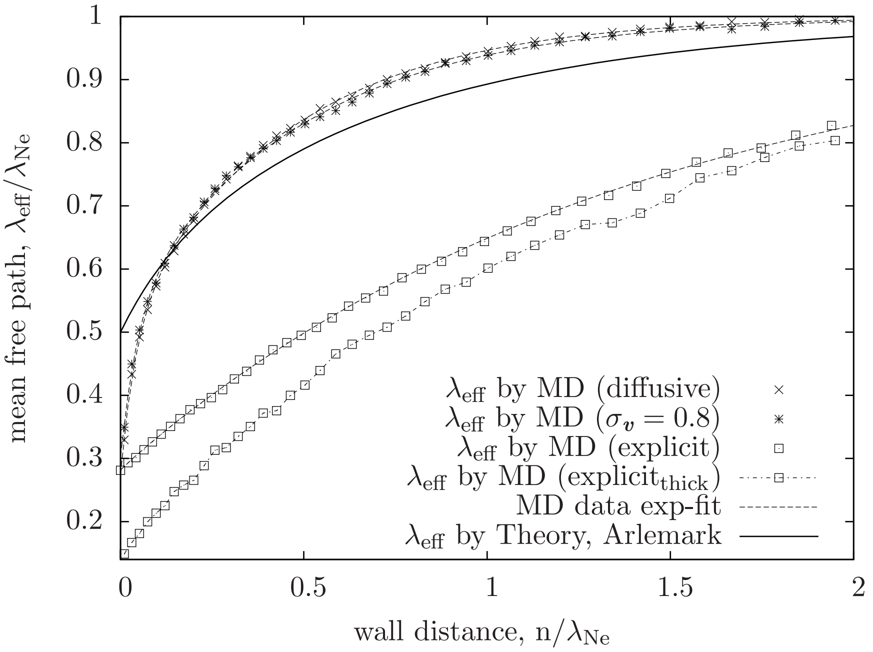

Figure 4.11: Comparison between effective mean free path profiles by molecular dynamics using a diffusive wall, a wall with $\sigma_{\boldsymbol{v}} = 0.8$ and two widths of explicit walls and by the new theoretical model from physical reasoning.

the cases with specular walls (which have a near-wall value of 0.5λ). The λ_{eff} profile using a diffusive wall achieves values close to λ at approximately $\mathrm{n}/\lambda_{\mathrm{Ne}} = 1$, which should be compared to the case using specular reflections achieving similar values at approximately $\mathrm{n}/\lambda_{\mathrm{Ne}} = 1.6$.

It is interesting to compare these results with the results using explicit walls as also shown in Figure 4.11 which clearly show a much lower λ_{eff} profile, with near-wall values of about 0.28λ and 0.14λ for the thinner and thicker explicit walls respectively. The λ_{eff} profiles of these cases also have much more constant gradient of increase in the n-direction and much flatter profiles than the corresponding profiles for the implicit walls. The mean free path profile by the thinner and thicker explicit wall cases achieves values of about 0.83λ and 0.80λ respectively at $\mathrm{n}/\lambda_{\mathrm{Ne}} = 2$.

Since there is a significant difference between the two λ_{eff} profiles for the two explicit wall cases it is assumed that the thicker wall has a more realistic wall influence on the gas molecules considering that the walls are just a few molecular layers thick. However, due to that explicit walls are costly to simulate it was chosen here not to perform an investigation with even thicker walls. Figure 4.9 shows that the molecules are on average reflected off both the thinner and the thicker explicit walls at a higher speed than for specular and diffusive walls, which makes the result of the explicit walls counter-intuitive considering the lower mean free path profile and the fact that faster molecules are less likely to experience collisions compared to slow molecules, as discussed in section 2.2.2 for the variable-hard-sphere molecular representation. Due to these aspects other wall models than the explicit walls might be needed. Quite different results may be obtained in case wall molecules are modelled having different σ and ϵ values than for the presently used ones gas molecules. The wall molecules were chosen here to be modelled using the same type of molecules as the gas (but at a density of 1000 kg/m^3). The values for σ and ϵ could be chosen to correspond to molecules of more normal substrate material of micro-gas-flow channels such as silicon which is often used in MEMS. Examples of an other wall model is the Weeks–Chandler–Andersen wall potential which cuts off the attractive long-range force from the Lennard-Jones potential of the wall molecules (Markvoort *et al.* [40]). This might cause the speeds of the wall reflected molecules to have a more similar speed distribution compared to the Maxwellian distribution at the chosen wall distance of 5×10^{-10}m. An other wall modelling technique is presented by Spijker *et al.* [58] where averaged contributions of explicit walls are used to obtain a boundary condition yielding reasonable macroscopic gas quantities such as temperature, pressure and heat flux. By using this technique a wall potential could be simulated implicitly based on averaged data from an explicit wall yielding that the computational process would be more efficient.

Results of mean free path affected by two walls

In this section the reflective surface at $\mathrm{n} = H$ is modelled as a specular wall similar to the wall at $\mathrm{n} = 0$ in the previous section, instead of representing the bulk. The simulated geometry has side lengths in the **x**- and **z**-directions of $0.75\lambda_{\mathrm{Ne}}$ and in the **n**-direction five different side lengths are studied, which in terms of H/λ_{Ne} are 5, 2, 1, 0.5 and 0.05 units corresponding to Kn of 0.2, 0.5, 1, 2, 20 respectively.

These simulation results are presented together with the new theoretical model for a gas in a two-wall confinement represented by $\lambda_{\mathrm{eff}} = \lambda J$, where J is given by Eqn (3.7).

An additional comparison is made with Stops [60] effective mean free path model modified to consider two walls as suggested by Guo [22], i.e. Eqn (3.2). The molecular dynamics curve-fit to the data for the one-wall case presented by Eqn (4.12), is reformulated in an attempt to predict the λ_{eff} profile for two walls as follows:

$$\begin{aligned}\frac{\lambda_{\mathrm{eff}(CF)}}{\lambda_{\mathrm{Ne}}} = 1 - \frac{1}{2}\Bigg[&A_1 \exp\left(\frac{-A_2\mathrm{n}}{\lambda_{\mathrm{Ne}}}\right) + A_3 \exp\left(\frac{-A_4\mathrm{n}}{\lambda_{\mathrm{Ne}}}\right) \\ &+A_1 \exp\left(\frac{-A_2(H-\mathrm{n})}{\lambda_{\mathrm{Ne}}}\right) + A_3 \exp\left(\frac{-A_4(H-\mathrm{n})}{\lambda_{\mathrm{Ne}}}\right)\Bigg], \qquad (4.13)\end{aligned}$$

using the values A_1, A_2, A_3 and A_4 in Table 4.6 for specular reflections. This heuristic model is referred to as the empirical model in this thesis.

The results of the measured effective mean free path profiles for two specular walls is shown in Figure 4.12 together with both the new and Stops' theoretical models and the empirical model by Eqn (4.13). The cases are shown for $Kn = 0.2$, 0.5, 1.0, 2.0, 2.0 (dependent on the lengths of the cases extending in the **n**-direction). It is seen that in general the empirical model gives the best description of the molecular data for all Kn cases. The four different effective mean free path representations all show similar results in the near-wall regions, except for the $Kn = 2$ case. However, the bulk values differ more significantly. For the $Kn = 0.5$ case the empirical model matches the simulated data adequately in the near-wall region but towards the bulk it matches the theoretical models better. The difference between the theoretical and simulated effective mean free path models is greatest for the $Kn = 2$ case, where the empirical model represents the simulated values the best in the bulk but the theoretical models are better in the near-wall region.

The difficulty of reproducing an effective mean free path profile similar to the molecular dynamics data might reflect the difficulty of modelling fluid behaviour in the transition regime. The biggest discrepancy for the mean free path profile is for the $Kn = 2$ case, which is roughly in the middle of the transition regime.

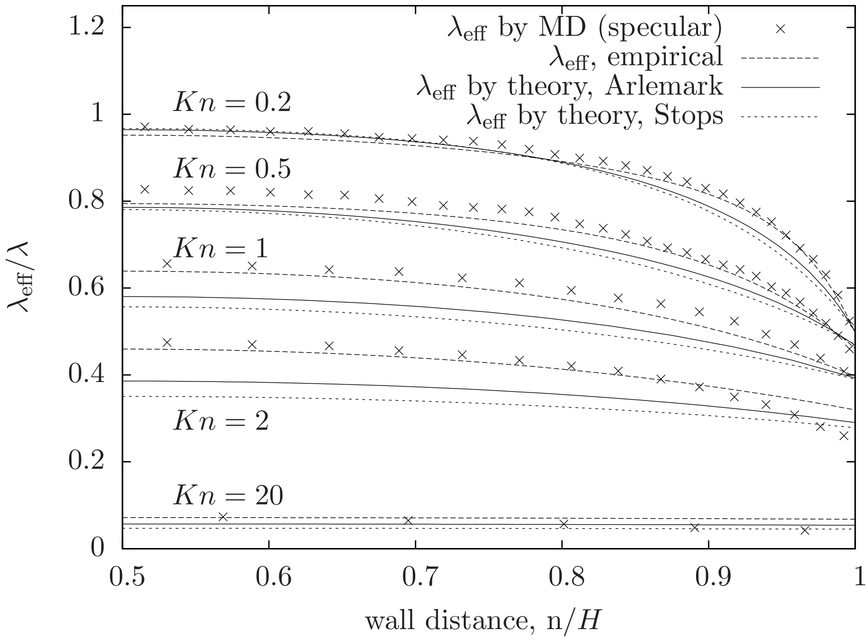

Figure 4.12: Cross-channel effective mean free path profiles affected by two specular walls achieved by molecular dynamics, theoretical models and empirical model from the one-wall molecular dynamics results.

The results of the mean free path profiles for two diffusive walls are shown in Figure 4.13. It is possible to recognise the general trend from the one-wall results previously presented. All the Kn cases show lower near-wall values than for the specular reflection cases. Also the profiles have a sharper gradient leading to higher mean free path bulk values.

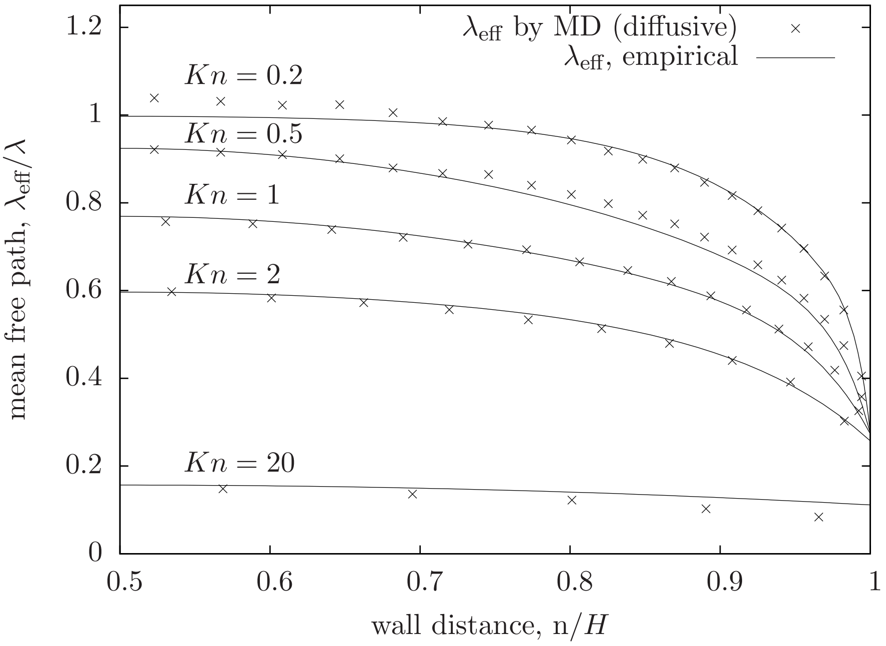

Figure 4.13: Cross-channel effective mean free path profiles for two diffusive walls achieved by molecular dynamics using diffusive walls, theoretical models and empirical model from the one-wall molecular dynamics results.

It is not possible to use an empirical model based on the data for one diffusive wall to model a two wall effective mean free path in the same manner as for an empirical model based on data from specular reflections. This is due to that the curve-fit parameters cause a negative values in the near-wall regions through the term $1-(A1+A3)$ in Eqn (4.12). Instead a different averaging could be used between λ^-_{eff} and λ^+_{eff}. For example, the generalised power mean:

$$\lambda_{\text{eff}} = 1 - \frac{1}{2}\left((1-\lambda^-_{\text{eff}})^s + (1-\lambda^+_{\text{eff}})^s\right)^{1/s} \tag{4.14}$$

could be applied, where s is a modelling parameter. Here $(1-\lambda^-_{\text{eff}})$ and $(1-\lambda^+_{\text{eff}})$ are the collision probabilities for the molecule travelling towards either of the two walls. This expression favours the influence of whichever of λ^-_{eff} or λ^+_{eff} is the closest to the wall. The generalised power mean has been applied to the molecular dynamics data in Figure 4.13 using the diffusive curve-fit parameters from Table 4.6. The modelling parameter s is set to 2, by trial and error. It is seen that the curve-fit model manages to reproduce the effective mean free path results of the $Kn = 2$, $Kn = 1$, $Kn = 0.5$ and $Kn = 0.2$ cases as well.

In order to obtain a model for diffusive reflections which can be applied to the solution method of the Navier–Stokes equations the effective mean free path is also measured for molecules travelling only in the wall-normal direction. In Figure 4.14 these results are shown using specular and diffusive walls. Also shown is the λ_{eff} profile from the curve-fit function:

$$\frac{\lambda_{\text{eff}}}{\lambda} = 1 - \left[A_1 \exp\left(\frac{-A_2 \text{n}}{\lambda_{\text{Ne}}}\right) + A_3 \exp\left(\frac{-A_4 \text{n}}{\lambda_{\text{Ne}}}\right)\right], \tag{4.15}$$

using the coefficients $A_1 = 0.30318$, $A_2 = 9.38115$, $A_3 = 0.69682$ and $A_4 = 1.11005$, for the diffusive wall and the coefficients shown in Table 4.6 for the specular wall. It is seen in Figure 4.14 that the specular and diffusive wall cases yield much more similar λ_{eff} profiles than for the cases where the free paths of the molecules were averaged for molecules travelling in any direction. The largest difference between the two profiles is at about $\lambda_{\text{eff}} = 0.75\lambda$ where the profile of the specular wall case is about 5% larger than the profile for the diffusive wall case.

It should be noted that Stops' [60] derivation of λ_{eff} is based on the collision probability of a molecule only travelling in a direction to wards a planar wall similar to this latter λ_{eff} measurement.

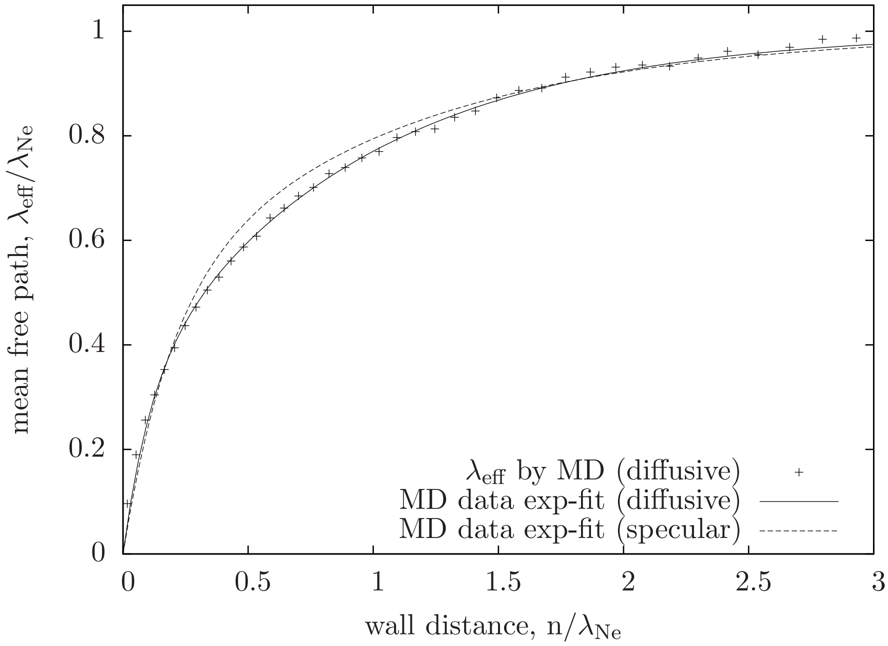

Figure 4.14: One-wall effective mean free path profiles by molecular dynamics and molecular dynamic curve-fit, considering an average of molecules travelling only in the wall-normal direction

Results of mean free path around a spherical obstacle

The variation of the mean free path of neon gas, at standard temperature and pressure, around a spherical obstacle is also studied using molecular dynamics. The unstructured simulated mesh domain is shown in Figure 4.15, for a solid sphere of diameter $d_{sp} = 0.2\lambda_{\mathrm{Ne}}$, consistent with the corresponding theoretical case presented in section 3.2.2. The spherical obstacle is placed inside a cubic domain of side length $l = \lambda_{\mathrm{Ne}}$, with a numerical mesh of $24 \times 24 \times 24$ cells, which is quite coarse [4]. Ideally the sphere should be placed in a gas domain which is as large as possible, but since it is costly to simulate a large numbers of molecules it is here chosen to restrict the domain to this size. The sphere is modelled as both fully specular and fully diffusive in two different investigations. The molecules reflected from the sphere's surface acquire a termination of their free paths, which are accounted for in the simulation by setting $t_{LC} = t_C$. The boundaries of the cube are modelled as fully specular reflective surfaces. These reflecting surfaces are used here instead of periodic boundary conditions, as was used for the measurement of the unbounded mean free path. The reason for using the specular surfaces is that the periodic boundary conditions would mirror the effects of a sphere being located in the centres of fictitious neighbouring cells in an infinite pattern. Since it is desired to model a bulk gas of infinite extension in the surrounding of the spherical obstacle the specular reflective surfaces with the ability to set all reflected molecules' free paths equal to the mean free path where considered to be the best boundary condition available. The molecules reflected of the specular reflective surfaces have their free paths set to the unconfined value by setting their time of the last collision: $t_{LC} = \lambda_{\mathrm{Ne}}/Sp_C - t_C$.

Simulation results are compared to the corresponding theoretical results presented in section 3.2.2. The mean free path values of the cells, in the domain surrounding the sphere, are averaged within 15 spherical sampling bins. The thickness of the bins are graded with an expansion ratio which makes the bin furthest away from the sphere three times the width of the closest one. Within every bin the cell values of both the cells distances from the sphere and the mean free path values are averaged. The results are presented in Figure 4.16.

In Figure 4.16 it is seen that the mean free path profiles from the simulation are quite similar to each other independent of whether the sphere's surface is modelled as specular or diffusive, with the mean free path values for the specular sphere slightly higher at a distance of $r_d/\lambda \approx 0.15$. The molecular dynamics results compare well with the theoretical mean free path profile in the near-wall area. At a distance of about $0.2r_d/\lambda$ the two measured profiles are about 5% lower than the theoretical values. This difference remains at the end of the measuring domain at $0.5r_d/\lambda$.

---

[4] Attempts were made using finer meshes in the close vicinity of the sphere resulting in a smoother sphere surface. However the use of these meshes caused tracking errors of the molecules near the surface, which are explained by Macpherson and Reese [36].

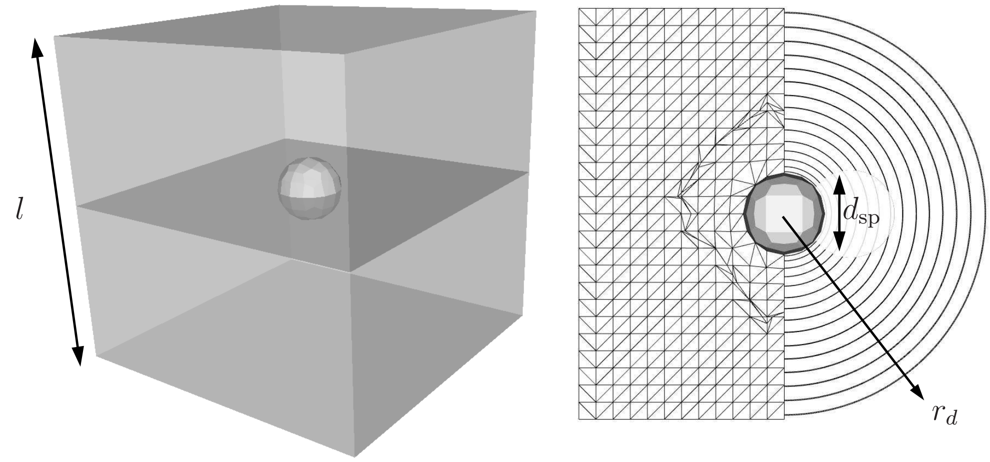

Figure 4.15: A domain containing a spherical obstacle, simulated in molecular dynamics. Left: the cubic bounding domain with the spherical obstacle centre, the cutting plane is more clearly illustrated in the right-hand figure. Right: cutting plane seen from above, illustrating the grid-lines in the left half of the plane and the spherical sampling bins in the right half of the plane.

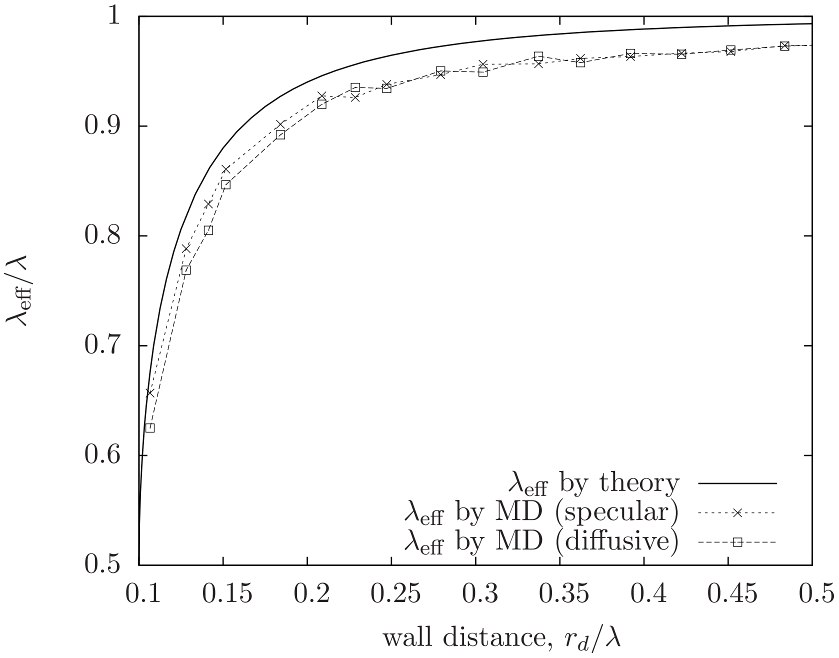

Figure 4.16: mean free path profile in the vicinity of a spherical obstacle achieved by molecular dynamics, compared with the present theoretical model.

Results of mean free path in a spherical cavity

The mean free path inside a spherical cavity is now investigated for a cavity having either a fully specular or a fully diffusive surface. In this case a background mesh of $16 \times 16 \times 16$ cells is used out of which the unstructured mesh of the cavity is created. The spherical cavity domain is represented in Figure 4.17. The free paths of the molecules reflected off the spherical cavity's surface are terminated by setting the time of last collision to $t_{LC} = t_C$. Since there is no bulk to be artificially modelled no other manipulation of this attribute is needed.

In addition to measuring the effective mean free path the average radial distance from any point of the domain to the surface, $\langle D_{tr} \rangle / d_{\text{cav}}$, is also measured by modelling the gas without any intermolecular interactions and by only recording terminations of the molecular free paths due to wall collisions.

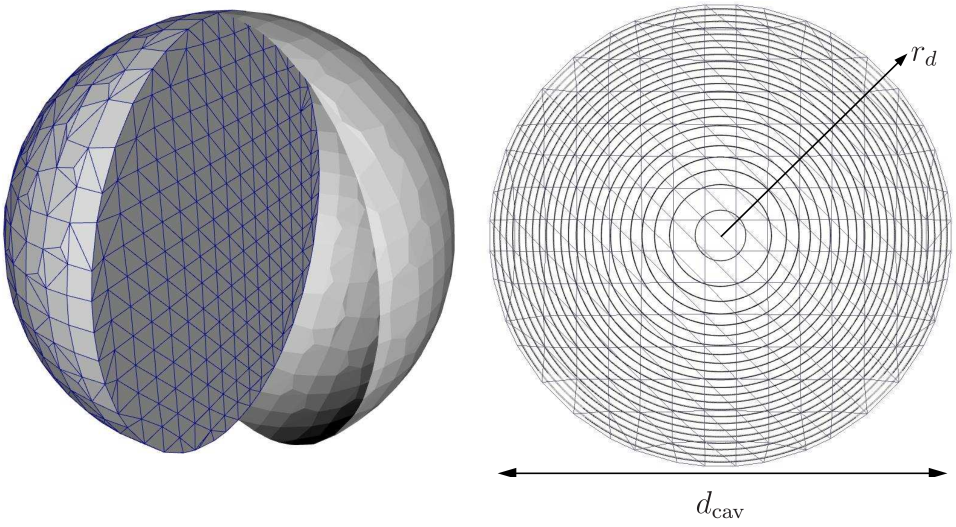

Figure 4.17: A spherical cavity domain simulated by molecular dynamics. Left: the cavity open by a wedge-shaped cut revealing the internal mesh. Right: a cross-sectional plane showing 22 spherical sampling bins of exponentially decreasing width for increasing radial distance as well as the grid used.

In Figure 4.18 results are presented of the measured average wall distance and the mean free path measurements inside the spherical cavity with specular surface. The mean free path is measured using the three different cavity diameters of $d_{\text{cav}} = 0.5\lambda$, $d_{\text{cav}} = \lambda$ and $d_{\text{cav}} = 1.5\lambda$ corresponding to Kn of 2, 1 and 2/3 respectively, where the diameter is used as the characteristic length scale. It is seen that the average distance is correctly achieved in the middle of the cavity but is about 6% too low in the near-wall region. The mean free path results all show similar profiles compared to the corresponding theoretical ones. In the middle of the cavity, ranging from about $\langle D_{tr} \rangle / d_{\text{cav}} = 0.5$ to about $\langle D_{tr} \rangle / d_{\text{cav}} = 0.3$, the mean free path profiles from molecular dynamics show good agreements with the theoretical model, while at the near-wall regions of these cases the molecular dynamics results have about 5% lower values compared to the theoretical results.

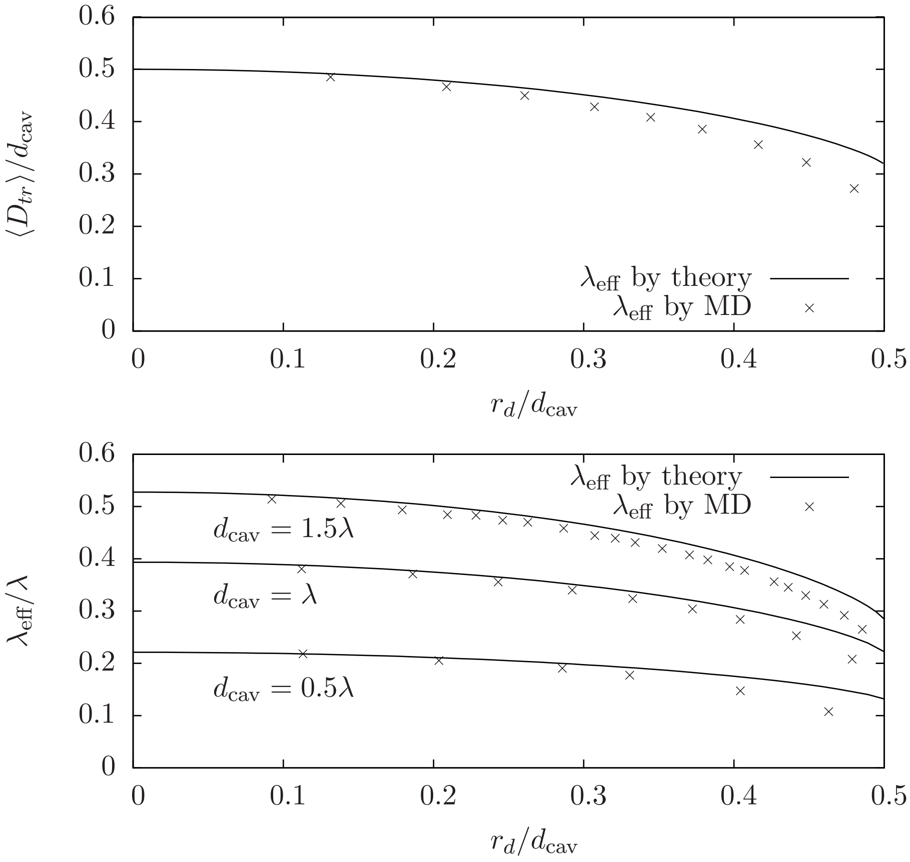

Figure 4.18: Top: average wall distance measured by simulation and corresponding profile from theory. Bottom: mean free path profiles obtained by molecular dynamics and by theoretical model from physical reasoning. The cases shown are $d_{\text{cav}} = 0.5\lambda$, $d_{\text{cav}} = \lambda$ and $d_{\text{cav}} = 1.5\lambda$.

In Figure 4.19 the molecular dynamics results of the mean free paths measured inside a cavity with either fully specular or fully diffusive surface are shown together with the corresponding theoretical results. Here the same characteristic shape of the diffusive wall results can be recognised from the one-planar-wall results, where the near-wall values are lower than the corresponding theoretical case and give a steeper near-wall gradient. For the larger $d_{\mathrm{cav}} = 1.5\lambda$ case it can also be recognised that the bulk values of the effective mean free path profile, for the cavity case with diffusive surface, is higher than both the corresponding results of the cavity case, with a specular surface, and the theoretical model. This is also consistent with the results of the one-planar-wall case.

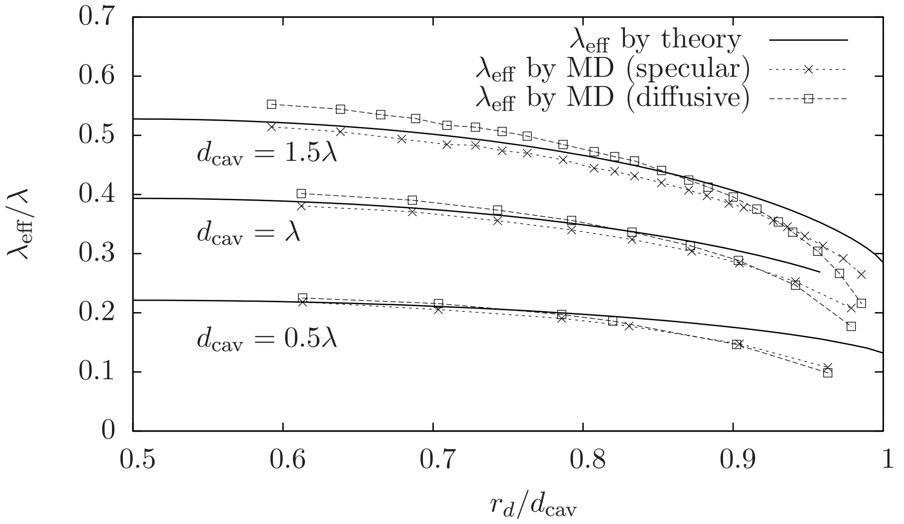

Figure 4.19: Mean free path profiles obtained from molecular dynamics with either fully specular or fully diffusive cavity surface, theoretical model achieved by from physical reasoning. The cases shown are $d_{\mathrm{cav}} = 0.5\lambda$, $d_{\mathrm{cav}} = \lambda$ and $d_{\mathrm{cav}} = 1.5\lambda$.

4.6 Discussion

In this chapter molecular dynamics has been used to record the molecular travelling distances between collisions from helium, neon and argon gases at standard temperature and pressure conditions. Then results have been compared with corresponding conventional theoretical results of Maxwellian and hard sphere molecular representations. It was shown that the values of the theoretical unconfined mean free paths were recovered for the investigated gases. It was found that neon had the largest discrepancy of the measured mean free path values which was about 1.8% lower than the theoretical value. It was also shown that the simulations of the conventional unconfined mean free path fulfil the binary collision assumption.

Planar specular and diffusive reflective walls were introduced to the molecular dynamics solver, and the mean free paths were recorded at various wall distances in order to compare with the physically derived model. It was found that the theoretical models and the molecular dynamics simulations with specular walls showed similar results for single wall geometries, for the two-parallel-planar-wall cases up to Knudsen numbers of about 0.2. The mean free path profile results achieved by diffusive walls differ significantly from the specular results, and do not compare as well to the theoretical model. Also, explicit molecular walls were simulated (with two different widths), replacing the reflecting surfaces. For these cases the effective mean free path results differed even more from the theoretical profiles than the effective mean free path results obtained using the specular or the diffusive walls. Finally, the effective mean free path profiles were investigated in the vicinity of the non-planar-wall geometries of a spherical obstacle and within a spherical cavity for both specular and diffusive reflections. In these cases the measured effective mean free path profiles showed similar characteristic shapes as the theoretical results, but differed in the bulk region for the spherical obstacle case and in the near wall region for the cavity case.

Since the present theoretical model is not derived to take molecular potentials into account causing long-range influences between the gas molecules or taking into account different molecular reflection characteristics, further investigation in this area could improve the models further. The effective mean free path derived in this thesis is used to obtain an effective viscosity which is applied with the Navier–Stokes equation in chapter 5. This assumes that the transfer of momentum between gas molecules is linearly proportional to a molecule's probability of colliding with an other gas molecule or a wall. Other interesting areas to investigate further are the different types of Knudsen layers such as the momentum Knudsen layer or the thermal Knudsen layer, which are believed to differ from each other dependent on the layers ability to transfer momentum or heat respectively. Since noble gases need some three or four collisions to equilibrate their energy with surrounding molecules [51] it is assumed that the molecular collision probability should not scale linearly with the heat transfer in the same manner as was assumed for the momentum transfer.

The results obtained in this chapter will prove useful for modelling micro gas flows using the Navier–Stokes equations by incorporating a non-linear stress/strain-rate relationship [4]. Knowledge of the effect of confining walls on the mean free path will also be useful when applying boundary conditions to the Navier–Stokes equations, because velocity-slip and temperature-jump are dependent on a near-wall value of the mean free path. In the next chapter the simple isothermal test cases of the Couette and the Poiseuille flows are presented using the present effective mean free path dependent parameter μ_{eff} in the Navier–Stokes equations, with first- and second-order velocity-slip boundary conditions.

Chapter 5

Extended Navier–Stokes equations

In this chapter an extension to the Navier–Stokes equations is investigated. The extension consists of incorporating the influence of the effective mean free path to viscosity and to the conventional velocity-slip boundary conditions.

Returning to the conventional derivation of the viscosity dependence on the mean free path in Eqn (2.28), it was stated that the a parameter was describing the same quantity as the unbounded λ. If the gas is confined however then the gas molecules do not have an average travelling distance of λ before experiencing collisions any more. The difference in the derivation of the mean free path and viscosity relation for cases of solid boundary interference can be incorporated in Eqn. (2.25). Here the velocity changes between characteristic layers of the flow. The layers are separated by the geometric dependent quantity $a'(\mathrm{n})$, where the wall normal coordinate, $\mathbf{n}$, and the wall tangential coordinate, $\mathbf{t}$, are used instead of the coordinates $\mathbf{y}$ and $\mathbf{x}$. The quantity $a'(\mathrm{n})$ describes the local distance from the wall normal distance, n, at which a molecule has the average travelling distance a' before experiencing collisions with either other gas molecules or walls. Since this quantity describes the same as λ_{eff} it can be replaced by this quantity in the following equation of velocity change between layers:

$$v_{\mathrm{t}}|_{\mathrm{n}} = v_{\mathrm{t}}|_{\mathrm{n}-a'(\mathrm{n})} + \lambda_{\mathrm{eff}} \frac{dv_{\mathrm{t}}}{d\mathbf{n}}. \tag{5.1}$$

By again using Eqn (2.23), which expresses the sheer stress as momentum exchange between layers, the following expression is achieved:

$$\Pi_{\mathrm{xn}} = -\beta nmC\lambda_{\mathrm{eff}} \frac{dv_{\mathrm{t}}}{d\mathbf{n}}. \tag{5.2}$$

where C is the average thermal speed from the Maxwellian velocity distribution and β has the value $\beta = 1/2$. The relationship between the effective mean free path and the new effective viscosity is achieved by comparison to Newtons definition of the sheer stress tensor in Eqn (2.22) i.e.:

$$\mu_{\text{eff}} = \lambda_{\text{eff}}\rho\sqrt{\frac{2RT}{\pi}}. \tag{5.3}$$

In order to intuitively visualise how the mean free path affects the cross-sectional momentum transfer in a micro-channel Figure 2.5 is modified by including two confining walls as is shown in Figure 5.1. Then the same derivation of the viscosity dependence on the mean free path can be used as in section 2.4.1 with the exception that the cross-sectional average spacing between collisions is no longer at a constant spacing (a) (which was approximated to be equal to λ). The location of the planes where the molecular collisions on average occur are instead replaced with $a'(\mathrm{n})$ symbolising the non-uniform spacing between these planes with respect to the wall normal distance n.

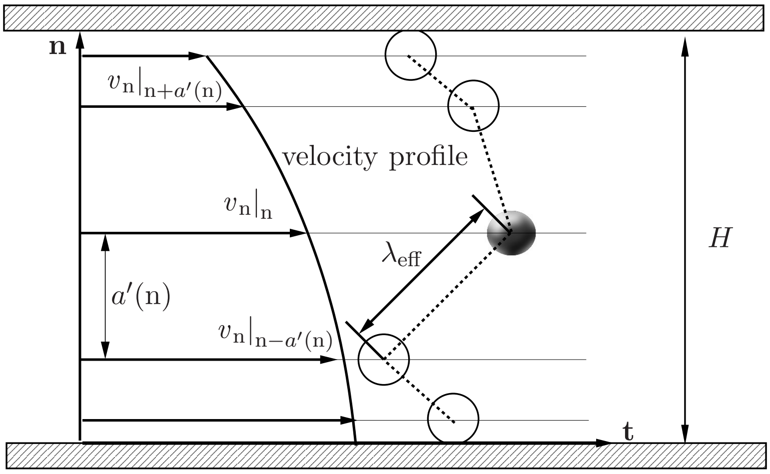

Figure 5.1: Molecular transport of momentum from the plane at n$-a'(\mathrm{n})$ to the plane at n, where $a'(\mathrm{n})$ is the vertical separation of the planes where collisions on average occur and H is the wall separation.

Generally, kinetic derivations of the velocity slip such as the one performed by Cercignani are based on a diffuse reflection approximation for the gas/surface interaction [8]. An example of such an approximation is to use a correction for the gas/surface interaction using the coefficient $(2-\sigma)/\sigma$ in Eq. (2.42). The surface not only modifies the slip coefficients but also affects the mean free path locally. The first- and second-order velocity-slip expressions that are applied are therefore based on Eqns (2.44) and (2.50), respectively, and use a mean free path modified to incorporate the effect of a surface through, λ_{eff}, i.e.

$$\boldsymbol{v}_{\text{w}} = -D_1'\lambda_{\text{eff}}\left(\frac{\partial \boldsymbol{v}}{\partial \mathbf{n}}\right)_{\text{w}}, \tag{5.4}$$

and

$$\boldsymbol{v}_{\mathrm{w}} = -D_2'\lambda_{\mathrm{eff}}\left(\frac{\partial \boldsymbol{v}}{\partial \mathbf{n}}\right)_{\mathrm{w}} - D_3'\lambda_{\mathrm{eff}}^2\left(\frac{\partial^2 \boldsymbol{v}}{\partial \mathbf{n}^2}\right)_{\mathrm{w}} . \tag{5.5}$$

The conventional velocity-slip definitions represent surface effects through their slip coefficients rather than through the mean free path model. The expressions in Eqns (5.4) (5.5) have coefficients D_1', D_2' and D_3' different from the conventional coefficients D_1 and D_2. This is because λ_{eff} is expected to incorporate some surface effects, most likely requiring a change in the slip coefficient values.

An investigation, based on DSMC results, has been performed by Pan *et al.* [48] of the influence of the slip coefficients on the velocity-slip boundary conditions. They argued that the slip coefficients should depend not only on macroscopic parameters but also on the microscopic parameters such as molecular mass, diameter and number density. In the investigation by Pan *et al.* it is found that a slip coefficient is a function of the mean free path of molecules colliding with a wall. In the new slip boundary conditions, however, the slip coefficients are fixed but the mean free path varies with the wall-distance, which should have the same overall effect as the derived velocity-slip of Pan *et al.*

Other authors such as Shen *et al.* [57] and Yuhong and Chan [57] have also proposed methods that extend the validity of the Navier–Stokes equations to higher Kn by incorporating geometry-dependent mean free paths to the continuum methods. Another alternative approach, using a wall-function, is empirically derived by Lockerby *et al.* [34], which is based on DSMC results. This wall-function scales the viscosity used in the Navier-Stokes equations in a similar manner as for the new theory. This method yields good results up to about $Kn = 1$ for the Poiseuille velocity profile.

In the next section Couette flow and Poiseuille flow cases are solved using both the Navier-Stokes equations extended by using the effective mean free path, $\mathrm{NS}_{\mathrm{eff}}$ and the conventional Navier-Stokes equations, NS. The effective mean free path methods that are applied for solving the Navier–Stokes equations are here referred to as the TMFP, EMSP and EMDIFF models. Here TMFP is the theoretically derived effective mean free path obtained by λJ, where J is from Eqn (3.7) and EMSP and EMDIFF are empirical models from the molecular dynamics simulation that use specular and diffusive reflections respectively. The normalised effective mean free path, also referred to as J, for the two latter models are obtained from the following expression:

$$\begin{aligned}\frac{\lambda_{\mathrm{eff}}}{\lambda} = 1- \Bigg[& A_1 \exp\left(\frac{-A_2 \mathrm{n}}{\lambda_{\mathrm{Ne}}}\right) + A_3 \exp\left(\frac{-A_4 \mathrm{n}}{\lambda_{\mathrm{Ne}}}\right) \\ & + A_1 \exp\left(\frac{-A_2 (H-\mathrm{n})}{\lambda_{\mathrm{Ne}}}\right) + A_3 \exp\left(\frac{-A_4 (H-\mathrm{n})}{\lambda_{\mathrm{Ne}}}\right)\Bigg] ,\end{aligned} \tag{5.6}$$

where EMDIFF uses the coefficients $A_1 = 0.30318$, $A_2 = 9.38115$, $A_3 = 0.69682$ and

$A_4 = 1.11005$, and EMSP uses the specular wall coefficients shown in Table 4.6. The corresponding one wall-profiles are shown for the empirical models in Figure 4.14.

5.1 Case solving using extended Navier-Stokes equations

Isothermal, fully developed velocity profiles in planar Couette and Poiseuille flow cases are calculated using the modified Stokes equation:

$$\frac{\partial}{\partial \mathbf{n}}\left[\mu_{\text{eff}}\frac{\partial v_t}{\partial \mathbf{n}}\right] = \frac{\partial p}{\partial \mathbf{t}}, \tag{5.7}$$

where v_t is the tangential component of the velocity $\boldsymbol{v}$ and the effective viscosity is applied through the relationship to the effective mean free path, expressed in Eqn 5.3. The velocity component v_t is assumed to vary only in the direction normal to the wall, the **n**-direction. This model is applied with the first-order velocity-slip of Eqn (5.4) and with the second-order velocity-slip of Eqn (5.5). The Couette and Poiseuille flow cases are solved for just the half of the channel ($H/2 < \text{n} < H$). For these velocity-slip boundary conditions the near-wall values of λ_eff, are applied at $\text{n} = H$.

The slip coefficients used in this chapter are listed in Table 5.1. The coefficients for the NS$_\text{eff}$ models are chosen by trial and error with consideration given to achieving reasonable results for both the Couette and the Poiseuille cases.

Table 5.1: Coefficients for velocity-slip models used in this chapter. The coefficients for the conventional Navier-Stokes equations (NS) are from Hadjiconstantinou [23].

Model	D_1'	D_2'	D_3'	D_1	D_2
NS$_\text{eff}$, second-order BC (TMFP)		0.05	0.75		
NS$_\text{eff}$, first-order BC (TMFP)	1.0				
NS$_\text{eff}$, second-order BC (EMSP)		0.05	0.60		
NS$_\text{eff}$, BC (EMSP)	1.0				
NS$_\text{eff}$, second-order BC (EMDIFF)		0.05	0.56		
NS$_\text{eff}$, first-order BC (EMDIFF)	1.0				
NS, second-order BC				1.1466	0.647
NS, first-order BC				1.1466	

It should be noted that the second order velocity slip model is derived from an expansion of the first order model using λ as a smallness parameter. It is generally considered that the second order term is a correction to the first order term and that the same coefficients for D_1' and D_2' should therefore be used. However this yielded unreasonable results which is why these coefficients instead where chosen by trial and error. Due to this incomplete theoretical derivation of the present applied boundary condition it is not certain that the new model is generally applicable for all cases.

It is shown by experimental investigators, such as Turner *et al.* [63], that micro gas flows have compressible characteristics even for flow velocities bellow Mach 0.3. However, the normalised velocity profile in the channel cross section of the flow is calculated here by assuming fully developed incompressible flow. Although it is not investigated here, the density of the flow could also be solved by incorporating the ideal gas law to the solution method knowing the pressure. This solution method is obtained from Kandlikar *et al.* [28].

5.1.1 Couette flow

A schematic representation of Couette flow is given in Figure 5.2 illustrating the gas movement caused by the difference of the wall velocities in the wall-tangential direction.

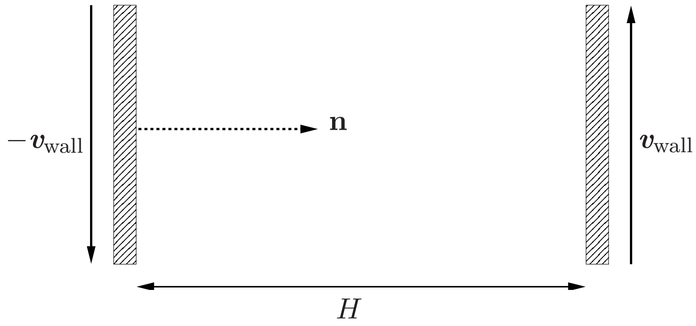

Figure 5.2: Schematic of Couette flow. The flow is driven by the left wall moving with the velocity -$\boldsymbol{v}_{\text{wall}}$ and the right wall moving with the velocity $\boldsymbol{v}_{\text{wall}}$. Also shown is the channel wall separation, H, and the wall-normal coordinate $\mathbf{n}$.

In Couette flow the pressure gradient of Eqn (5.7) is assumed to be negligible, yielding the governing equation:

$$\frac{\partial}{\partial \mathbf{n}}\left(\mu_{\text{eff}}\frac{\partial v_{\text{t}}}{\partial \mathbf{n}}\right) = 0. \tag{5.8}$$

The solution to this equation using the first-order velocity-slip, is

$$\frac{v_{\text{t}}}{v_{\text{wall}}} = \frac{F(\text{n} - H/2) - F(\text{n} = H/2)}{F(\text{n} = H) + D_1'\lambda - F(\text{n} = H/2)}, \tag{5.9}$$

where v_{wall} is the tangential component of the wall velocity and

$$F(\text{n}) = \int \frac{1}{J(\text{n} - H/2)} d\mathbf{n}. \tag{5.10}$$

The NS$_{\text{eff}}$ solution using the second-order velocity-slip is:

$$\frac{v_{\text{t}}}{v_{\text{wall}}} = \frac{F(\text{n} - H/2) - F(\text{n} = H/2)}{F(\text{n} = H) + D_2'\lambda - D_3'\lambda^2 J'(\text{n} = H) - F(\text{n} = H/2)}, \tag{5.11}$$

where

$$J'(\text{n}) = \frac{dJ(\text{n} - H/2)}{d\text{n}}. \tag{5.12}$$

The conventional solution to Eqn (5.8), with constant viscosity and boundary conditions applied using λ, is as follows:[1]

$$\frac{v_{\text{t}}}{v_{\text{wall}}} = \frac{\text{n} + H/2}{H/2 + D_1\lambda}. \tag{5.13}$$

The NS$_{\text{eff}}$ solutions of Eqns (5.9) and (5.11) for the TMFP, EMSP and EMDIFF models and the NS solution of Eqn (5.13) are compared in Figures 5.3, 5.4 and 5.5 respectively for different Kn. The velocity profiles are compared to the conventional Navier-Stokes (NS) for $Kn = 0.01$ and $Kn = 0.1$. Comparisons are made to the DSMC method by Bird [6] and to the BGK results of Sharipov [56] for the cases $Kn = 0.1$, Kn=0.5 and Kn=1. The results of the figures are jointly commented on below for the different Kn. No significant difference in results can be distinguished between the first- and second-order velocity-slip up to $Kn_D = 1$. In these figures n $= H/2$ is in the centre of the channel.

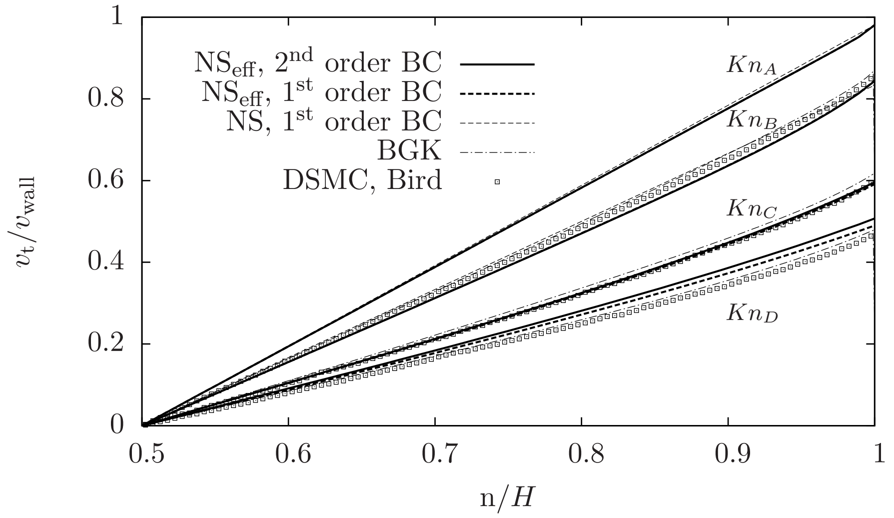

Figure 5.3: Half-channel Couette flow velocity profiles using the TMFP effective viscosity model (NS$_{\text{eff}}$), with first- and second-order velocity-slip boundary conditions (BC), where $Kn_A = 0.01$, $Kn_B = 0.1$, $Kn_C = 0.5$ and $Kn_D = 1$.

---

[1] The second-order velocity-slip solution does not exist, because there is no second-order gradient of the velocity.

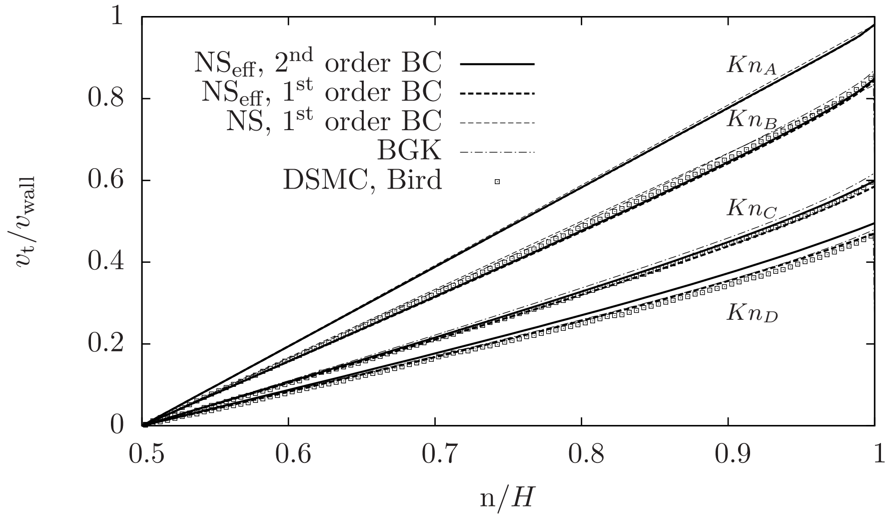

Figure 5.4: Half-channel Couette flow velocity profiles using the EMSP effective viscosity model (NS$_{\mathrm{eff}}$), with first- and second-order velocity-slip boundary conditions (BC), where $Kn_A = 0.01$, $Kn_B = 0.1$, $Kn_C = 0.5$ and $Kn_D = 1$.

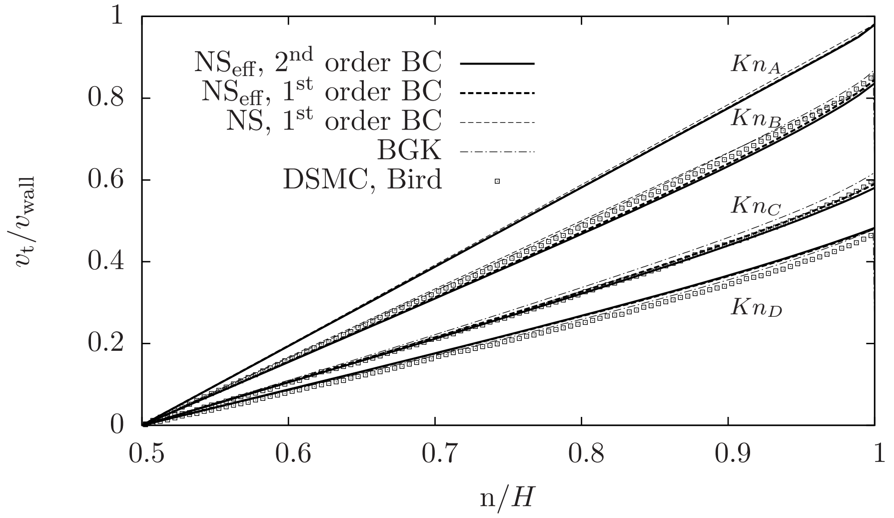

Figure 5.5: Half-channel Couette flow velocity profiles using the EMDIFF effective viscosity model (NS$_{\mathrm{eff}}$), with first- and second-order velocity-slip boundary conditions (BC), where $Kn_A = 0.01$, $Kn_B = 0.1$, $Kn_C = 0.5$ and $Kn_D = 1$.

- It is seen that for $Kn_A = 0.01$ all of the solutions have sufficiently linear profiles to match the conventional NS results well.

- Even for the $Kn_B = 0.1$ case most of the profiles show similar results. All the models have about the same amount of velocity-slip at the wall, where as the $\mathrm{NS_{eff}}$ -models have slightly more curved profiles and deviate the most at n ≈ 0.85 at which point these profiles are about 1% below the validation data.

- For $Kn_C = 0.5$ all the $\mathrm{NS_{eff}}$ models fit the validation data of DSMC very well. For this case the validation data of the DSMC method is about 0.5% lower than the BGK results in the near-wall area and the NS models are omitted since they are not applicable at this Kn.

- For $Kn_D = 1$ there is a significant difference between the $\mathrm{NS_{eff}}$ first- and second-order velocity-slip models, except for the EMDIFF model. The EMSP model yields the best match with the DSMC results for the first-order velocity slip. It is shown that the second-order velocity-slip has a velocity profile that is about 1% higher than the first-order velocity-slip in the near-wall area for the TMFP model whereas the corresponding difference is about 2% for the EMDIFF model. The DSMC and BGK methods both have results very similar to each other. The results of the TMFP, EMSP and EMDIFF methods for the second-order velocity-slip are about 4%, 2% and 1% higher than the DSMC results respectively in the near-wall area.

It is considered that the EMSP model with first order velocity slip is the $\mathrm{NS_{eff}}$ model that compares best with the DSMC data for these cases.

5.1.2 Poiseuille flow

A schematic representation of Poiseuille flow is given in Figure 5.6 illustrating the gas movement caused by the pressure difference between the inlet and the outlet.

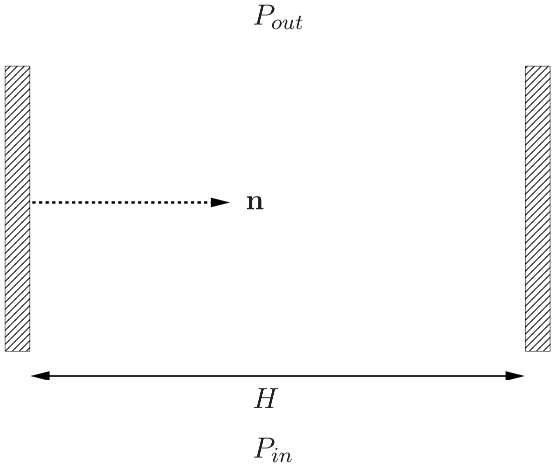

Figure 5.6: Schematic of the Poiseuille flow. The flow is driven by the pressure difference between P_{in} and P_{out} at the two ends of the channel. For this case the two confining walls are stationary. Also shown is the channel wall separation, H, and the wall-normal coordinate $\mathbf{n}$.

In the next two sections the velocity profiles and the mass-flow rates for isothermal, fully developed Poiseuille flow cases are solved in planar-wall geometries for the $\mathrm{NS_{eff}}$ and NS models with first- and second-order velocity-slip boundary conditions.

Velocity profile results

In this case the solution to Eqn (5.7) using the $\mathrm{NS_{eff}}$ model with first-order λ_{eff}-dependent velocity-slip is as follows:

$$\frac{v_{\mathrm{t}}}{v_0} = \frac{8}{H^2}\left[G\left(H\right) + D_1'\lambda\frac{H}{2} - G(\mathrm{n} - H/2)\right], \tag{5.14}$$

where

$$G(\mathrm{n} - H/2) = \int \frac{\mathrm{n} - H/2}{J(\mathrm{n} - H/2)} d\mathbf{n} \quad \text{and} \quad v_0 = -\frac{H^2}{8\mu}\frac{dp}{d\mathbf{t}}. \tag{5.15}$$

The $\mathrm{NS_{eff}}$ solution with second-order λ_{eff}-dependent velocity slip is:

$$\frac{v_{\mathrm{t}}}{v_0} = \frac{8}{H^2}\left[G\left(H\right) + D_2'\lambda\frac{H}{2} + D_3'\lambda^2\left[J(H) - \frac{H}{2}J'(H)\right] - G(\mathrm{n} - H/2)\right], \tag{5.16}$$

where

$$J'(\mathrm{n} - H/2) = \frac{dJ(\mathrm{n} - H/2)}{d\mathbf{n}}. \tag{5.17}$$

The solution of the conventional NS equation, with constant viscosity and first-order velocity slip using the unconfined λ, is:

$$\frac{v_\mathrm{t}}{v_0} = 1 - 4\left(\frac{\mathrm{n} - H/2}{H}\right)^2 + 4D_1\frac{\lambda}{H}, \tag{5.18}$$

and the NS solution with second-order velocity slip using the unconfined λ is:

$$\frac{v_\mathrm{t}}{v_0} = 1 - 4\left(\frac{\mathrm{n} - H/2}{H}\right)^2 + 4D_1\frac{\lambda}{H} + 8D_2\left(\frac{\lambda}{H}\right)^2. \tag{5.19}$$

The half-channel velocity profiles of the NS$_\mathrm{eff}$ and NS models for Poiseuille flow are shown in Figures 5.7, 5.8 and 5.9. The results of the figures are jointly commented below for the different values of Kn. No significant difference in results can be distinguished between any of the models for the $Kn_B = 0.1$ case, indicating that they are likely to asymptotically approach the results of the conventional NS models for lower Kn. There is only a marginal difference between the TMFP, EMSP and EMDIFF models up to $Kn = 1$. In these figures it is seen that the main difference between the NS$_\mathrm{eff}$ models is generally that they have similar shape to each other but different velocity-slip.

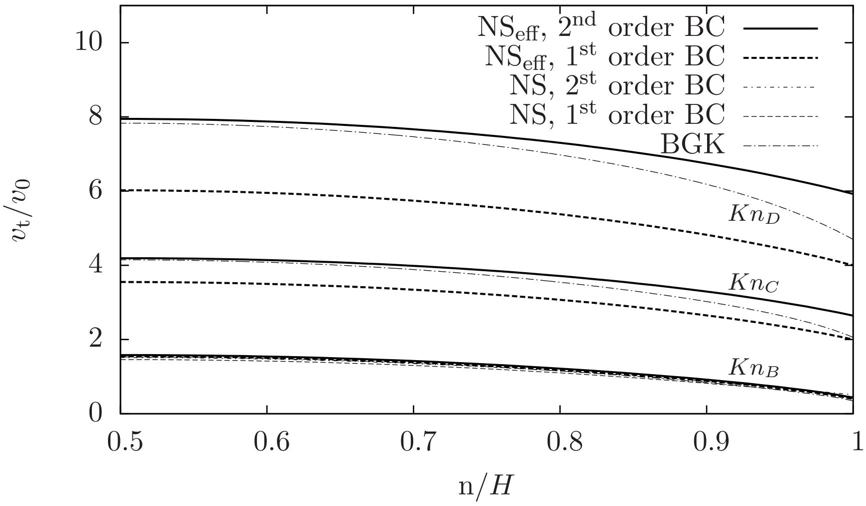

Figure 5.7: Half-channel Poiseuille flow velocity profiles using the TMFP effective viscosity model (NS$_\mathrm{eff}$), with first- and second-order velocity-slip boundary conditions (BC), where $Kn_B = 0.1$, $Kn_C = 0.5$ and $Kn_D = 1$.

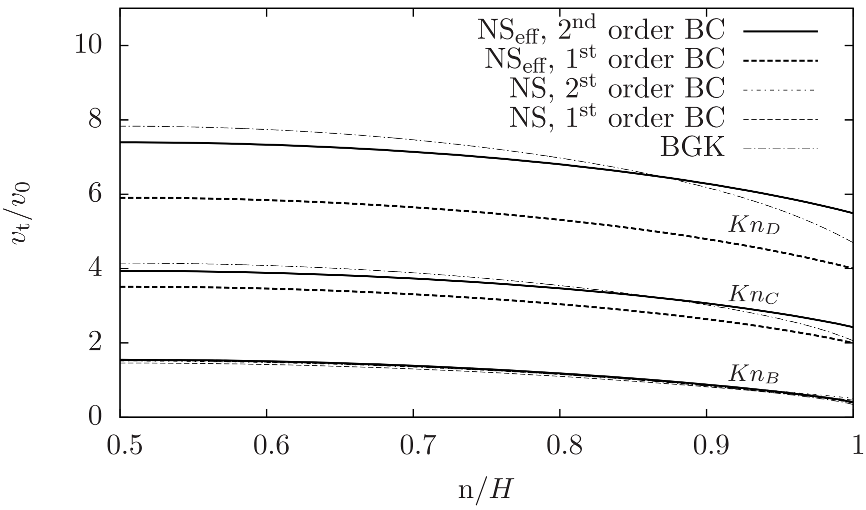

Figure 5.8: Half-channel Poiseuille flow velocity profiles using the EMSP effective viscosity model ($\mathrm{NS_{eff}}$), with first- and second-order velocity-slip boundary conditions (BC), where $Kn_B = 0.1$, $Kn_C = 0.5$ and $Kn_D = 1$.

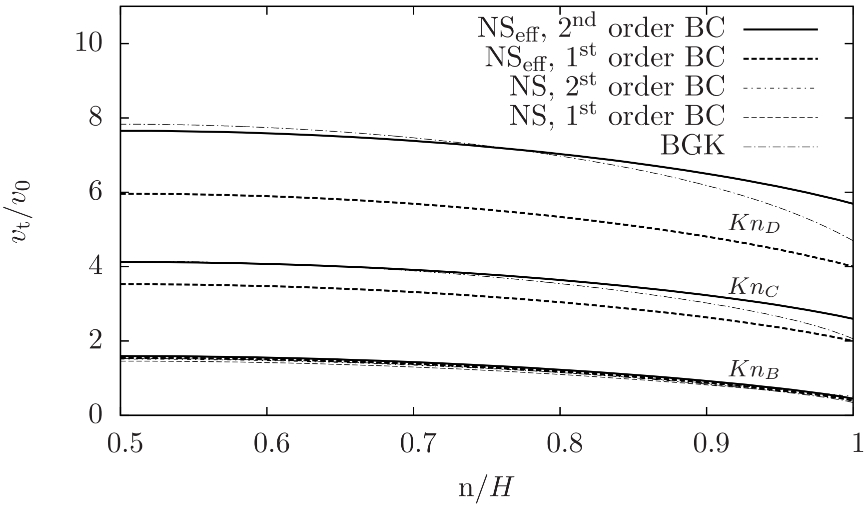

Figure 5.9: Half-channel Poiseuille flow velocity profiles using the EMDIFF effective viscosity model ($\mathrm{NS_{eff}}$), with first- and second-order velocity-slip boundary conditions (BC), where $Kn_B = 0.1$, $Kn_C = 0.5$ and $Kn_D = 1$.

- For the $Kn_B = 0.1$ case all the presented models show similar results indicating that a convergence of the models is likely for even smaller Kn. For the Poiseuille case this is the only Kn that the conventional NS models are compared with since $Kn = 0.1$ is generally considered as the upper validity limit of this method.

- For the $Kn_C = 0.5$ case all the velocity profiles using different order of velocity slip differ. It is seen that the $\mathrm{NS_{eff}}$ model with second-order velocity-slip achieves good results in the bulk area of the flow. Since the validation data of the BGK method has a more curved velocity profile than the new models the $\mathrm{NS_{eff}}$ model using first-order velocity-slip matches the BGK data better in the near-wall area.

- For the $Kn_D = 1$ case it is seen that the $\mathrm{NS_{eff}}$ models have velocity profiles which are considerably flatter than the BGK results. For the EMSP method using second-order velocity-slip a reasonable cross-sectional average of the velocity profile compared to the BGK method is captured. Both the TMFP and EMDIFF models using second-order velocity-slip show similarly good results in the bulk flow compared to the BGK method but their velocity profiles are both about 10% too high in the near-wall area.

It can be concluded that for the Poiseuille velocity profiles the TMFP, EMSP and EMDIFF models show an asymptotic approach to the NS results for flows approaching the continuum regime. For $Kn = 0.5$ the velocity profiles of the models tested deviate from the validation data although the second-order slip still acquires a seemingly correct cross-sectional average of the velocity.

Mass flow rate results

The mass flow rates are studied in this section using the TMFP, EMSP and EMDIFF models and compared with experimental results by Ewart *et al.* [15] and with the BGK results by Sharipov [56] for degrees of rarefaction ranging from $Kn \approx 0.1$ to $Kn \approx 90$.

The experimental measurements by Ewart *et al.* are made for helium gas, driven by a pressure difference which, for various cases, has the ratios of 3, 4 and 5 between the inlet and the outlet of the channel. The experimental channel dimensions are: height $H = 9.38\mu\mathrm{m}$; width $W = 492\mu\mathrm{m}$; and length $L = 9.39\mathrm{mm}$. Since this channel is relatively wide compared to its height, it is assumed that a comparison with our model for just two planar walls is valid. However, according to Sharipov [56] there is still an influence of the lateral walls, here separated by W; the error due to this influence can be taken into account by multiplying the predicted mass flow rate by $1 - 0.63H/W = 0.99$.

In order to compare our results with experiment, the velocity-dependent mass flow rate is calculated using the following relation:

$$\dot{m} = \rho \left\langle v_{\mathrm{t}} \right\rangle A_{CS} = \frac{p \left\langle v_{\mathrm{t}} \right\rangle A_{CS}}{RT}, \tag{5.20}$$

where A_{CS} is the area of the cross section of the channel and

$$\widetilde{v}_{\mathrm{t}} = \frac{\left\langle v_{\mathrm{t}} \right\rangle}{v_0} = \frac{2}{H} \int_0^{H/2} \frac{v_{\mathrm{t}}}{v_0} d\mathbf{n} \tag{5.21}$$

is the normalised average velocity across the channel height. Here the mass flow rate definition of Eqn (5.20) applies the averaged velocities of the four velocity expressions of Eqns (5.18), (5.19), (5.14) and (5.16) and is normalised by the quantity

$$\dot{m}_0 = -\frac{A_{CS} H}{\sqrt{2RT}} \frac{dp}{d\mathbf{t}}. \tag{5.22}$$

The normalised expression is then obtained for the mass flow rate,

$$\frac{\dot{m}}{\dot{m}_0} = \frac{v_0}{\dot{m}_0} \frac{p A_{CS}}{RT} \widetilde{v}_{\mathrm{t}} = \frac{\sqrt{\pi}}{8} \frac{H}{\lambda} \widetilde{v}_{\mathrm{t}} = \frac{\delta}{4} \widetilde{v}_{\mathrm{t}}(\delta), \tag{5.23}$$

where the inverse rarefaction parameter is

$$\delta = \frac{\sqrt{\pi}}{2} \frac{H}{\lambda}. \tag{5.24}$$

The results of the mass flow rates of the $\mathrm{NS_{eff}}$ and NS equations using first- and second-order velocity-slip are shown in Figures 5.10, 5.11 and 5.12, together with the BGK results of Sharipov [56] and the experimental results of Ewart *et al.* [15], where height of the error bars of the experimental data is set to 4.5% of the normalised mass flow rate values.

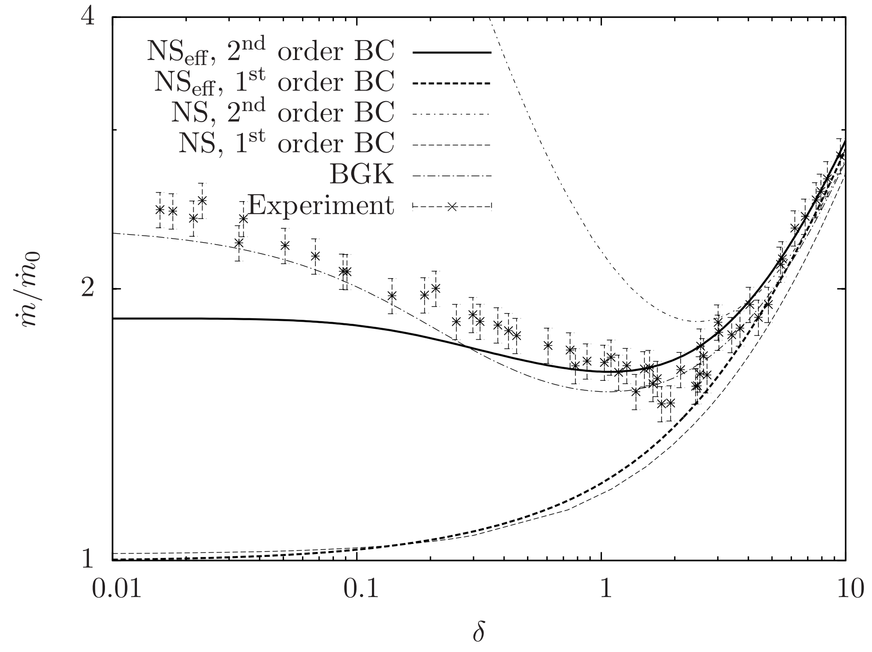

Figure 5.10: Mass flow results of the TMFP model in NS$_{\text{eff}}$ with first- and second-order boundary conditions (BC). The results are compared with BGK solutions by Sharipov [56] and experimental results of Ewart *et al.* [15].

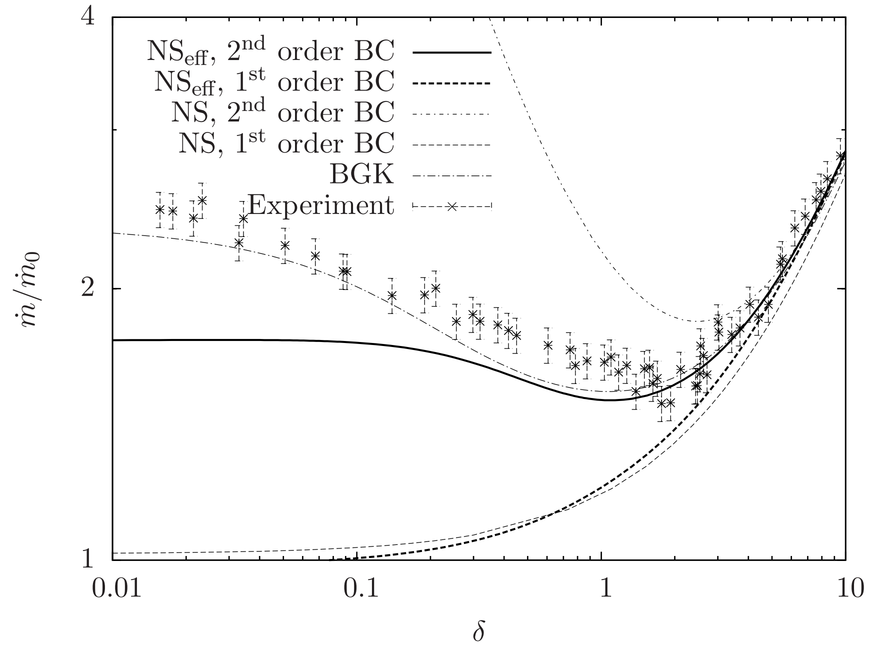

Figure 5.11: Mass flow results of the EMSP model in NS$_{\text{eff}}$ with first- and second-order boundary conditions (BC). The results are compared with BGK solutions by Sharipov [56] and experimental results of Ewart *et al.* [15].

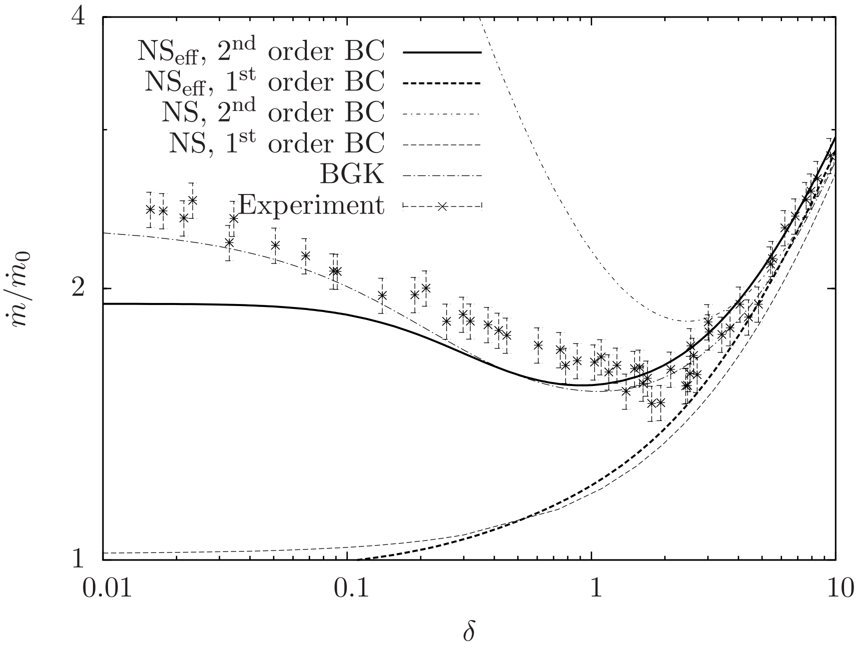

Figure 5.12: Mass flow results of the EMDIFF model in NS$_{\text{eff}}$ with first- and second-order boundary conditions (BC). The results are compared with BGK solutions by Sharipov [56] and experimental results of Ewart *et al.* [15].

The Figures 5.10, 5.11 and 5.12 show that all of the models are asymptotic to the experimental data for low Kn (i.e. high δ), which fulfils the requirement that the influence of the effective viscosity and the effective mean free path should decay with decreasing degree of rarefaction. It is only the NS$_{\text{eff}}$ and NS models with second-order velocity-slip that capture the mass flow minimum, which occurs for the conventional model at $\delta \approx 2$ and for the new model at $\delta \approx 1$. The validation data of the BGK-model and the experimental data have a minimum at $\delta \approx 1.2$. The conventional Navier-Stokes equations are solved by Colin et al. [50] with second-order velocity boundary conditions applied with Hadjiconstantinou's velocity-slip coefficients [23] showing good mass-flow rate results for roughly $Kn < 0.3$. The NS model with second-order velocity-slip predicts a mass flow rate that is unbounded and therefore non-physical for low δ-values. The NS$_{\text{eff}}$ models show a clear minimum at $Kn \approx 1.5$. There after, the mass flow rate of the TMFP model lies between the experimental data and the BGK results down to $\delta \approx 0.2$. The corresponding mass flow rates for the EMSP and EMDIFF models are slightly closer to the BGK results than the experimental results. The TMFP, EMSP and EMDIFF models start to deviate from the validation data, by asymptoting to values of about 1.9, 1.8 and 1.9 respectively at about $\delta \approx 0.05$. The mass flow rate results up to $Kn = 1$ can be realised by inspection of the velocity profiles for the Kn_D cases of Figures 5.10, 5.11 and 5.12, where the velocity profiles of the TMFP and EMDIFF models are relatively high in comparison to the EMSP model which is, on average, slightly below the BGK velocity profile. It should also be noted that the $\mathrm{NS_{eff}}$ based first-order velocity-slip models show very good results down to $\delta \approx 4$.

In Table 5.2 an approximate range of applicability is listed for the NS-based models and the BGK-model, within the δ inspection range of 0.3–20. These applicability ranges are estimated by the ability of the different models to reproduce mass flow rates similar to the experimental data within approximately the double length reach of the stated error bars.

Table 5.2: Applicability ranges of the tested models, determined by comparing their ability to accurately predict the experimentally determined mass flow rate as measured by Ewart *et al.* [15].

Model	**Approximate range of applicability**	
	In terms of δ	In terms of Kn
$\mathrm{NS_{eff}}$, second-order BC (TMFP)	0.3—10	0.09—2.95
$\mathrm{NS_{eff}}$, first-order BC (TMFP)	4—10	0.09—0.22
$\mathrm{NS_{eff}}$, second-order BC (EMSP)	0.3—10	0.09—2.95
$\mathrm{NS_{eff}}$, first-order BC (EMSP)	4—10	0.09—0.22
$\mathrm{NS_{eff}}$, second-order BC (EMDIFF)	0.3—10	0.09—2.95
$\mathrm{NS_{eff}}$, first-order BC (EMDIFF)	4—10	0.09—0.22
NS, second-order BC [a]	3—10	0.09—0.30
NS, first-order BC	4—15	0.04—0.06
BGK	0.01—10	0.09—88.6

---

[a] It should be noted that the investigators Colin *et al.* [11] and Maurer *et al.* [41] found that for special cases the applicability range of NS with second-order boundary conditions reached up to $Kn = 0.25$ and $Kn = 0.3$ respectively.

5.2 Discussion

The new models based on the effective mean free path description from a theoretical derivation as well from molecular dynamics results have been used to extend the applicability of the Navier-Stokes equations for the classical Couette and Poiseuille flow cases. In order to simplify the cases, they are considered to be isothermal and to have only one-dimensional flow solutions in planar-wall geometries, i.e. the variables only change in the direction normal to the walls. Also the gas is assumed to be monatomic in order for the molecular dynamics results of the effective mean free path to be applicable. The new models are compared to BGK and DSMC results for Couette flow, and the BGK and experimental mass-flow results for the Poiseuille flow case.

The Couette flow results show that the present extended Navier-Stokes equations have a non-linear velocity profile similar to the validation data of the BGK and DSMC methods. The new models are considered to capture similar velocity profiles to the validation data up to $Kn \approx 1$. It is found that the highest Kn case that the conventional Navier-Stokes equations are applicable to solve the Couette flow for is $Kn = 0.1$.

For Poiseuille flow, it is considered that the present extended Navier-Stokes results agree with the conventional Navier-Stokes results for $Kn = 0.1$. For Kn up to unity it is found that the velocity profiles of the extended Navier-Stokes equations using second-order velocity-slip manage to capture the bulk velocity of the validation data, while in the near-wall region the new model using first-order velocity-slip manages shows results more similar to the validation data.

In solving the Poiseuille flow it is found that the extended Navier-Stokes equations can only predict the mass-flow-minimum by using second-order boundary conditions which also is the case for the conventional Navier-Stokes equations. However, the mass flow rates predicted by the extended Navier-Stokes models approach a bounded value at $Kn \approx 10$, which is some 10% lower than the bounded mass flow rate results of the validation data.

For the tested cases the results of the new extension of the Navier-Stokes equations converge with the results of the conventional Navier-Stokes equations at low Kn. This convergence is important for $Kn \lesssim 0.1$ since the conventional Navier-Stokes equations are generally considered to be correct for in this region [17]. For larger Kn the extended Navier-Stokes equations can be used to about $Kn \approx 3$. However, at $Kn = 1$ they predict velocity profiles with roughly the same average of the cross sectional velocity as the corresponding BGK method results, but the new velocity profiles are flatter in shape.

Chapter 6

Discussion and conclusions

In recent years vast improvements in manufacturing of micro-mechanical systems has been made. It is however known that the conventional fluid modelling techniques consisting of the Navier–Stokes–Fourier equations do not capture the correct flow description at these length scales [17]. Clear examples of cases where the conventional methods fail are the torque exerted on a disk by the reading head in a hard disc drive [29] or the occurrence of the mass-flow minimum which has been experimentally observed for helium gas driven in Poiseuille flows, at a certain level of rarefaction [15]. A better understanding of the gas flow behaviour on the micro-scale (micro gas flows) would yield a more profitable production of micro-mechanical systems. A better understanding of micro gas flows would also yield better knowledge of biological effects on the micro scale such as insects' perception of sound [26] or the way medical or polluting substances affect the micro-channels of our lungs [19]. Due to many beneficial application areas of better flow descriptions on the micro-scale, and also due to general thirst of knowledge, investigators are now seeking new modelling techniques or extensions to the Navier–Stokes–Fourier equations to obtain good flow descriptions at this length scale.

To describe micro gas flows it is convenient to use the key parameter, the Knudsen number, Kn, which describes a gas state of rarefaction or equivalently its state of non-equilibrium. The Kn parameter is the ratio of the average travelling distance of the gas molecules between successive collisions, the mean free path, to the geometrical length scale of the problem.

The main difficulty of describing gas flows on the micro-scale as opposed to describing them on the macro-scale is that the equilibrium description becomes invalid for standard pressure and temperature gases in channels where the walls are separated by roughly 10μm, which roughly corresponds to $Kn \approx 0.01$ for neon gas at standard temperature and pressure. It is generally considered that the Navier–Stokes–Fourier equations can predict flows up to $Kn \approx 0.1$ when applied with discontinuous velocity and temperature boundary conditions, referred to as velocity-slip and temperature-jump respectively [17]. There are alternative methods such as the particle-based direct simulation Monte Carlo method (DSMC) and various simplified solution methods of the Boltzmann equation, such as the BGK method, which are appropriate for solving rarefied gas flows for all degrees of rarefaction. However these methods are more expensive in terms of computational effort. Many investigators therefore focus on deriving combinations of more accurate but costly methods with the computationally cheaper Navier–Stokes–Fourier equations resulting in hybrid methods. However, a valid extension to the purely continuum-based Navier–Stokes–Fourier equations for $Kn > 0.1$ cases is interesting because it would be cheap in terms of computational cost, and this method converges with the conventional Navier–Stokes–Fourier equations for macro-scale flows.

In this thesis an extension of the isothermal Navier–Stokes–Fourier equations, the Navier–Stokes equations, is derived. This method is based on a description of how the travelling distance of molecules between collisions, the free path, is terminated by the gas molecules colliding with solid walls in addition to the inter-gas molecular collisions. The average of these distances is here considered to be a geometry-dependent mean free path referred to as the effective mean free path. An expression for the effective mean free path is first theoretically derived and then validated using the deterministic modelling approach of molecular dynamics.

The theoretically derived effective mean free path is based on a gas molecule's probability of colliding with other gas molecules in addition to to solid walls. The effective mean free path is described by an exponential probability function, which scales the unconfined value of the conventional mean free path. The theoretically effective mean free path model is investigated in the close vicinity of geometries with one planar wall, two planar walls, a spherical obstacle and a spherically shaped cavity.

For the one-planar-wall case it is found that the effective mean free path fulfils intuitive requirements of approaching a value of half the unconfined mean free path in the near-wall region and approaching the unconfined value of the conventional mean free path in the bulk of the gas. For the two-planar-wall case with the walls widely separated, it is shown that the same requirements as for the effective mean free path for the one wall are fulfilled. However, as the walls are situated close to each other compared to the length measure of the unconfined mean free path it is observed that there is an overlapping effect of the gas molecular collision probabilities caused by both the walls which results in the effective mean free path profiles to be flatter and lower than for the cases where the walls are widely separated. As the two planar walls are placed at a distance from each other equal to one twentieth of the unconfined mean free path it is observed that the effective mean free path converges to a flat profile at a value of about the same as the distance between the walls, which fulfils a third requirement [14].

For the spherical obstacle case the effective mean free path obtains half of the unconfined mean free path value at the wall. The effective mean free path profile approaches the unconfined value at a shorter wall distance compared to the corresponding one-planar-wall case, as intuitively expected.

The spherical cavity case also shows results where the effective mean free path inside a relatively large cavity approaches half the unconfined value at the wall and approaches the unconfined value in the bulk of the cavity. The effective mean free path for a relatively small cavity approaches the average distance to the walls from any position of the gas. This is to be expected since the molecular travelling distances between collisions are not as often terminated by inter-gas molecular collisions as they are for gas molecular collisions with walls.

It is reasonable that the probability of the molecular travelling distance without experiencing a collision is based on the exponential probability function. This is reasonable because this function is commonly used in scenarios where there is an assumption of constant probability of an occurrence per unit of the dependant variable. In this thesis it is assumed that the molecules of an unconfined gas are equally probable to travel in any direction, that the speed of the molecules does not depend on their direction of travel and that as long as the molecular density of a gas is spatially uniform and the minimum spacings between the molecules of the gas should be roughly the same. With regard to these assumptions it is reasonable to believe that the molecules also have a constant probability of experiencing a collision per unit of length of travel which is in consistency with the constant probability per unit of a dependant variable, on which the exponential function is based. In this thesis the exponential probability function is applied even in near-wall regions, therefore a reasoning should be made concerning the use of the exponential function in these situations. For a gas in a near-wall region it is still assumed that the molecule is equally probable to travel in any direction and that this direction is independent of the speed that the molecule is travelling in. It is also assumed that molecules are equally probable to experience collisions in any part of their travelling trajectories towards solid boundaries as for molecules travelling in the direction of an unconfined gas. However, in case a molecule approaches a wall it will clearly experience a collision. This is accounted for in the the probability function since the upper limit of the probability function's dependence on the travel distance is set to the wall distance. The applicability of using the exponential probability function for estimating the near-wall effective mean-free-path is therefore considered to be reasonable for cases where the assumptions stated above are valid.

A validation of the theoretical mean free path is performed using the method of molecular dynamics. This method simulates the gas in a detailed manner by describing it as a discrete number of molecules interacting by Lennard-Jones' repulsive short-range and attractive long-range forces. Since the molecules in this description do not experience collisions at instantaneous moments but instead interacts through continuous forces, the defined criterion of a collision has to be implemented. In the molecular dynamics simulations of this thesis a collision between molecules is considered to have occurred if they are closer to each other than their equivalent hard-sphere diameter. This criterion for molecular collisions is consistent with the theoretical description, which is essential for comparisons between these methods. The parameter used for determining the magnitude of the potential between the molecules is also chosen so that consideration is taken to the hard-sphere diameter so that the scattering of molecules occurs in a similar manner as for more commonly used Lennard-Jones parameters. The mean free path is then recorded by averaging the collision free path of every molecule within a certain spatial domain during a certain time frame.

First a simulation is made, using molecular dynamics, of the distribution of the free paths for the gases helium, neon and argon. These results are very similar to the corresponding theoretical probability distribution except that the simulation shows a slightly higher probability of shorter free paths. Then the average of the free paths, the mean free path, is measured. It is found that the molecular dynamics simulation reproduces the theoretical values of the mean free path for argon, neon and helium within an approximate accuracy of 1.4%, 1.8% and 0.7% respectively. Also an investigation is made measuring the mean free path when only binary collisions are considered as opposed to collisions involving more than two molecules. It is found that, even though roughly 80% of the molecular collisions are binary, there is no observable difference in the measured mean free path from the two-collision descriptions.

Then this molecular dynamics method is used to measure the effective mean free path profiles in the vicinity of one planar wall and two planar wall configurations. The walls are either modelled to yield only specular reflections, only diffusive reflections or explicit reflections caused by simulating a wall consisting of tethered molecules. It is found that the theoretical description corresponds reasonably well with the molecular dynamics results for the specular wall reflections for the one planar wall case. The molecular dynamics results for the mean free path profile between two planar specular walls is similar to the corresponding theoretical results up to $Kn \approx 0.5$. For higher Kn the mean free path profiles differ in shape but keep the same order of magnitude. The molecular dynamics simulation using diffusive walls produces a mean free profile which is considerably lower in the near-wall area and has a more rapid increase to the unconfined value compared to the case of specular wall reflections. For the effective mean free path measured in the vicinity of explicit walls it is found that the whole profile is much lower than both the results by specular or diffusive walls. It is also found that the results of the mean free path profile strongly depend on the thickness of the modelled wall, which is probably due to that the thicker wall has a significantly different potential influence on the gas molecular behaviour.

Finally the molecular dynamics simulation is used to measure the mean free path in the near vicinity of the non-planar geometries of a spherical obstacle and a spherical cavity. For the spherical obstacle it is found that the measured effective mean free path profiles caused by both the specularly and the diffusive reflective surfaces are very similar to each other. It is also found that the measured mean free path profiles are similar to the theoretical profile in the near-wall area but is about 2% lower towards the bulk. For the spherical-cavity case three different diameters of the cavity are simulated, which are chosen to be comparable to the length of the unconfined mean free path. It is found that all the measured mean free path profiles are similar to the theoretical profiles in the bulk but are about 5% low in the near-wall areas.

One of the main assumptions concerning the applicability of using an exponential probability function for describing the effective mean free path profile in near wall regions is that molecules should on average be expected to have the same speed independent of their travelling trajectories. This assumption is assumed to be valid for all the implicit walls. This requirement is however not likely to be fulfilled for cases using explicit walls since the molecular velocities will be geometrically affected by the potential of the wall. The speed distribution is therefore measured for molecules that are reflected of an explicit wall in section 4.5.2. The results of the speed distribution showed that the molecules where indeed faster in the near wall area compared to the Maxwellian speed distribution. If this aspect would be the only affect on the near-wall effective mean free path then it would be expected that the near wall value would be higher than the corresponding results by the implicit walls, but it is in fact significantly lower. This lower profile is probably caused by other factors than the molecular speed distribution. A likely reason for the low effective mean free path profile to occur near the explicit walls is due to that molecules are likely to get caught in the well of the Lennard-Jones potential between the long-range attractive force and the short-range repulsive force. The trapping of molecules in the near wall area would thereby cause a locally higher molecular density which in turn would cause a shortening of the mean-free-path in this region. A closer investigation is therefore of interest concerning to what extent this potential force can influence the mean free path.

Both the effective mean free path results from the theoretical model and the effective mean free path from the molecular dynamics measurements are applied for solving the isothermal Navier–Stokes–Fourier equations. For this method the effective mean free path is shown to relate to the viscosity through a linear relationship which in turn yields a geometry-dependent viscosity. It is also argued that the effective mean free path should be involved in the velocity-slip boundary conditions instead of the conventional unconfined mean-free-path value.

By extending the Navier–Stokes equations with the effective mean free path definition, the classical fluid flow problems of the Couette flow and Poiseuille flow are solved with a first- and second-order velocity-slip. In the solution of the extended Navier–Stokes equations three different effective mean free path descriptions are used. The descriptions are from the theoretical effective mean free path derivation and the measured effective mean free path from molecular dynamics for both specular and diffusive wall reflections. The effective mean free path descriptions affect the results of the extended Navier–Stokes equations quite similarly for $Kn < 0.5$. The largest difference between the theoretically derived description and the measured descriptions is for $Kn \geq 1$, which is shown in the mass flow rate results of the Poiseuille flow.

The velocity-profile results of the Couette flow shows that the extended Navier–Stokes equations converge with the results of the conventional Navier–Stokes equations for $Kn = 0.01$, which is a fundamental criterion. For larger Kn it is shown that the new model manages to produce velocity profiles similar to both the DSMC method and the BGK method up to $Kn \approx 1$, where the second-order velocity-slip represents slightly better results.

For the Poiseuille flow it is shown that the extended Navier–Stokes equations manage to converge with the results of the conventional Navier–Stokes equations for $Kn = 0.1$. For larger Kn it is shown that the velocity profiles of the new model are slightly different from the validation data of the BGK method but manage to capture the same magnitude of the cross-sectional velocity using the second-order velocity-slip, which is important in order to reproduce similar mass flow rates. The mass flow rates of the new model are compared to experimental results [15] and the BGK method [56]. The new model applied with second-order velocity-slip manages to capture the mass flow minimum and shows good agreement with the experimental data up to $Kn \approx 3$, which is relatively close to the free molecular regime where a flow needs to be described by individual molecules and not by a continuous medium. It is shown that the new model, applied with first-order velocity-slip, does not produce good agreement with the experimental mass flow rates above $Kn \approx 0.3$.

There are three main interesting areas of future research based on the work of this thesis. The first is to study the effective mean free path for other types of walls. Second it would be interesting to implement the extended Navier–Stokes equations as a solution method in the OpenFOAM [1] toolkit. And the third interesting area to investigate is the influence of near-wall effects on the thermal heat transfer of gases.

The first field of investigation that is directly applicable to this material concerns further investigation of the effects of different types of walls. It is reported by various investigators that the tangential momentum exchange between solid walls and molecules reflected off the walls is neither fully diffusive nor fully spectral. Instead about 80% of the molecules experience diffusive reflections and the rest experience specular reflections. It would therefore be interesting to investigate how well the isothermal extended

Navier–Stokes equations would solve the Couette and Poiseuille flow cases with an effective mean free path description based on partly specular reflection and partly diffusive reflections. It would also be of interest to measure the effective mean free path profile for an explicit wall that is sufficiently thick for the effective mean free path profile not to change shape using marginally more or less molecules in the wall. The results in this thesis show that the effective mean free path profile is about 15% lower in the near wall region for an explicit wall of an approximate thickness of 3.7×10^{-10}m compared to a wall with an approximate thickness of 3.1×10^{-10}m and about 4% lower at a wall distance of two conventional mean free paths. Since the wall molecules that are simulated in this investigation are neon molecules with $\sigma = 2.5836$ the wall consists of a molecular layer which is roughly one and one half molecular diameters thick. However a wall with this thickness is not representative for actual walls and it is reasonable to believe that a change of the wall potential, due to the wall thickness, will vary to a large extent dependant on how many molecules there are in the wall. This change of wall potential will most likely influence the profile of the effective mean free path in the near wall region. It is assumed that a thicker explicit wall would yield a still lower effective mean free path profile. It would be of interest to investigate the cases of the Couette flow and the Poiseuille flow for the extended Navier–Stokes equations applied with an effective mean free path empirically derived for such conditions. It would also be very interesting to investigate the effective mean free path in the vicinity of an explicit wall which uses purely short-range repulsive potentials such as the Weeks–Chandler–Andersen wall potential. This potential cuts off the attractive long-range force from the Lennard-Jones potential of the wall molecules [58].

The second aspect of future work is to develop extended Navier–Stokes equations, which could be implemented in the OpenFOAM toolkit. This would be beneficial in the sense that flow cases for arbitrary geometrical configurations could then be modelled as opposed to the two-planar-wall test cases of the Couette and Poiseuille flows studied here. For this model to be implemented the effective mean free path of every point of the gas domain needs to be determined, however the form of the domain is shaped. One method of doing this could be to use an already existing tool in OpenFOAM which calculates the closest distance to the boundaries from any point of the gas domain. This function would then be modified to find various wall distances for various directions, being distributed with equal angular separation from the point of interest. The usage of wall distances from these trajectories is in consistency with the point of view that molecules are equally probable to travel in any direction which is used in this thesis. The wall distances would then be inserted in the theoretically derived mean free path probability function for a single travelling direction, and then averaged with respect to all the effective mean free paths obtained from all directions. By this method it would not matter in case the bounding domain is planar or spherical or any other shape since the measured wall distance trajectories only considers the mean free paths from their trajectories independently. The main geometrical effect becomes apparent once these values are averaged yielding the mean free paths for equally probable travelling direction. The velocity slip boundary conditions would also have to be implemented dependent on these effective mean free paths.

In case the effective mean free path is implemented in the OpenFOAM toolkit it would need to take a transient relaxation factor into account. This would be consistent with the effect captured by the molecular dynamics simulation where the free path is "remembered" by the molecules and is not instantaneously altered in case the geometry is changed. For instance, if a flow over a wall is considered where the wall is suddenly taken away, then the molecular dynamics simulation would show an effective mean free path which is the same as just before the wall was removed. However, for the model derived in this thesis the effective mean free path would obtain the unconfined mean free path value as soon as the wall was taken away.

It should be noted that it would be more simple in case the average wall-distance could be computed first and then inserted into the one directional effective mean free path expression. The results of such an approach were tested for the effective mean free path of the spherical obstacle and the spherical cavity cases. It was found that the two approaches had very similar results for the spherical obstacle case. For the spherical cavity case it was found that the two approaches where only similar in case the diameter of the cavity was small relative to the unconfined mean free path. If the diameter of the cavity was large relatively to the unconfined mean free path the effective mean free path profile was close to the value of the unconfined λ at the surface. This discrepancy is due to the difference between the two expressions:

$$\langle 1 - \exp(-r_d) \rangle \neq 1 - \exp(\langle -r_d \rangle), \tag{6.1}$$

where r_d is the radial distance from the sphere or cavity centre and the angular brackets are averaged quantities with respect to travelling directions of the molecules. Since these equations gave similar effective mean free path results for the spherical obstacle case and not for the cavity case it is assumed that the two expressions of Eqn. (6.1) are more likely to be similar in most cases where there is no reciprocal wall present.

The third interesting area of future work is to investigate how the presence of a wall influences the heat-transfer characteristics in near-wall areas. In this thesis only isothermal cases are considered where it is assumed that the average momentum transfer between molecules is proportional to the effective mean free path profile. An example of this can be illustrated considering that molecules of the bulk of the gas receive momentum from molecules that have had their previous collision on average one mean free path away, and similarly, for a gas in the near-wall region, momentum is on average received from a distance that is half of one mean free path away. This point of view is based on that molecules exchange full momentum at collisions. However the heat transfer due to molecular collisions is probably not fully exchanged between molecular collisions in the same extent as for the momentum exchange. This is strengthened by that molecules need to experience some three or four molecular collisions in order to equilibrate their energy with other molecules in the same vicinity, as reported by Reese *et al.* [51]. It would therefore be interesting to investigate the influence of surface effects on the heat-transfer characteristics of a gas.

References

[1] OpenFOAM, the Open Source CFD Toolbox, http://www.openfoam.com/.

[2] E. Arkilic, K. Breuer, and M. Schmidt. Mass flow and tangential momentum accomodation in silicon micromachined channels. *Journal of Fluid Mechanics*, 437:29–43, 2001.

[3] E. Arkilic, M. Schmidt, and K. Breuer. Gaseous slip flow in long microchannels. *Journal of Microelectromechanical Systems*, 6(2):167–178, 1997.

[4] E. Arlemark, S. Dadzie, and J. Reese. An extension to the Navier–Stokes equations to incorporate gas molecular collisions with boundaries, To be published in Journal of Heat Transfer.

[5] R. Barber, Y. Sun, X. Gu, and D. Emerson. Isothermal slip flow over curved surfaces. *Vacuum*, 76(1):73–81, 2004.

[6] G. Bird. *Molecular Gas Dynamics and the Direct Simulation of Gas Flows*. Oxford Science Publications, 2003.

[7] R. Bird, W. Stewart, and E. Lightfoot. *Transport Phenomena*. John Wiley & Sons, 2nd edition, 2002.

[8] C. Cercignani. *Rarefied Gas Dynamics: from Basic Concepts to Actual Calculations*. Cambridge University Press, 2000.

[9] C. Cercignani and A. Daneri. Flow of a rarefied gas between two parallel plates. *Journal of Applied Physics*, 34(12):3509–3513, 1963.

[10] S. Colin. Rarefaction and compressibility effects on steady and transient gas flows in microchannels. *Microfluidics and Nanofluidics*, 1(3):268–279, 2005.

[11] S. Colin, P. Lalonde, and R. Caen. Validation of a second-order slip flow model in rectangular microchannels. *Heat Transfer Engineering*, 25(3):23–30, 2004.

[12] R. Deissler. An analysis of second-order slip flow and temperature-jump boundary conditions for rarefied gases. *International Journal of Heat and Mass Transfer*, 7(6):681–694, 1964.

[13] N. Dongari, A. Agrawal, and A. Agrawal. Analytical solution of gaseous slip flow in long microchannels. *International Journal of Heat and Mass Transfer*, 50(17–18):3411–3421, 2007.

[14] N. Dongari, A. Sharma, and F. Durst. Pressure-driven diffusive gas flows in microchannels: from the Knudsen to the continuum regimes. *Microfluidics and Nanofluidics*, 6:679–692, 2009.

[15] T. Ewart, P. Perrier, I. Graur, and J. Meolans. Mass flow rate measurements in a microchannel, from hydrodynamic to near free molecular regimes. *Journal of Fluid Mechanics*, 584:337–356, 2007.

[16] P. Fieseler. A method for solar sailing in a low earth orbit. *Acta Astronautica*, 43(9–10):531–541, 1998.

[17] M. Gad-el-Hak. Fluid mechanics of microdevices – the Freeman Scholar lecture. *Journal of Fluids Engineering, Transactions of the ASME*, 121(1):5–33, 1999.

[18] M. Gad-el-Hak. Gas and liquid transport at the microscale. *Heat Transfer Engineering*, 27:13–29, 2006.

[19] T. Gemci, V. Ponyavin, Y. Chen, H. Chen, and R. Collins. Computational model of airflow in upper 17 generations of human respiratory tract. *Journal of Biomechanics*, 41(9):2047–2054, 2008.

[20] X. Gu and D. Emerson. A computational study of oscillatory Couette flows in the transition regime with higher order moment method. In *Proceedings of 1st European Conference on Microfluidics μFlu08, Bologna, Italy, 10-12 Dec 2008.*

[21] E. Guarini, U. Bafile, F. Barocchi, F. Demmel, F. Formisano, M. Sampoli, and G. Venturi. Collective excitations in liquid cd4: Neutron scattering and molecular-dynamics simulations. *Europhysics Letters*, 72(6):969–975, 2005.

[22] Z. Guo, B. Shi, and C. Zheng. An extended Navier–Stokes formulation for gas flows in the Knudsen layer near a wall. *Europhysics Letters*, 80(2):24001–24006, 2007.

[23] N. Hadjiconstantinou. Comment on Cercignani's second-order slip coefficient. *Physics of Fluids*, 15:2352–2354, 2003.

[24] N. Hadjiconstantinou. Oscillatory shear-driven gas flows in the transition and free-molecular-flow regimes. *Physics of Fluids*, 17(10):100611, 2005.

[25] Y. Hsia and G. Domoto. An experimental investigation of molecular rarefaction effects in gas lubricated bearings at ultralow clearances. *Journal of Lubrication Technology-Transactions of the ASME*, 105(1):120–130, 1983.

[26] J. Jackson and D. Robert. Nonlinear auditory mechanism enhances female sounds for male mosquitoes. *Proceedings of the National Academy of Sciences of the United States of America*, 103:16734–16739, 2006.

[27] J. Jang and S. Wereley. Pressure distributions of gaseous slip flow in straight and uniform rectangular microchannels. *Microfluidics and Nanofluidics*, 1:41–51(11), 2004.

[28] S. Kandlikar, S. Garimella, D. Li, S. Colin, and M. King. *Heat Transfer and Fluid Flow in Minichannels and Microchannels*. Elsevier, 2005.

[29] G. Karniadakis, A. Beskok, and N. Aluru. *Microflows and Nanoflows: Fundamentals and Simulation*. Springer, 2005.

[30] E. Kennard. *Kinetic Theory of Gases*. McGraw-Hill Book Co. Inc., 1938.

[31] D. Lockerby and J. Reese. High-resolution Burnett simulations of micro Couette flow and heat transfer. *Journal of Computational Physics*, 188(2):333–347, 2003.

[32] D. Lockerby and J. Reese. On the modelling of isothermal gas flows at the microscale. *Journal of Fluid Mechanics*, 604:235–261, 2008.

[33] D. Lockerby, J. Reese, D. Emerson, and R. Barber. Velocity boundary condition at solid walls in rarefied gas calculations. *Physical Review E*, 70(1/2):017303, 2004.

[34] D. Lockerby, J. Reese, and M. Gallis. A wall-function approach to incorporating Knudsen-layer effects in gas micro flow simulations. *Procedings of the 24th International Symposium on Rarefied Gas Dynamics*, 762(1):731–736, 2005.

[35] G. Macpherson, M. Borg, and J. Reese. Generation of initial molecular dynamics configurations in arbitrary geometries and in parallel. *Molecular Simulation*, 33(15):1199–1212, 2007.

[36] G. Macpherson, N. Nordin, and H. Weller. Particle tracking in unstructured, arbitrary polyhedral meshes for use in cfd and molecular dynamics. *Communications in Numerical Methods in Engineering*, 25(3):263–273, 2009.

[37] G. Macpherson and J. Reese. Molecular dynamics in arbitrary geometries: parallel evaluation of pair forces. *Molecular Simulation*, 34(1):97–115, 2008.

[38] S. Mahulikar, H. Herwig, and O. Hausner. Study of gas microconvection for synthesis of rarefaction and nonrarefaction effects. *Journal of Microelectro Mechanical Systems,*, 16(6):1543–1556, 2007.

[39] G. Maitland, M. Rigby, E. Smith, and W. Wakeham. *Intermolecular Forces*. Clarendon Press, 1981.

[40] A. Markvoort, P. Hilbers, and S. Nedea. Molecular dynamics study of the influence of wall–gas interactions on heat flow in nanochannels. *Physical Review Letters*, 71(6):066702, 2005.

[41] J. Maurer, P. Tabeling, P. Joseph, and H. Willaime. Second-order slip laws in microchannels for helium and nitrogen. *Physics of Fluids*, 15(9):2613–2621, 2003.

[42] J. Maxwell. On stresses in rarefied gases arising from inequalities of temperature. *Philosophical Transactions of the Royal Society of London*, 170:231–256, 1879.

[43] Y. Mitsuya. Modified Reynolds equation for ultrathin film gas lubrication using 1.5-order slip-flow model and considering surface accommodation coefficient. *Transactions of the Japan Society of Mechanical Engineers C*, 58(555):3341–3346, 1992.

[44] R. Myong, D. Lockerby, and J. Reese. The effect of gaseous slip on microscale heat transfer: an extended Graetz problem. *International Journal of Heat and Mass Transfer*, 49(15-16):2502 – 2513, 2006.

[45] R. Myong, J. Reese, R. Barber, and D. Emerson. Velocity slip in microscale cylindrical Couette flow: the Langmuir model. *Physics of Fluids*, 17(8):087105, 2005.

[46] S. Nedea, A. Frijns, A. van Steenhoven, A. Markvoort, and P. Hilbers. Hybrid method coupling molecular dynamics and Monte Carlo simulations to study the properties of gases in microchannels and nanochannels. *Physical Review Letters*, 72(1):016705, 2005.

[47] C. Nordling and J. Österman. *Physics Handbook for Science and Engineering.* Studentlitteratur, 6th edition, 1999.

[48] L. Pan, G. Liu, and K. Lam. Determination of slip coefficient for rarefied gas flows using direct simulation Monte Carlo. *Journal of Micromechanics and Microengineering*, 9(1):89–96, 1999.

[49] G. Patterson. *Molecular Flow of Gases.* John Wiley & Sons, 1956.

[50] J. Pitakarnnop, S. Varoutis, D. Valougeorgis, S. Geoffroy, N. Laurien, and S Colin. New experimental setup for accurate measurement of gas microflows. In *Proceedings of 1st European Conference on Microfluidics μFlu08, Bologna, Italy, 10-12 Dec 2008.*

[51] J. Reese, M. Gallis, and D. Lockerby. New directions in fluid dynamics: non-equilibrium aerodynamic and microsystem flows. *Royal Society of London Philosophical Transactions Series A*, 361:2967–2988, 2003.

[52] S. Schaff and P. Chambre. *Flow of Rarefied Gases.* Princeton University Press, 1961.

[53] R. Schamberg. *The fundamental differential equations and the boundary conditions for high speed slip-flow, and their application to several specific problems.* PhD thesis, California Institute of Technology, 1947.

[54] T. Schwartzentruber, L. Scalabrin, and I. Boyd. A modular particle-continuum numerical method for hypersonic non-equilibrium gas flows. *Journal of Computational Physics*, 225(1):1159–1174, 2007.

[55] F. Sharipov. Modeling and calculations of gas flows in microfluidics: DSMC vs kinetic equation. In *Proceedings of 1st European Conference on Microfluidics μFlu08, Bologna, Italy, 10-12 Dec 2008.*

[56] F. Sharipov. Rarefied gas flow through a long rectangular channel. *Journal of Vacuum Science & Technology A:Vacuum Surfaces and Films*, 17(5):3062–3066, 1999.

[57] S. Shen, G. Chen, R. Crone, and M. Anaya-Dufresne. A kinetic-theory based first order slip boundary condition for gas flow. *Physics of Fluids*, 19(8):086101, 2007.

[58] P. Spijker, H. ten Eikelder, A. Markvoort, S. Nedea, and P. Hilbers. Implicit particle wall boundary condition in molecular dynamics. *Proceedings of the Institution of Mechanical Engineers, Part C: Journal of Mechanical Engineering Science*, 222(5):855–864, 2008.

[59] W. Steckelmacher. Knudsen flow 75 years on: the current state of the art for flow of rarefied gases in tubes and systems. *Reports on Progress in Physics*, 49(10):1083–1107, 1986.

[60] D. Stops. The mean free path of gas molecules in the transition regime. *Journal of Physics D*, 3(5):685–696, 1970.

[61] J. Sun and Z. Li. Molecular dynamics simulations of energy accommodation coefficients for gas flows in nano-channels. *Molecular Simulation*, 35(3):228–233, 2009.

[62] L. Trilling. The Knudsen boundary layer in low density gas flow past a crystal. *SIAM Journal on Applied Mathematics*, 28(4):757–777, 1975.

[63] S. Turner, L. Lam, M. Faghri, and O. Gregory. Experimental investigation of gas flow in microchannels. *Journal of Heat Transfer*, 126(5):753–763, 2004.

[64] A. van Well and L. de Graaf. Density fluctuations in liquid neon studied by neutron scattering. *Physical Review A*, 32(4):2396–2412, 1985.

[65] W. Vincenti and C. Kruger. *Introduction to Physical Gas Dynamics.* Krieger, 2002.

[66] M. Von Smoluchowski. Über wärmeleitung in verdünnten gasen. *Annalen der Physik und Chemie*, 64:101–130, 1879.

[67] H. Wijesinghe, R. Hornung, A. Garcia, and N. Hadjiconstantinou. Three-dimensional hybrid continuum-atomistic simulations for multiscale hydrodynamics. *Journal of Fluids Engineering*, 126(5):768–777, 2004.

[68] H. Xue and Q Fan. A high order modification on the analytic solution of 2-d microchannel gaseous flows. In *Proceedings ASME Fluids Engineering Division summer meeting, Boston, Massachusetts, 2000.*

[69] H. Xue, H. M. Ji, and C. Shu. Analysis of micro-couette flow using the burnett equations. *International Journal of Heat and Mass Transfer*, 44(21):4139 – 4146, 2001.

[70] S. Yuhong and W. Chan. Analytical modeling of rarefied Poiseuille flow in microchannels. *Journal of Vacuum Science & Technology A: Vacuum Surfaces and Films*, 22(2):383–394, 2004.

[71] Y. Zheng, J. Reese, and H. Struchtrup. Comparing macroscopic continuum models for rarefied gas dynamics: a new test method. *Journal of Computational Physics*, 218(2):748–769, 2006.